Active corrosion protection of aluminium AA2024-T3 by corrosion inhibitor loaded electrospun nanofibres

An exploratory study and proof of concept

Christian D. Dieleman

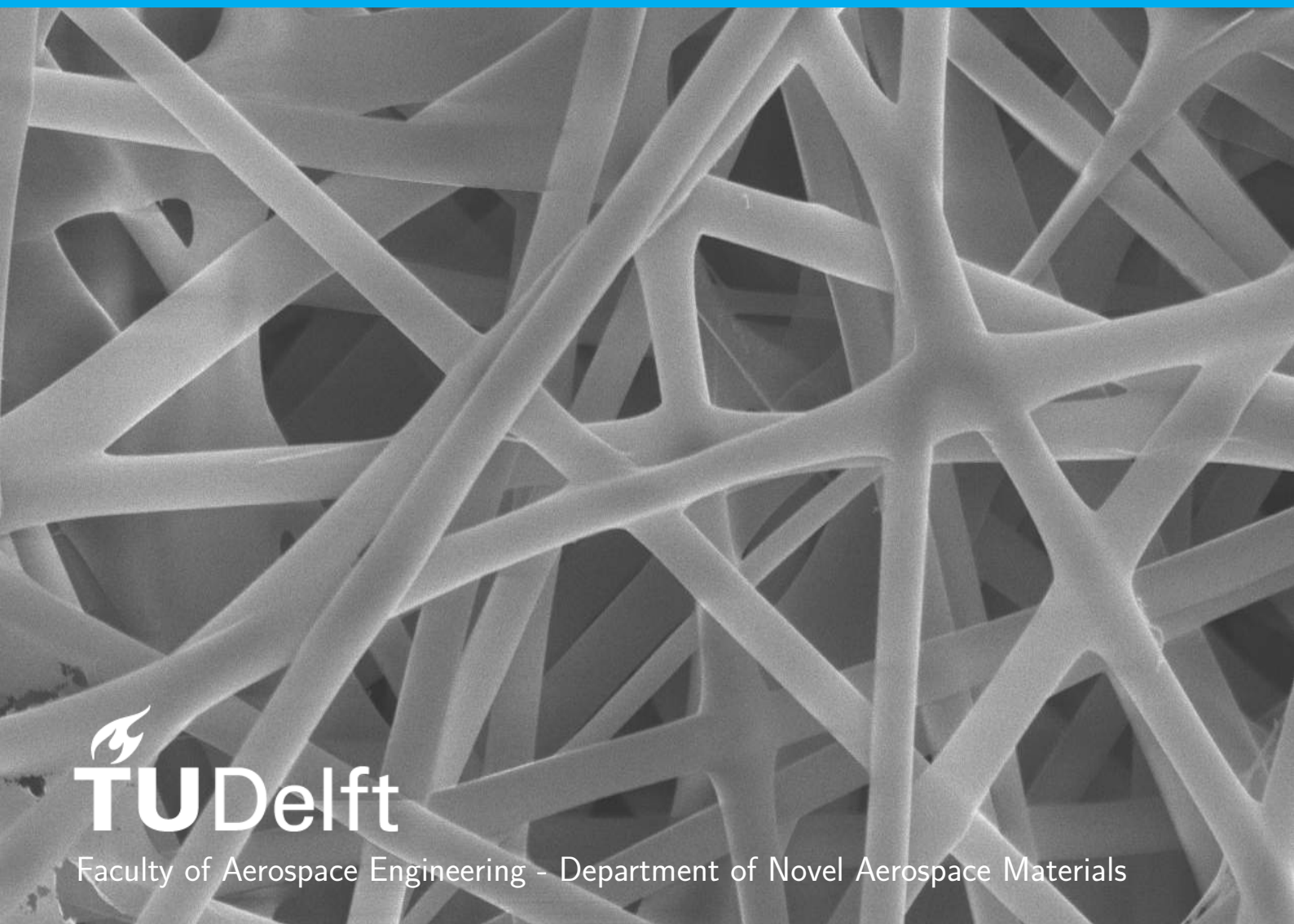

TU Delft
Faculty of Aerospace Engineering - Department of Novel Aerospace Materials

THIS PAGE IS INTENTIONALLY LEFT BLANK.

Active corrosion protection of aluminium AA2024-T3 with corrosion inhibitor loaded electrospun nanofibres

An exploratory study and proof of concept

by

Christian David Dieleman

to obtain the degree of Master of Science
at the Delft University of Technology,
to be defended on Thursday December 22, 2016 at 13:00 AM.

Student number:	1506897	
Project duration:	February 1, 2016 – December 22, 2016	
Faculty:	Aerospace Engineering	
Department:	Aerospace Structures and Materials	
Group:	Novel Aerospace Materials (NovAM)	
Thesis committee:	Prof. dr. ir. S. van der Zwaag,	TU Delft, NovAM, chairman
	Dr. S. J. Garcia,	TU Delft, NovAM, supervisor
	Dr. I. Fernandez-Villegas,	TU Delft, SIC, external member

TU Delft

Contents

Preface

This document is the final piece that will complete my master's program in Aerospace Engineering. My total study has been a journey of little over 8 years, which has not always been easy. I was lucky enough to spend my time in Delft with wonderful people and current times allowed me to take full advantage of many wonderful opportunities.

During my time as a student I have been able to develop myself as a person, gaining new insights in life, personal relationships and have developed the necessary knowledge and skills that allowed me to finish this work. Most of all, during the last two years at the Novel Aerospace Materials department I got excited about not just engineering, but doing science, making me want to extend my studies by pursuing a PhD.

I might not have noticed it right away, but in hindsight every move and 'mistake' I made, gave me an opportunity later on. I held a board function of a small student society for one year which meant a year full of stressed situations and exceptional highlights. Further study delay in my bachelor allowed me to take up a part time job and gain experience at an engineering company, and next to that made me save enough money to fund my own internship to Melbourne.

I want to use this small preface to express my thanks and gratitude for everyone that somehow helped me during this thesis project. First of all my supervisor Dr. Santiago Garcia who has guided me through this project and allowed me to seize opportunities like attending a conference and doing an internship in Australia. Secondly, prof. Sybrand van der Zwaag whose inspiring leadership makes NovAM an exceptionally interesting environment to study. Thirdly, Paul Denissen who was not my daily supervisor but helped out a lot. Also special thanks to Johan Bijleveld and Ranjita Bose for helping in the lab with several machines and equipment. Frans Oostrum and Lijing Xue for their supervision in the lab and Johan Boender for helping building my set-up and Tomasso Brugo for helping me improve it. I want to thank all the people in the NovAM department for making my time here as pleasant as it was. Special thanks to Kevin de Boom the rides to IKEA and the purchase of the Nespresso machine which was of great help during my thesis, Michael den Brabander for the good conversations and useful discussions, Wouter Vogel for the bad puns and horrible memes, Wouter Post for the great music influence and everyone else I forget to mention here. I want to thank all my wonderful friends and band mates with whom I had great times, whether it was on stage, on a sailing boat or in café de Klok. Of course I want to thank my lovely girlfriend Kimberly McGuire who was always there when I had difficulties and who's spirit inspired me to work hard, never give up and made me realise to always use your full potential. Finally, I want to thank my loving parents who have always supported me during my studies and with my choices, even though some of them meant an extension of my time as a student. I am grateful to have all of you help me deliver this work.

Christian Dieleman,
Delft, December 2016

"We cannot teach people anything; we can only help them discover it within themselves."
Galileo Galilei

Executive summary

Aluminium AA2024-T3 is a high strength aluminium alloy widely used in aerospace. The strengthening copper-rich intermetallic phases, however, make the material very susceptible to aqueous corrosion and severe pitting. To protect the metal, coatings loaded with corrosion inhibitors are typically used. Traditionally, highly efficient CrVI-based inhibitors have been used but these are soon to be banned due to their high genotoxicity. The use of alternative environmentally friendly inhibitors is commonly bound to the problem of incompatibility with the organic coating matrix. As a solution to reduce unwanted inhibitor-matrix reactions and to control the inhibitor release extensive research has been devoted to the development of responsive inhibitor nanocarriers. These carriers are, however, limited in the amount of inhibitor they can store thereby having a narrow potential for long-term protection at damage sites such as scratches or cracks. Alternative concepts are therefore needed. This work explores for the first time the use of responsive electrospun polymeric nanofibers loaded with corrosion inhibitors as an efficient carrier system for long term protection of relatively big damages in coated AA2024 structures.

For the proof of concept explored in this work, water soluble poly(vinyl alcohol) fibres loaded with up to 10 wt% CeCl3 were successfully electrospun. To control the inhibitor release the PVA fibres were crosslinked at different degrees by glutaraldehyde. The influence of fibre chemistry and inhibitor loading on the release kinetics of the loaded fibre mats was investigated via in-situ UV/VIS spectroscopy. Loaded fibre mats were successfully incorporated in a protective epoxy/amine coating system varying the position of the inhibiting mat within the coating with respect to the substrate. In-situ opto-electrochemical impedance spectroscopy was used to investigate the long-term, protective, self-healing behaviour of the prepared coating systems after damage. Protection up to 4 weeks was achieved for several coating compositions with different fibre chemistries and corrosion inhibitors. This research opens the path for the development of sophisticated, tailored and highly efficient inhibitor delivery systems for the protection of metal structures at large damages for long immersion times.

List of acronyms

Acronym	Definition
ACE	Acetone
AU	Absorbance unit
$Ce(dbp)_3$	Cerium dibutylphosphate
$CeCl_3$	Cerium chloride
DC	Direct current
DMF	Dimethyl formamide
DI	Deionised
EIS	Electrochemical impedance spectroscopy
ES	Electrospinning
EtOH	Ethanol
FESEM	Field emission scanning electron microscopy
FPI	Fluorinated polyimide
FTIR	Fourier transform infrared spectroscopy
GA	Glutaraldehyde
GPTMS	3-glycidoxypropyltrimethoxysilane
HCl	Hydrochloric acid
ICP-MS	Inductively coupled plasma mass spectrometry
ICP-OES	Inductively coupled plasma optical emission spectrometry
Li_2CO_3	Lithium carbonate
NaOH	Sodium hydroxide
OH	Hydroxide
OCP	Open circuit potential
PAA	Polyacrylic acid
PAN	Polyacrylonitrile
PDT	Poly(dodecylthiophene)
PEO	Polyethylene oxide
P(FDA-*co*-AA)-*b*-PAN	Poly(heptadecafluorodecylacrylate-*co*-acrylic acid)-*b*-poly(acrylonitrile)
PLLA	Poly(*L*-lactide)
PMMA	Polymethyl methacrylate
PU	Polyurethane
PVA	Polyvinylalcohol
PVC	Polyvinylchloride
PVDF	Poly(vinylidene fluoride)
PVP	Polyvinylpyrrolidone
RE	Rare earth
SEM	Scanning electron microscopy
TEM	Transmissive electron microscopy

Continued on next page

– Continued from previous page –

Acronym	Definition
TPOZ	Tetra n-propoxyzirconium
TUFT	Tubes by fibre templates
dbp	Dibutylphosphate

List of symbols

Symbol	Definition	Units
A	Absorbance	[AU]
C	Concentration	[mM]
c	Concentration	[M]
D	Diffusion constant	[m^2 s^{-1}]
I	Transmitted light intensity	[-]
I_0	Incident light intensity	[-]
J	Diffusion flux	[mol m^{-2} s^{-1}]
k	Material related constant	[-]
l	Path length	[m]
M	Mass of inhibitor	[mg]
T	Transmittance	[-]
t	Time	[s]
w_i	Mass fraction	[-]
x	Position	[m]
ϵ	Molar absorptivity	[m^2 mol^{-1}]
λ	Wavelength	[nm]
φ	Concentration	[mol m^{-3}]
ω	Rotational speed	[m/s],[rpm]

Subscripts	
Ce	Cerium
$CeCl_3$	Cerium chloride
$Ce(dbp)_3$	Cerium dibutyl(phosphate)
PVA	PVA
t	Certain time
x	Certain number
∞	Infinite time

List of Figures

List of Tables

Chapter 1

Introduction

This chapter introduces the context of the project, its scope and outline. It is meant for the reader to understand why this project was executed, what problems it is looking to solve and what insights it tries to provide.

1.1 Problem statement

Corrosion of metals remains a big problem in the engineering world. In the United States alone, costs that can be related to corrosion yearly add up to $2.2 trillion [3], which in its turn is around 3% of the world gross domestic product (GDP) [4]. This is only the cost of direct losses in terms of loss of equipment, maintenance, replacement etc. Environmental issues, downtime and harm and injuries caused by corrosion are not even included in these figures [3] as they are hard to estimate. Scientists have therefore been looking for methods to protect metallic structures against corrosion for centuries.

Metal corrosion is defined by Popov as *"the spontaneous destruction of metals and alloys caused by chemical, biochemical, and electrochemical interaction between metals and alloys and the environment."* [5] This destruction is caused by the fact that pure metals or alloys with intermetallic phases are converted to more thermodynamically stable metal oxides and hydroxides, which have lower mechanical properties than the pure metal. Protective coatings, that shield the underlying structure from the harsh environment causing corrosion, have been one of the major ways to protect metals against corrosion [6]. These coatings initially provide a passive barrier that separates the substrate from the environment. As the coating deteriorates over time, however, it may lose its protective properties. By adding inhibitors, that can be released upon damage and subsequently react with the environment, new barriers can be formed after the substrate is exposed [7–9]. Hexavalent and trivalent chromates (Cr^{6+}, Cr^{3+}) have been among the most used inhibitors for corrosion protection over hundred years as they are very efficient in forming protective oxide layers at damage sites [9]. The carcinogenic nature of chromates, however, has caused them to be banned by the European Union, between 2015 and 2019 [10]. They, therefore, have to be replaced by environmentally friendly alternatives and should be released in an efficient way. Rare Earth (RE) or lanthanide compounds seem to be good candidates to replace chromate based inhibitors [11]. Especially cerium based inhibitors have been extensively investigated since the late seventies and early eighties as corrosion inhibitors for aluminium [12]. Many studies on corrosion protection of AA2024-T3, a widely used but corrosion susceptible aluminium alloy, are still centered around cerium salts as corrosion inhibitor [7, 13–17].

Advances in the field of self-healing materials can help in the design of high performance anti-corrosion coatings that can provide stable storage of the inhibitor over long time spans and can be triggered to release the inhibitor at the right time [6]. The field of self-healing materials and protective coatings has been growing extensively in the last decade [18, 19]. Self-healing materials or coatings have the ability to restore (a part of) their original functionality after a damage occurs. This

restoration can either be executed by an intrinsic mechanism in the material or coating chemistry, or with use of an embedded system of carriers containing the healing agents or inhibitors [18]. These carriers protect the active agent or inhibitor from unwanted leaching, unwanted reactions with the environment and unwanted reaction with the matrix material and have been one of the major topics of research since the field emerged. Many materials, shapes and sizes have been investigated, ranging from microcapsules [20] to nanosized, porous zeolites [21]. These particles, however, can carry only a limited supply of corrosion inhibitor and the release of inhibitor depends greatly on particle size and distribution [22].

For self-healing composite materials, fibres have also been used as carrier of self-healing agent. The advantage of fibres over particles is, that due their shape and distribution, fibres are more likely to be exposed when the coating is damaged, making it easier to release its content and provide a continuous supply of this agent [18], much like the vascular system in the human body. This makes fibres excellent candidates for carrying inhibitors as well, but is something that has never been investigated before. This thesis will explore the possibility of using fibres as carriers of corrosion inhibitors inside a self-healing anti-corrosion coating system and investigate the main parameters that have an influence on the performance of the coating.

Electrospinning is a field that started growing rapidly in the late 1990s and early 2000s [23]. Electrospinning is a relatively simple process to produce polymeric nano- and micro sized fibres in a membrane or non-woven mat. The process gives a lot of control over the morphology of the fibres and many different applications have made use of electrospun fibres [24], including for drug delivery [25] and as carrier of self-healing agents in composites [26]. It seems therefore an interesting option to consider electrospun fibres as carrier of functional materials with anti-corrosion properties in a coating system, especially if the structure and morphology of the fibres can be used to control the release.

1.2 Research goals

The goal of this thesis project is to investigate the possibility of using electrospun nanofibres loaded with corrosion inhibitors to actively protect aluminium AA2024-T3. This is a new approach that might provide new insights in how to effectively protect metal substrates against corrosion. In order to achieve this goal the following research question needs to be answered:

Can the use of inhibitor loaded nanofibres lead to highly efficient anti-corrosion coating systems?

In order to answer this question a number of subgoals needs to be met.

- Investigate previous research with electrospinning.
- Create inhibitor loaded nanofibers by electrospinning.
- Investigate the release behaviour and how this can be altered.
- Use this knowledge to create a coating system to obtain long term corrosion protection.

As no electrospinning has been carried out in the Aerospace Structures and Materials department of the Aerospace Engineering faculty a set-up needed to be developed and built first. This study is therefore challenging and of exploratory nature.

1.3 Thesis set-up

This thesis describes the research done in order to answer the main research question. The intermediate goals are answered in separate chapters.

Chapter 2 gives an introduction to the process of electrospinning, what is necessary to build a set-up and its relation to corrosion protection.

Chapter 3 elaborates on the development of the electrospinning set-up and how fibres can be made with this set-up. The main parameters and their influence on the process will be discussed. It is shown that electrospun fibres can be loaded with corrosion inhibitors.

Chapter 4 describes a method that was developed in order to follow the release kinetics of the loaded fibres by UV/VIS spectroscopy. This chapter also examines these kinetics for simple fibre mats and investigates the influence of several fibre mat characteristics on the release.

Chapter 5 shows the incorporation of the produced and characterised fibre mats in a coating system and shows the influence of several changes in coating parameters on the final protective properties. The challenges in production of these coatings is discussed as well as the electrochemical tests.

The final chapter will summarise the research and draw the most important conclusions of the work.

Chapter 2

Electrospinning of nanofibres - literature

This project revolves around the production of fibres and using them as a carrier for corrosion inhibitors. Large part of the research, therefore, is focussed on the production of these fibres. This chapter introduces the technique of electrospinning in the first three sections and elaborates on the experimental set-up used and the investigated parameters for producing the desired fibres in the subsequent part of the chapter.

2.1 The electrospinning process

Electrospinning was invented at the beginning of the twentieth century and in 1934 a process using an electric field in order to create fibres was patented [24]. In the 1970s Baumgarten was one of the first to describe the influence of different parameters on the end result [27]. In the 1990s it sparked the interest of scientists when the value of this particular way of making nanofibres became clear [28]. The process is recognised as a relatively simple, cheap and versatile process by many [28–32]. Major applications of electrospun nanofibres include filtration [31], battery separators [33,34], anode materials for batteries [35], artery design [36], wound dressing and tissue engineering [23,37], sensors [38], composite materials [39], self-healing composites [26] and drug delivery [25].

One of the main advantages of electrospinning is that it is in essence very simple. For the process only a few elements are needed: a spinneret, usually a syringe with a blunt needle, filled with a polymer solution, a high voltage power source and a grounded collector. Figure 2.1a shows a schematic representation of a typical electrospinning set-up.

The syringe is usually driven by a syringe pump to ensure a constant flow of polymer solution. Some set-ups also use a vertical spinneret where gravity takes care of the flow [24]. When a droplet has formed at the tip of the needle and the power supply is switched on, an electrical field is created and charges start to build up on the droplet surface. The surface tension of the solution, however, keeps the droplet together. If the voltage is sufficiently high and the charges build up further, a so called Taylor cone is formed. A liquid polymer jet is expelled out of the cone when the repulsion between the charges are higher than the surface tension [40]. The liquid polymer jet will start "flying" towards the collector electrode. This process is depicted in figure 2.1b. During this phase the solvent evaporates and similar charges in the polymer fibre start to repel each other, causing the jet to start spinning in a whipping motion [41]. With every rotation the fibre will stretch and the diameter will reduce. At a certain point the solvent will be evaporated and the polymer fibre will solidify and deposit on the collector electrode. The final result is a web of polymer nanofibres [24].

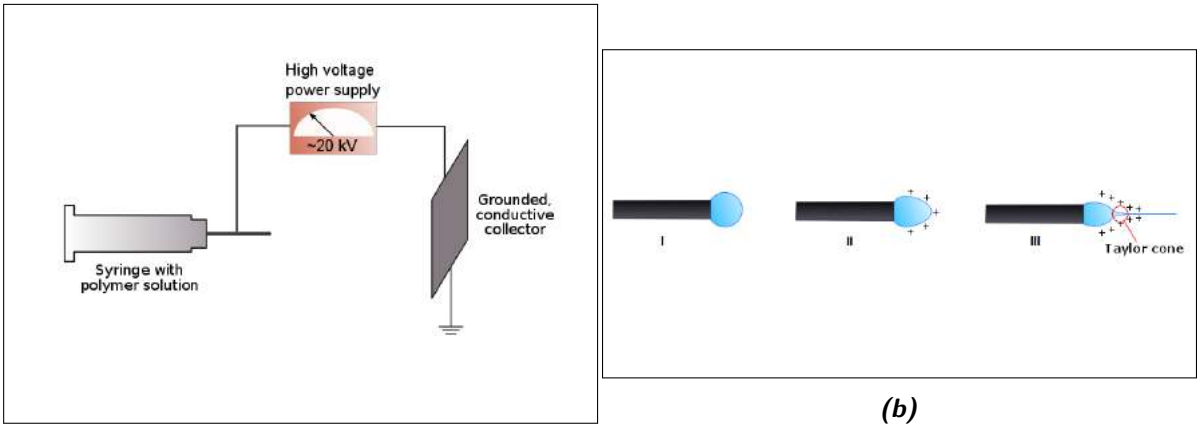

(a) *(b)*

Figure 2.1: *Schematic depictions of electrospinning set-up and process. 2.1a: The basic elements needed for an electrospinning set-up are: high voltage power source, a spinneret (usually a syringe with a blunt needle) and a grounded collector. 2.1b: (I) First a droplet is formed on the tip of the spinneret. (II) When the electrical field is switched on, charges start to build up on the surface of the droplet which causes the droplet to elongate. Surface tension is keeping the droplet together. (III) When the charges are high enough a Taylor cone is formed on the droplets surface and a polymer jet is ejected outwards.*

2.2 Electrospinning parameters

Although the principle behind electrospinning is really simple, there are a lot of factors that can influence the final result. Ramakrishna et al. identify at least three major categories of parameters that affect the quality or form factor of the fibres: the polymer solution, the processing conditions and ambient conditions [24]. Sill and von Recum stated that the processing conditions to have the biggest impact, followed by the polymer solution parameters [23]. As electrospun fibres are formed due to balance between forces and phenomena, changing more than one parameter can create the same sort of fibres as long as the changed parameters remain balanced. A summary of the generalised relationship between parameter changes and end results is given in table 2.1.

Table 2.1: *Main parameters influencing fibre morphology. Adapted from Sill et al. [23].*

Parameter	Fibre diameter	Bead formation
Voltage ↑	First ↓, then ↑ within optimal range	Start to appear when Taylor cone becomes unstable
Feed rate ↑	↑, limited by stretching due to higher charges“	Appear with fused and ribbon like fibres at too high rates
Distance between spinneret & collector ↑	↓, but has a competing mechanism	Appear at too short distances
Polymer solution viscosity ↑	↑, as long as solution is spinnable	↓
Solution conductivity ↑	↓, deposited in larger area	↓
Solvent surface tension ↑	No big influence	Beads more likely to form, rougher fibre surfaces
Solvent volatility ↑	No big influence	Rougher, “porous" fibre surfaces

2.2.1 Processing conditions

Processing conditions are all external conditions that are not related to the environment. These parameters are easy to change in order to alter the morphology of the fibres.

2.2.1.1 Voltage

One of the most obvious and influential parameters is applied potential, as the electrical field produced induces the build up of charges necessary for the electrospinning process to initiate. A voltage of around 6 kV can be enough to form the Taylor cone [40], although the stability of this cone is closely linked to the feed rate.

A higher voltage will affect the fibres in two ways, due to two effects with opposite consequences. Initially, a higher voltage will cause a higher charge in the solution and will, therefore, increase the amount of repulsion within the solution, leading to increased whipping motions and stretching of the material. This causes thinner fibres with a higher order of crystallinity.

The increased repulsion within the polymer will, on the other hand, cause more material to be forced out of the needle at a higher acceleration, decreasing the flight time of the fibre. This will result in fibres with a larger diameter and lower degree of crystallinity [42]. Every polymer solution will have a certain optimum range of voltages wherein it is possible to form smooth fibres of uniform diameter [23].

2.2.1.2 Feed rate

The feed rate of the solution is linked to the voltage. As material is pulled away from the droplet, a certain feed rate is needed to maintain a stable Taylor cone on the outside of the droplet for a given voltage, as there must be equilibrium between material provided and material being drawn towards the collector. If the droplet shrinks, the Taylor cone is not stable which is favourable for bead formation [43, 44]. The lowest feed rate at which a Taylor cone can be maintained will result in the smallest fibre diameter. An increased feed rate will supply more material and is, therefore, likely to produce thicker fibres [44, 45]. This increase of material will, however, also require higher charges to be drawn from the needle. As these higher charges will induce more stretching, the fibre diameter will decrease again. These competing mechanisms will limit the maximum fibre thickness [24].

A higher feed rate also provides more solvent. This solvent needs to evaporate in time in order for the polymer fibre to fully solidify. If too much solvent is present, the polymer may still flow once deposited on the collector. This causes fibres to fuse together and lose their cilindrical shape and get more ribbon like structures [46].

2.2.1.3 Distance between spinneret and collector

The distance between the needle tip and collector is in essence another way of changing the electrical field strength and has a direct influence on the flight time of the fibre. A larger distance will obviously lead to a longer flight time, as well as a weaker electrical field strength, giving a lower acceleration to the jet, increasing flight time even further. Both these effects benefit solvent evaporation. Too short distances may prevent the solvent from evaporating which aids the formation of beads and flat and fused fibres. [45].

As increasing the distance lowers electrical field strength, a similar competition can be found between mechanisms thinning or thickening fibres. It is, however, recognised that the longer flight time has a dominant effect over the fibre stretching compared to the decreasing electrostatic forces, meaning that in general the fibre diameter will decrease with increasing distance [42, 47]. At too long distances, however, the fibres might not deposit at all since the electrical field strength will be too weak to pull the fibres to the collector or initiate electrospinning in the first place.

2.2.2 Polymer solution and ambient parameters

A polymer solution can consist of many different combinations of polymer and solvent. The major influences of the solution parameters are discussed here as well as the ambient conditions, although they play a smaller role.

2.2.2.1 Polymer molecular weight and solution viscosity

The type of polymer, but especially the molecular weight, has an influence on the solution viscosity. The viscosity determines largely if the polymer can be spun or not. If the viscosity is too low, the surface tension will force the solution into droplets as there are not enough polymer chains entangled to ensure a continuous fibre. The causes the solution to be electrosprayed [28]. If the viscosity is too high, on the other hand, the solution is not able to flow and the droplet on the needle tip might already solidify before the polymer jet is ejected, resulting in a clogged needle [44].

The viscosity of the solution does not only depend on the molecular weight of the used polymer, but can also be adjusted by increasing the polymer concentration. Usually solutions with a concentration in the range of 5 wt% to 15 wt% are used, but values up to 40 wt% have been successfully applied to make uniform fibres [32, 48–50]. Higher polymer concentrations will result in thicker fibres [45, 51].

2.2.2.2 Surface tension of the solvent

The solutions surface tension will make the solvent reduce its outer surface area. The build up of charge in the solution should, therefore, overcome the surface tension in order for the process to initiate. The presence of more polymer molecules can decrease the surface tension effect [24]. In highly diluted systems the solution is more likely to "ball up" as the low concentration of polymer molecules cannot lower the surface tension, creating more beads. Solvents with a lower surface tension or with added surfactant will result in smoother fibres [1]. The surface tension has, therefore, a strong interaction with the effect of viscosity.

2.2.2.3 Conductivity

The build up of charges in the solution causes the initiation of electrospinning as well as the whipping motion that thins the fibres. The higher the conductivity, the higher the charges, the more the fibre gets stretched and the smoother and thinner it gets [27, 44]. By adding ions to the solution, it is possible to increase the charges within the solution. A secondary effect of increased conductivity is that there is a greater bending instability, causing the fibres to be deposited in a larger area [52]. As this leads to the fibre travelling for a longer time through the air, this also favours thinning and stretching of the fibres.

2.2.2.4 Volatility of the solvent

The last solution parameter to have an important influence on the end result is the volatility of the solvent. The solvent must evaporate before the fibre reaches the collector in order to retain its cylindrical shape. If the fibres are still wet and the polymer has not solidified when collected, the fibres might start flowing and fusing together into ribbon-like fibres and structures [46]. Next to this, Megelski et al. noticed an influence on solvent volatility on porous structures on the surface of the fibres [45]. More volatile solvents are more likely to show these porous structures.

2.2.2.5 Ambient parameters

Higher humidity or lower tempetures will decrease the evaporation rate of the solvent, while a low humidity and high temperature has the opposite effect. This mechanism can, therefore, again be

tuned to reach the desired fibre surface morphology as described in the previous subsection.

The composition of the atmosphere at which electrospinning takes place also has an influence on the process, as the electrostatic field may affect the gasses in the atmosphere. Some gasses break down under high voltage. There has not been a lot of research in this field, but experiments conducted in a Freon-12 resulted in fibres with a diameter twice as big as fibres spun in normal air [27].

Decreasing the pressure is not beneficial for electrospinning [24]. The polymer in the syringe is more likely to flow out. This increases the chance of unstable Taylor cones. Air in the solution will also cause bubbling of the solution at lower pressures, resulting in unstable jets. At too low pressure, there will be immediate discharge, which makes electrospinning impossible.

2.3 Controlling the fibre morphology

Electrospun fibres can be used for many different applications. In order to perform their functionality as efficiently as possible, different fibre morphology may be desired. Electrospinning is versatile enough to create fibres with a different form factor. This section explores the many possibilities.

2.3.1 Monolithic polymer fibres

Electrospinning first emerged with the spinning of monolithic polymer fibres. This method only requires a simple set-up and there are less parameters and interactions influencing the process. The final product is one continuous fibre deposited in a random manner to create a non-woven mat (see fig. 2.2a, unless the Taylor cone is not stable and the process is interrupted. If the spinning parameters are tuned well, the fibres will be consistent and smooth, with a uniform distribution of fibre diameters [31, 38, 51, 53]. As this method is relatively the oldest one, by now a lot of different materials have been spun and the influence of the different parameters is quite well known (see table 2.1), meaning that finding the right set of conditions for the desired fibre morphology is relatively easy. It is important to notice that the effects described in this section will continue to play a role when the electrospinning technique is evolving in order to create more advanced morphologies.

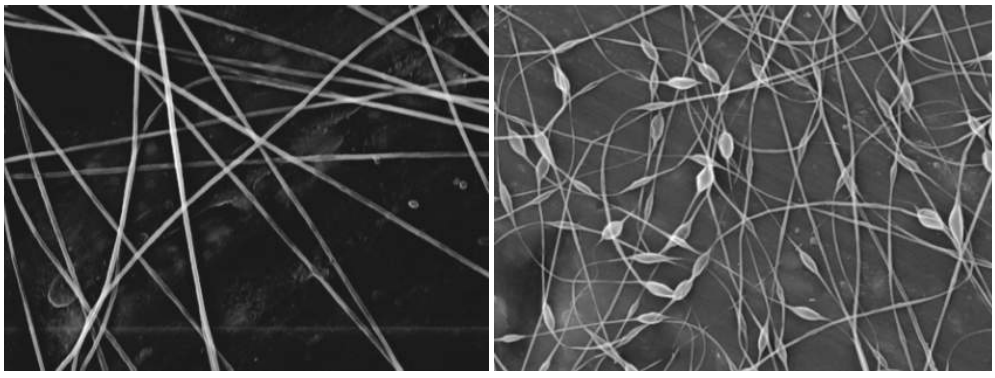

(a) ***(b)***

Figure 2.2: *Monolithic polymer fibres, spun under different conditions to create certain morphology [1]. 2.2a: Smooth fibres deposited in a non-woven fibre mat. This is the result most researchers are aiming for. 2.2b: By using a solution with a lower viscosity, the surface tension of the solvent will have a bigger effect on the process and more beads will appear.*

2.3.1.1 Beaded fibres

If needed, other fibre shapes can be produced by altering the parameters as described before. In this way it is possible to create fibres with a bead-on-string morphology [1, 43] (see fig. 2.2b. For

monolithic polymer fibres these beads are usually seen as imperfect fibres [23], as they are created when the electrospinning process is not stable enough. For multi-material fibres beads can act as compartments or capsules.

As smooth fibres can be created in a certain optimum range of parameters, beads will start to form when the limits of this range are reached. The main driver in formation of beads is the balance between viscoelastic forces of the polymer and the surface tension of the solution [1]. There are therefore easy ways to control the formation of beads: lowering the viscosity of the solution by changing solvent or decreasing the concentration of polymer, using a solvent with higher surface tension, such as water instead of ethanol, or lowering the voltage, which changes the degree of stretching. High voltages, however, may cause an unstable Taylor cone, which will also result in more beads [43].

2.3.1.2 Functionalised monolithic polymer fibres

The functionality of monolithic fibres can be expanded by mixing nanoparticles with the polymer solution [54]. During electrospinning, the particles will be drawn out of the needle together with the polymer and will end up in the fibre mat. Size of the nanoparticles will be crucial in determining if the particles will end up inside the fibres or if they will be present outside the fibres, between entangled fibres. Bead formation during the fibre spinning with nanoparticle loaded solutions may result in clusters of the nanoparticles at the bead location, but the right tuning of electrospin parameters in relation to particle shape and size can also result in nicely aligned particles [55]. It is important to realise that due to the addition of particles, the general viscosity of the solution increases. As discussed in section 2.2.2.1 this will have an effect on the electrospinning process. Simple dilution of the solution can prevent any unwanted effects, but it is a factor that needs to be taken into account.

Crespy et al. wrote an elaborate review on nanoparticles used in electrospinning [54]. They identify a lot of different types of nanoparticles, of different sizes in different polymer matrices. The main categories are: zero-valent metal particles like silicon, titanium, silver and gold, metal oxides, like TiO_2, SiO_2 and Fe_3O_4 and various inorganic markers. The polymer matrices are ones used more often for electrospinning of polymer-only monolithic fibres like PMMA, PVA, PVP, PLLA, PEO and PU. The different particles are added for different reasons, like hydrophobicity [56] or for creating conductive anode materials [35].

2.3.2 Biaxial fibres with continuous core

A second major morphology used in electrospinning are the biaxial core/shell, core/sheath or coaxial fibres. The process is referred to with different terms like coaxial electrospinning, cospinning or co-electrospinning. The goal of this process is to create fibres with a distinct core and a shell surrounding it. In general the core will consist of the functional material and the shell will provide protection for this active material or improve the interfacial interactions between the fibres and the matrix [29]. In essence the process is the same as for monolithic fibre electrospinning and it depends on the same parameters. All processes for creating core/shell fibres are therefore an extension on the monolithic fibre spinning. The set-up can have some slight changes compared to the monolithic fibres, and at this moment several approaches have been developed to create core/shell fibres.

2.3.2.1 Emulsion spinning

Although co-electrospinning, when it first emerged, made use of a coaxial spinneret with core/shell nozzle, the simplest way of creating a core/shell fibre is by use of emulsion electrospinning [29]. This process can make use of a simple one nozzle set-up like for monolithic fibres. Other advantages over other biaxial electrospinning techniques is the fact that it can reduce the amount of solvent needed or make it possible to use different solvents for the core and shell materials, which allows further control over the final fibres [57]. A drawback of the emulsion spinning, however, is that the emulsions are

only metastable and are likely to form larger droplets over time or completely phase separate [54]. This limits the shelf life of the solution.

Much like a system where solid nanoparticles are added to the polymer solution, a two phase solution is created and forced through a nozzle (fig. 2.3). Suspended droplets are sucked out of the nozzle when the shell material is sucked out as well. Due to large amount of stretching of the material, it is possible to create fibres with relatively small defects and discontinuous cores [58].

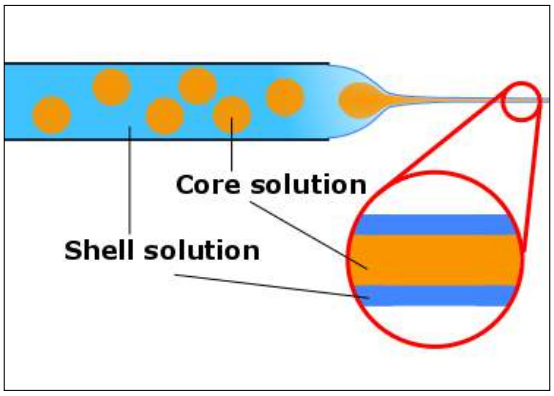

Figure 2.3: *Emulsion spinning process. The emulsion droplets are drawn into the fibres and end up inside the core when the fibre dries up.*

2.3.2.2 Biaxial fibre spinning

Biaxial electrospinning, or co-electrospinning, only emerged in 2003 [29]. For this process there are two different reservoirs of polymer solution and a needle-within-needle spinneret. The inner needle is connected to the core solution and the outer needle with the shell solution. During the process both solutions will be drawn from droplets on the end of the needle resulting in biaxial fibres as can be seen in figure 2.4. This was the first one-step process of creating core-shell structured nanofibres, which was advantageous over other processes like tubes-by-fibre-templates (TUFT) that require multiple processing steps [2].

Sun et al. managed to co-electrospin several materials in core/shell structured fibres, one of which is shown in figure 2.5 [2]. The diameter of the fibres depended a lot on the system, but it is mentioned that this can be tuned in similar ways as for monolithic fibres.

In general, all kinds of core materials can be used. Polymers, liquid agents or powders and even enzymes, proteins and other bioactive materials [59]. If the core is not spinnable in itself, adding a small amount of spinnable polymer to the core material can help in the production of the desired core/shell fibres.

As co-electrospinning uses two solutions, there is an interaction between the two. For instance, the shell and core solution can have different viscosities. This may lead to a difference in charge build up, flight time and stretching of the polymer. Settings that are favourable for one solution may be less favourable for the other.

Next to this, feed rate is important. As the shell material will have to cover a larger volume, due to the larger diameter, its feed rate should be higher than that of the core, which requires two different sources of pressure, for instance two syringe pumps, for both solutions. The extra dispensed volume will initially create thicker fibres, although this can also be tuned again to create relatively thicker cores with respect to the shell [60]. Co-electrospinning of biaxial fibres is, therefore, even more than for monolithic fibres a matter of varying parameters to create the desired morphology.

In 2009, this process was even further developed into triaxial fibres [61], with an outer shell, an intermediate layer and a core. This opens up more possibilities for applications, such as fibres for drug

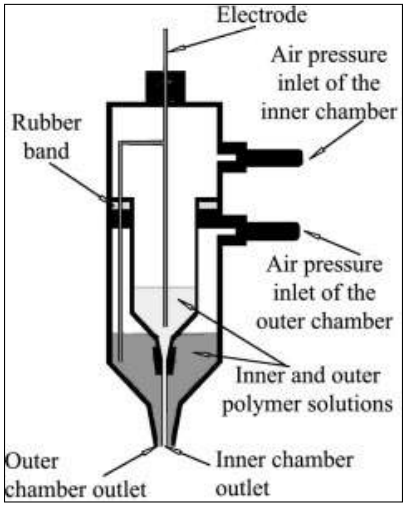

Figure 2.4: *Typical co-electrospinning spinneret as first introduced by Sun et al. [2]. Two different reservoirs are filled with a core solution and a shell solution. The needle-within-needle construction creates two-phase droplets from which core/shell fibres can be spun. The inlet pressure can be changed to change the feed rate in order to obtain a stable process.*

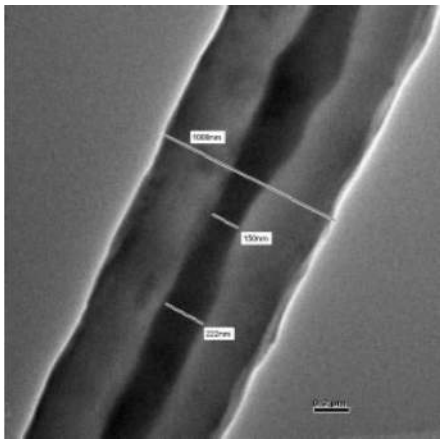

Figure 2.5: *TEM detail of one of the fibres spun by Sun et al. using a needle-within-needle spinneret [2]. The core of PDT is easy to distinguish from the PEO shell. The overall fibre thickness is around 1 micron, where the core has a diameter of around 200 nm. Scale bar 0.2 µm.*

release with different release rates [62], and fibres for a self-healing composite where different fibre layers contained different healing agent components [26].

2.3.3 Biaxial compartmented and capsule fibres

Much as for monolithic polymer fibres, during the spinning of biaxial fibres "defects" can occur. A lot of researchers try to create fibres filled with a continuous core of either solid polymer or liquid. During some of these processes however, the core either broke up into a discontinuous core or resulted in beaded fibres with encapsulated core solution. In practice these type of fibres can be seen as compartmented fibres or bead-on-string capsule fibres. The techniques behind this morphology are the same as for the biaxial fibres with continuous core [63, 64]. The limitations of the process can however result in fibres with a desired morphology for several applications, such as self-healing materials [39].

2.4 Electrospun fibres in corrosion protective coatings

2.4.1 Corrosion inhibitors and nanofibres

The recent works of Firouzi et al. and Covelo et al. are by the NovAM research teams knowledge the only researches that combined the use of corrosion inhibitors with the process of electrospinning [65, 66]. Even though the goal of the work was to increase corrosion protection, the fibres do not necessarily have the function of responsive carriers of inhibitor.

Firouzi et al. made nanofibres of PVA with 5 wt% cerium nitrate and cerium acetylacetonate [65]. The fibres were directly collected onto the substrate and some of them crosslinked by a thermal treatment. This simple coating was tested for its corrosion protective properties in a corrosive environment (3 wt% NaCl solution). Cerium release was measured with inductively coupled plasma mass spectrometry (ICP-MS). Adhesion of the coating was tested as well.

Covelo et al. made a coating system consisting of a layer of inhibitor loaded electrospun PVA fibres, combined with a sol-gel coating based on a presursor of 3-glycidoxypropyltrimethoxysilane (GPTMS) and 2-propanol and one of tetra n-propoxyzirconium (TPOZ) and ethylacetoacetate [66]. The fibres were used to reinforce the total coating. The fibres were loaded with either 1 wt% cerium nitrate or ceria (CeO_2) and spun using a biaxial spinneret where the inner solution was loaded and the outer solution was PVA only. This was done to ensure complete encapsulation of the inhibitor, thereby preventing premature release. The sol-gel coating was dip coated on top of the fibres. After immersion in saline solution (192 h), both loaded samples, but especially the ones containing cerium nitrate, showed better barrier properties than a blank sample with unloaded fibres and sol-gel coating, as shown by EIS.

Both works show initial steps into applying corrosion inhibitors in fibres as delivery system in corrosion protective coatings. Neither of the works investigate the corrosion protection from the perspective of using the fibres as responsive carrier, nor do they extensively investigate the parameters playing a role in improving the corrosion protection. This leaves an opportunity for this work to explore the proof of concept and its important parameters.

2.4.2 Protection by electrospun hydrophobic layers

Another approach, where electrospinning has been more extensively investigated is by creating hydrophobic layers. As the presence of moisture is necessary for corrosion to initiate, forming a hydrophobic layer on the metallic substrate can be an effective way to avoid corrosion.

In 2011 Grignard et al. showed a superhydrophobic coating layer made out of an electrospun fluorinated diblock copolymer [67]. The used polymer is poly(heptadecafluorodecylacrylate-*co*-acrylic acid)-*b*-poly(acrylonitrile) (P(FDA-*co*-AA)-*b*-PAN), a specially tailored copolymer. Fluorinated groups are known to have hydrophobic behaviour, the acrylic acid part has a good affinity with aluminium substrates, which ensures a stable adhesion over time. The electrospinning settings used did not result in fibres, but in structures varying from spherical particles, created by electrospraying, to interconnected structures on the microscale.

Other examples of electrospun hydrophobic layers are the work of Radwan et al. [56], who combined combined poly(vinylidene fluoride) (PVDF) with ZnO nanoparticles to create a hydrophobic structure, and Gong et al. who made a superhydrophobic mat of fibres based on a fluorinated polyimide (FPI) [68]. Neither of these examples, however, shows self-healing behaviour. One could, however, think of approaches where self-healing hydrophobic layers are created by encapsulating a reactive hydrophobic material into electrospun fibres, such as the silyl-ester of Garcia et al. [8].

2.4.3 Protection by barrier restoration

A final way to create a self-healing anti-corrosion coating is by providing a self-healing barrier. Providing a barrier is the main function of a protective coating and will prevent corrosion from initiating.

Electrospun fibres can be used as carrier to create a self-healing material based on the extrinsic healing principle. Park and Braun produced biaxial fibres via co-electrospinning [39]. Two reactive components were encapsulated in beads in two types of fibres and could be released upon damage to react and restore the barrier properties and protect against corrosion. Mitchell et al. used the same co-electrospinning approach in 2013 to produce PVA shell fibres with an epoxy prepolymer and an amine hardener encapsulated along bead-on-string- fibres [69]. Obviously, the encapsulation of a two component healing system can also be achieved with fibres with continuous core, as demonstrated by Lee et al. [70] by emulsion spinning, An et al. by coaxial spinning [71] or Zanjani et al. by triaxial spinning [26].

2.5 Conclusions

Electrospinning is a relatively easy and highly controllable process to make nanofibres. This allows it to be used for many different applications. Electrospinning has shown potential for creating corrosion protective coatings and even self-healing anti-corrosion coatings. The most heavily investigated approaches are based on forming (non-self-healing) hydrophobic layers or barrier restoration. Some initial steps have been taken to investigate corrosion inhibitors in combination with electrospun fibres, but these works have not explored the potential of using responsive fibres as continuous supplier of corrosion inhibitor inside a sophisticated coating system. Factors that influence the self-healing behaviour of coatings containing inhibitor loaded electrospun fibres have not been investigated in depth. This thesis seeks to elaborate on the potential of this concept.

Chapter 3

Materials and methods for electrospinning inhibitor loaded nanofibres

This chapter covers the experimental phase of making electrospun fibre mats. It elaborates on the set-up, the most important parameters that need to be taken into account during electrospinning and how changing solution and processing parameters changed the fibre spinning process.

3.1 Materials

3.1.1 Matrix material

As the idea of this concept was to create responsive fibres, poly(vinylalcohol) (PVA) (M_w=88,000 g mol^{-1}, 88% hydrolysed, Acros Organics) was chosen as fibre material. It is a water soluble polymer, a well known material for electrospinning [53, 55, 64–66, 69, 72–74] and has a low cost. PVA is in essence a chain of carbons atoms with -OH-side groups and has the linear formula [CH2-CH(OH)]$_n$. The repeat unit is shown in figure 3.1.

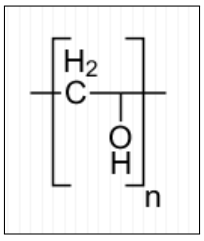

Figure 3.1: *The repeat unit of PVA is a simple carbon chain with one alcohol group.*

This gives the material the possibility to form hydrogen bridges and makes it easily soluble in water and in lesser extent soluble in ethanol. The material therefore dissolves in an aqueous (corrosive) environment, allowing the fibres to potentially release stored corrosion inhibitor. It also prevents the use of harsh solvents during production.

A final advantage of PVA is the fact that the hydroxy-groups can react with several other chemical sidegroups. This gives the advantage of being able to change the chemistry of the fibre matrix and modify the material to obtain desired properties. This can also be a disadvantage, as the fibre can react with functional materials inside or the coating matrix.

3.1.2 Corrosion inhibitors

Cerium chloride heptahydrate ($CeCl_3 \cdot 7H_2O$, >99.9% purity, Sigma-Aldrich), cerium dibutylphosphate ($Ce(dbp)_3$, synthesised as in [75]), and lithium carbonate (Li_2CO_3, >99% purity, Sigma-Aldrich) were investigated as corrosion inhibitors. The main focus of this work is on $CeCl_3$ as it is a well studied cathodic inhibitor for corrosion protection of aluminium [11, 14, 16, 76].

$Ce(dbp)_3$, a bifunctional organic/inorganic inhibitor [7, 77], and Li_2CO_3, which gained attention in the early 1990s as inhibitor for aluminium alloys [78] and recently regained attention [79], were selected to check the applicability of the proof of concept to other inhibitors. As the main focus is on $CeCl_3$ not all results on these inhibitors will be discussed in the body of this thesis. More details on electrospinning in general can be found in the appendix A.

3.1.3 Surfactants

In order to increase flow rates and with that production rates, surfactant (Triton X-100, laboratory grade, Sigma-Aldrich) or ethanol (analytical standard, Sigma Aldrich) were added to the solvent in order to reduce the surface tension [65]. A lower surface tension should allow for easier fibre formation with less beads and it might therefore allow for fast feed rates. The effect of the addition is dicussed in section 3.4.5.

3.2 Electrospinning set-up and key parameters

3.2.1 Equipment and set-up

As no prior electrospinning had been carried out at Aerospace Structures and Materials, the electrospinning set-up was developed and built during this project. Several improvements were made over time. The final set-up is presented here.

The three main parts of the set-up are a syringe pump (New Era NE-1000), holding 5 mL syringes and a needle (outer diameter = 0.9 mm, inner diameter = 0.6 mm), a power generator and an aluminium (foil) collector plate, much like the schematic in figure 2.1. The power was supplied by an Agilent U8002A DC power supply in combination with a Trek 609E-6 signal amplifier (max. output 10 kV) and a Spellman Bertan 205B-20R DC power generator (max. output 20 kV).

The needle and collector plate were connected to the power supply output and ground connection by a conducting wire and crocodile clip. To prevent charge build up on the metal case of the pump, with risk of sparking discharges between the needle and the pump, the housing was grounded as well. The whole set-up was placed in a polycarbonate box for safety and climate control. For humidity control a fan with a diameter of 120 mm was placed over a box with commercially available moisture absorbant (GAMMA) (see figure 3.3). The final set-up used can be found in figure 3.2.

3.2.2 Key parameters during electrospinning

In the previous chapter the most important factors infuencing the electrospinning process were identified. It is, however, also necessary to determine what parameters are important to pay attention to during electrospinning and what is the desired outcome. This makes it easier to determine the important parts of the set-up.

First of all, it is important to create uniform fibres. This means mainly the elimination of large scale visible defects, such as holes, weird topologies or collection of excess solvent. Next to that the fibres need to form a uniform network to be able to supply corrosion inhibitor everywhere in the coating. It is therefore beneficial to have fibres that roughly have the same size. The random deposition of the fibres will likely produce a uniform material on the macroscopic scale, but uniformly sized fibres

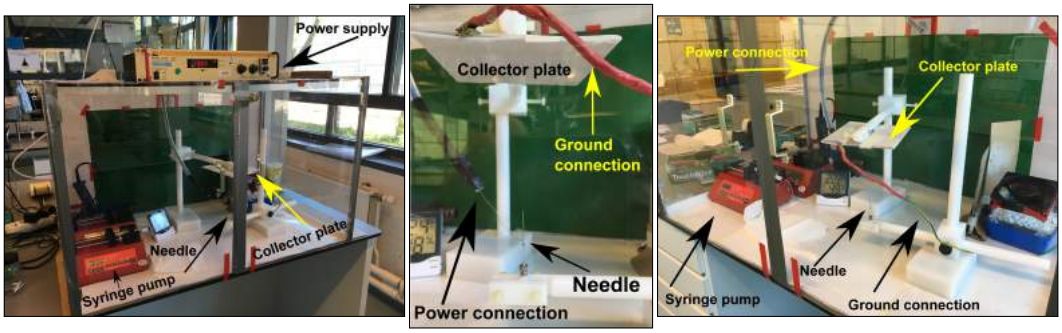

(a) *(b)* *(c)*

Figure 3.2: *The final electrospinning set-up used for creating nanofibrous mats. 3.2a: The total set-up with the power supply on top of the safety box and the red syringe pump clearly visible. 3.2b: Close-up of the needle and collector plate. Both the wire connection the power supply as well as the ground connection at the collector plate are visible. 3.2c Side view of the set-up with the clamps holding the needle and collector plate in place.*

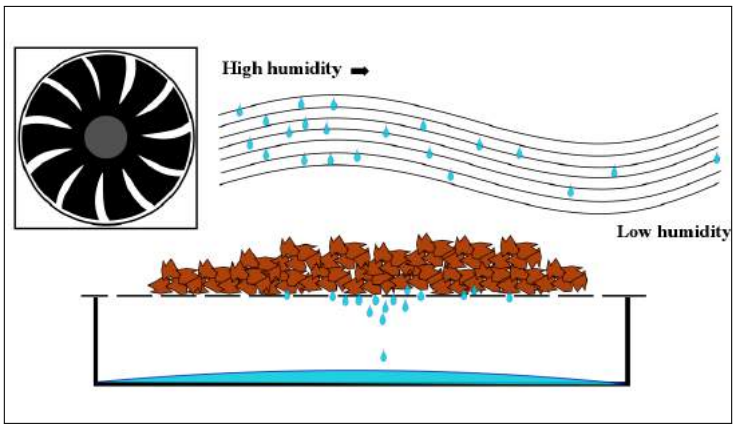

Figure 3.3: *Schematic of the device for controlling relative humidity of the air inside the electrospinning box. Air is blown over moisture absorbent salt and collected in a box, effectively removing moisture from the air.*

deposited in a relatively large area will aid in ensuring a fibre mat that also has an even thickness, throughout the sample.

A second requirement is that the results are reproducible. To allow testing of the influence of several fibre properties on the final anti-corrosion performance, it is important that the results obtained are actually caused by the parameters that are changed. Also "lucky" shots should be ruled out.

Next to that, the process should be fast. This is a relative term, but for electrospinning with a single needle the flow rates are typically $\leq$1.0 mL h^{-1} and ~90 wt% of the solution consist of solvent. This causes the actual amount of material deposited in the order of mg h^{-1}, making producing large quantities of thick fibre mats a time consuming process. For application, the mat will be in the order of tens of microns, which means long production times in the order of several hours. Avoiding this will be beneficial.

This automatically implies that the process should be stable over several hours. A stable process will give more uniform results as the effect of instabilities and subsequent changes in fibre quality will be canceled out by overall constant spinning conditions. A long term stable process also allows for the production of thick mats over a relatively large area, which means the same sample can be tested several times and the fibre mats can actually be applied in a coating. It also eliminates the forced presence of an observer to correct any instabilities during electrospinning.

In practice this means that the feed rate should be balanced with the other spinning parameters,

such that the speed at which material is ejected from the tip should match the material supplied. This keeps the process stable for longer times. Furthermore, the feed rate should be balanced such that the droplet on the needle tip does not dry up, thereby blocking the needle and destabilising the process.

Finally, it is also necessary to eliminate factors from the environment. It is therefore essential to have control over the ambient conditions during electrospinning. This mainly involves relative humidity and the related air temperature.

3.3 Methods

3.3.1 Preparing spinning solutions

Different polymer solutions were prepared by dissolving PVA powder in water under rapid magnetic stirring (600 rpm) for up to 24 hours. Concentrations varied from 4 wt% to 15 wt%. Dissolving PVA for concentrations of 12 wt% and higher took longer than 24 hours at room temperature. In order to fully dissolve the PVA within 24 hours, elevated temperatures of 60°C were used.

Some solutions were loaded with corrosion inhibitor from 5 wt% to 20 wt%. The inhibitor was added after dissolution of the PVA and simply stirred into the solution. The inhibitor is added by weight with respect to the PVA. The inhibitors are dissolved in solution in order to create the best dispersion. $CeCl_3$ easily dissolved creating a clear solution. $Ce(dbp)_3$ and Li_2CO_3 dissolve slower and have dispersed particles floating on top or suspended in the liquid.

3.3.2 Obtaining the right electrospinning parameters

The electrospinning process was explored by varying many parameters. These parameters and their variations, can be found in table 3.1. The starting point was always the polymer concentration in the solution. Subsequently, the parameters in table 3.1 were fixed, one at a time and the other parameters were varied in order to achieve stable spinning conditions of continuous fibres. So one would first fix the spinning distance and vary different potentials to achieve stable conditions for short term (<1 minute) spinning. Afterwards, the feed rate was adjusted to ensure a stable process for longer time (> 30 minutes).

The fibres were spun onto glass microscope slides to be checked under a Keyence VHX-2000E microscope. This gave a good indication of the quality of the fibre at the set parameters in terms of uniform thickness, bead formation and presence of excess solvent. Collection on aluminium foil was done to clearly check the deposition area and have an idea of the speed of the formation of a nice fibre mat. Collection on wax paper was carried out when full, thick fibre mats (~ 10 μm) were made, which needed to be peeled off, either to be tested for release kinetics (see chapter 4) or to be incorporated into coatings (see chapter 5).

Table 3.1: *Tested electrospinning parameters.*

Parameter		**Unit**	**Variations**
Polymer concentration		wt%	4, 5, 6, 7, 8, 10, 12, 15
Distance		cm	3, 5, 8, 10, 12, 15
Voltage		kV	6.0 - 20.0
Feed rate		mL h^{-1}	0.2 - 1.0
	H_2O	-	1
Solvent w_i	H_2O:EtOH	-	(0.5:0.5), (0.75:0.25), (0.9:0.1), (0.95:0.05)
	H_2O:Triton X-100	-	(0.989:0.011), (0.979:0.021)[1]
Inhibitor concentration		wt% to polymer	5, 10, 12, 15, 20
Inhibitor type			$CeCl_3$, $Ce(dbp)_3$, Li_2CO_3

The fibres were also investigated with Field Emission Scanning Electron Microscopy (FESEM) (JEOL-JSM-840) for high magnification imaging. As SEM makes use of a high energy electron scanning beam, the material which is investigated must be able to 'get rid' of any charges that build up on the material. Non conductive materials therefore need to be coated with a conductive layer. The polymer fibre mats were therefore, before placing them in the FESEM, stuck onto conductive carbon tape and sputtered with a 15 nm layer of gold.

3.4 Results and discussion

Starting point of the work was finding what set of parameters to use to spin monolithic PVA fibres. The second phase is adding the corrosion inhibitors and re-adjust the spinning parameters. Most important observations are discussed here.

3.4.1 Effect of polymer concentration

Lower concentrations of PVA, 4 wt% and 5 wt%, have too low viscosity to be electrospun into nice fibres. In this case there is not enough polymer material to form a continuous fibre when the surface tension is trying to force the solution into a droplet. This process therefore creates beaded fibres, as shown in figure 3.4a, or only droplets, meaning the solution is on the edge of electro*spraying* rather than electro*spinning*. From 6 wt% to 10 wt% electrospinning is possible and quite stable for longer periods of time. From 12 wt% and up, there seems to be a transition into the domain where fibre spinning becomes more difficult, as viscosity of the solution cannot be overcome by the electrostatic forces, which prevents fibres from forming, even at high potentials. Some polymer is collecting on the collector when the electrostatic forces are building up inside a big droplet and the entire droplet is pulled towards the collector instead of stretching into a thinner fibre, as shown in figure 3.4b. To remain safely in the spinnable domain, 8 wt% was chosen as concentration.

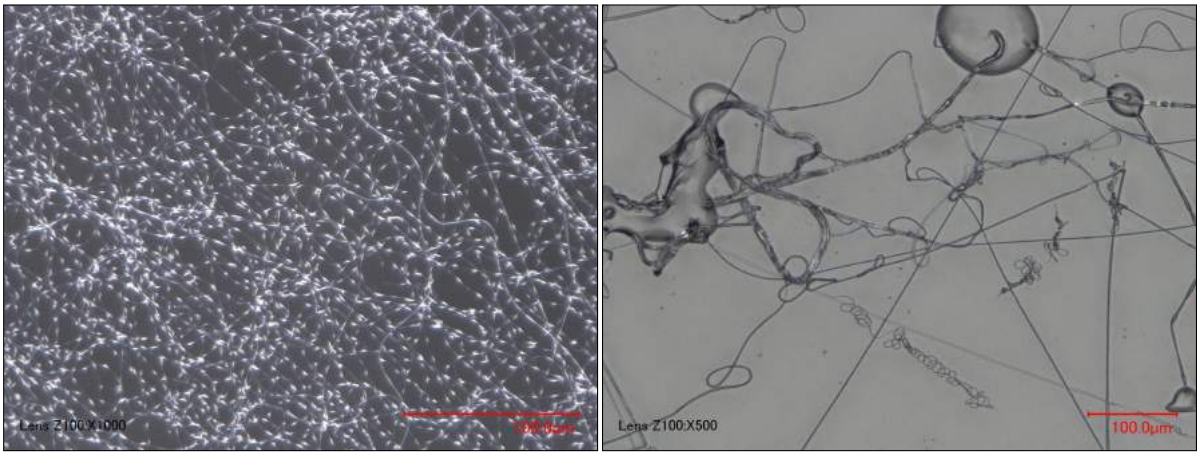

(a) ***(b)***

Figure 3.4: *Different fibre defects that occur at different polymer concentrations. 3.4a: PVA fibres spun at 4 wt%, 7.5 kV and 5 cm. These fibres show a lot of beads, the elongated blobs on the fibre. 3.4b: PVA "fibres" spun at 15 wt%, 6.5 kV and 3 cm. Very uneven fibres, droplets of solvent and polymer are all clearly visible.*

3.4.2 Effect of potential, distance and electrical field strength

In general, higher potentials will allow for faster spinning, as they will induce higher electrostatic forces on the solution. This will accelerate the fibre jet more, meaning that more material is being

[2]Corresponds to 1 and 2 wt% of total solution.

used in the same time frame and it is easier to create thicker fibre mats in a shorter amount of time, which is crucial for application purposes.

At very high potentials (>16 kV) however, the solutions became unstable and were hard to control, even when distances were increased to 15 - 20 cm. By reducing the potentials to the order of 12 - 15 kV this instability was overcome.

It was also necessary to carefully balance the potential with the distance to assure enough time for the solvent to evaporate. If the distance was too short, the water, being a high boiling point solvent, does not always fully evaporate, leaving droplets on the fibres. If large droplets of solvent are aggregating on the fibre mat up to the point they even start to flow, already spun fibres will be dissolved and an empty tear drop shape will be left in their wake.

Too large distances would, however slow the process down or prevent fibres from forming in the first place. For 8 wt% solutions, the electrical field strength or voltage/distance-ratios that worked well, were in the order of 0.9 - 1.1 kV cm $^{-1}$.

Another effect that was observed connected to the electrical field, was the influence of the collector plate. The size of the target was altered to try and steer the fibres more and make them deposit in a smaller area. Several aluminium collector plates with a thickness of 2 mm and an area between 25 and 144 cm^2 were used. The smaller collector plates created a smaller, less uniform electrical field, which increased the instability of the process. A larger target resulted in a more stable process, but showed a larger deposition area. This resulted in a larger but thinner fibre mat. To create reproducible, larger fibre mats for coating production, the bigger collector plates turned out to be better.

Based on microscope images, and later confirmed by SEM, good results were obtained with 13 kV at 12 cm for 8 wt% solutions. The feed rate of the syringe pump in this case was 0.4 mL h^{-1}. Figure 3.5a shows an SEM image of the fibres fabricated with these settings.

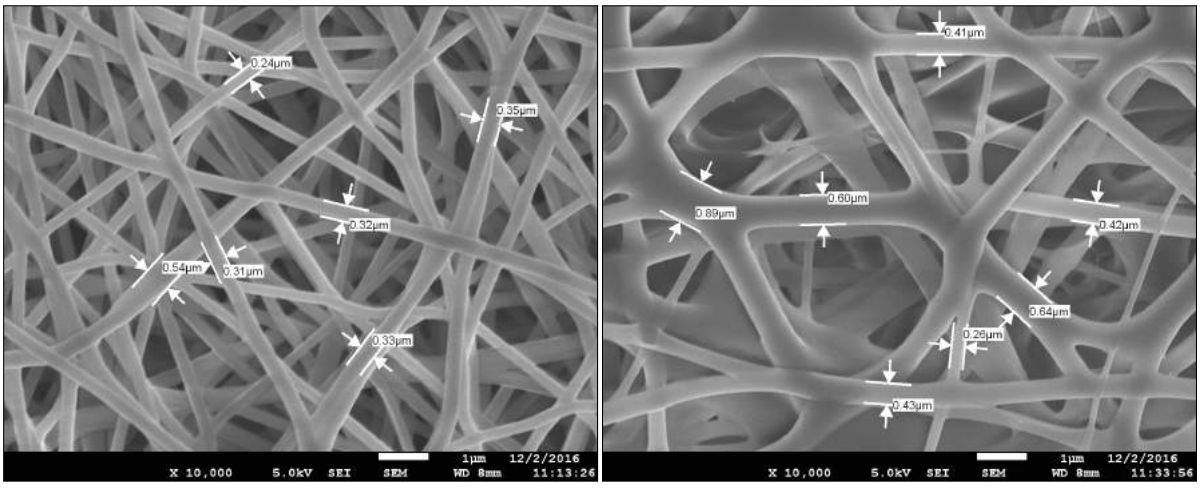

(a) ***(b)***

Figure 3.5: *Fibres spun at final selected parameters of 8 wt% PVA 13 kV and 12 kV. 3.5a: Pure PVA fibres spun at 0.4 mL h^{-1}. Fibre thickness is generally in the order of 300 - 400 nm. 3.5b: PVA fibres loaded with 10 wt% $CeCl_3$ spun at 0.25 mL h^{-1}. These fibres are thicker and more interconnected than pure PVA fibres.*

3.4.3 Effect of inhibitor addition

The direct influence of adding corrosion inhibitors to the solution is the increase in conductivity. By adding even small amounts of salts, conductivity can rise a lot. As mentioned by Zhang et al., increasing the amount of NaCl to a PVA/water solution from 0 to 0.185 wt% or 34.2 mM, increases the conductivity of the solution by a factor 18 from 0.58 to 10.5 mS cm $^{-1}$ [80]. When adding 10 wt%

$CeCl_3.7H_2O$ with respect to the polymer into the solution, the salt concentration is 0.525 wt% or 23.3 mM $CeCl_3$. This will therefore increase the electrical conductivity by a large amount as well. This has a large effect on the stability of the process.

The high conductivity of the solution, prevents using potentials over 14 kV, as the droplet on the needle tip becomes unstable very fast, even when the spinning distance is increased to distances as far as 20 cm. The instability also forces the feed rate to go down from 0.4 mL h^{-1} to 0.25 mL h^{-1} or even 0.15 mL h^{-1}, as a large droplet on the tip of the needle will become unstable very fast.

Another effect of increased instability is that there is also a limit on the inhibitor loading. Above 12 wt% inhibitor loading it was not possible to sustain a stable fibre spinning process for a prolonged (>15 minutes) period of time. Therefore, the maximum inhibitor loading was set to 10 wt%.

Figure 3.5b shows PVA fibres loaded with 10 wt% $CeCl_3$ spun at 13 kV and 12 cm with 0.25 mL h^{-1}. Even though more conductive solutions cause more stretching, the loaded fibres have increased diameters of 400 - 650 nm compared to the 300 - 400 nm of monolithic PVA fibres , which is likely due to the fact that the loaded fibres will have a shorter flight time towards to the collector plate, due the increased electrostatic forces, allowing less time for stretching of the fibres. One can see some branching of the fibres where they seem to fuse together and a larger distribution of fibre sizes. This might be induced due to more instability in the fibre during flight or the hygroscopic nature of the inhibitor that makes it more difficult for the solvent to evaporate. The distribution of fibres is less uniform than with monolithic PVA fibres, but is still good enough to create a uniform network of fibres. In this case, the fibres even form a more interconnected network of fibres, instead of only layers of fibres stacked on each other.

Finally, the increased conductivity also increases the deposition area, which is bigger for the inhibitor loaded fibres, as the instability of the flying fibre is higher due to the increased charges of the polymer jet. This makes the mats relatively thinner for the same amount of polymer solution used.

3.4.4 Effect of inhibitor type

As all inhibitors create ions when in solution, all additions of inhibitor create an increase in solution conductivity. This means that more instability is observed in all cases, as well as a larger deposition area. The amount of inhibitor mixed into the solution, however, depended greatly on the solubility of the inhibitor. $CeCl_3$ dissolves very quickly in the solution and can be added in large quantities as it has a solubility limit of $\leq$ 1000 mg mL^{-1}.

$Ce(dbp)_3$ on the other hand, being an inhibitor with organic part, dissolves both slower and in lower quantities into the solution. As mentioned by van Soestbergen et al. [81] the solubility limit of $Ce(dbp)_3$ is <1 mM at neutral pH, which corresponds to 0.771 mg mL^{-1}. This limits the loading of the fibres at 8 wt% PVA solutions to only 0.6 wt%. When the inhibitor loading is increased, the inhibitor will not dissolve and small particles will be suspended inside the solution. This gives the solution an opaque appearance. These particles can, nevertheless, be drawn out of the needle during electrospinning and therefore still end up in the fibre mat, be it as particles in between different fibre layers. Figure 3.6a shows this phenomenon. The limited dissolution of $Ce(dbp)_3$ therefore, has several implications.

First of all, the inhibitor is not shielded from the environment, which was one of the reasons to spin them into fibres. Secondly, the distribution of inhibitor within the fibre mat may be largely affected by the size distribution of the inhibitor particles. Lastly, $Ce(dbp)_3$ has the tendency to float, meaning that part of the inhibitor will not be suspended inside the solution but float on top, making it virtually impossible to know what the exact concentration is inside this solution. This makes it hard to draw any conclusions from later experiments.

Li_2CO_3 has a solubility limit of 12.9 mg mL^{-1} at 25°C [82], which is a lot higher than $Ce(dbp)_3$ but still limits the maximum loading of inhibitor with respect to 8 wt% PVA to 14.8 wt%.

The inhibitors were eventually chosen to be limited at concentrations 10 wt% w.r.t. PVA, as this

should supply enough corrosion inhibitor to protect a scratch, without pushing the limits of stable electrospinning.

$Ce(dbp)_3$ could be spun at the same conditions as $CeCl_3$, that is 13 kV, 12 cm and 0.25 mL h^{-1}. For Li_2CO_3 the final settings were different. Compared to the cerium based inhibitors it proved harder to find the right combination of parameters as small changes lead quickly to either too much solvent collection or an unstable or very slow process. The final conditions that provided good quality fibres, as shown in figure 3.6b are 20 kV, 15 cm and 0.15 mL h^{-1}.

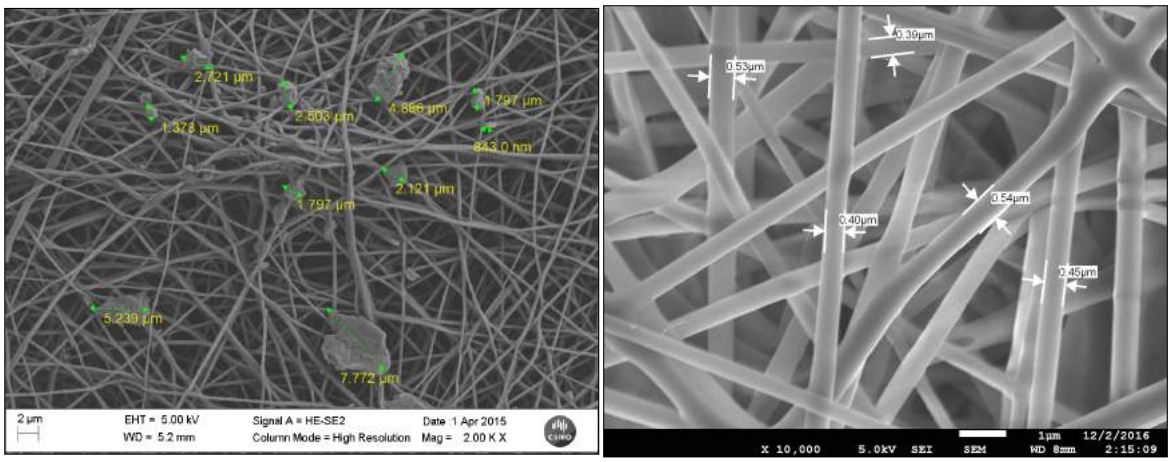

(a) *(b)*

Figure 3.6: *Fibres spun with different corrosion inhibitors. 3.6a: PU fibres loaded with 10 wt% $Ce(dbp)_3$. This is a SEM picture taken at CSIRO where different polymer/inhibitor systems were tried [75]. Even though the matrix material is different, the effect of inhibitor not dissolving and ending up in the fibre mat is the same. 3.6b: PVA fibres loaded with 10 wt% Li_2CO_3, spun at 20 kV, 15 cm and 0.15 mL h^{-1}.*

3.4.5 Effect of solvent mixtures and surfactants

As the addition of corrosion inhibitors forced the feed rate to go down, it was investigated if lowering the surface tension of the solvent or using a surfactant could aid in increasing the feed rates. During electrospinning this will make it easier for electrostatic forces to overcome the surface tension and electrospinning can start at lower potentials. As ethanol has a lower surface tension than water, adding it to the water can lower the surface tension [80]. As shown in table 3.1 several ratios of water and ethanol were explored in combination with different polymer concentrations.

The addition of ethanol seemed to have a positive effect on the feed rate. It was possible to increase the feed rate to 1.5 mL h^{-1} for H_2O:EtOH ratio of 0.75:0.25 for pure PVA fibres. This could, however not be maintained for a long time as the addition of ethanol increases the volatility of the solvent and caused drying of the droplet at the needle tip, blocking the supply of solution. Reducing the amount of ethanol also reduced the feed rate again which counters the desired effect.

The addition of ethanol to solutions with corrosion inhibitor, however, did not have the desired result as the solutions became more unstable again due to increased conductivity. This caused very beaded fibres or even electrospraying of droplets. This might be an unexpected result as reduction of surface tension should decrease bead formation. Zhang et al. however, explain such behaviour by the fact that EtOH is a worse solvent for PVA than water [80]. The viscosity of the solution is therefore also decreased, reducing the resistance of the polymer against bead formation. These competing mechanisms forced the feed rate to decrease again to the order of 0.25 mL h^{-1}. In other words the same result was obtained as before. This gives rise to the idea that the addition of so much conductive corrosion inhibitor ions and the instability this creates, has a bigger effect on the process than the

reduction of the solvent surface tension, rendering it an unsuitable solution.

A second attempt was the addition of a surfactant, Triton X-100, as used by Firouzi et al. [65]. With inhibitor loaded solutions however, voltages of 13 kV and higher would create electrospraying and no fibres would be formed, something that Firouzi et al. reported as well. It is probably caused by the surfactant that forces the fibres to ball up as it is resisting the solvent. Lower potentials and shorter distances however, caused either too much collection of solvent in the fibre mat or would reduce the feed rate again. Also in this case, feed rate could not be increased significantly and this route was abandoned.

3.4.6 Effect of ambient parameters

The humidity turned out to have a major effect on the quality of the fibre mats. As the weather in the Netherlands can be quite capricious, the ambient conditions in the lab could change quite a bit from week to week or even day to day. As water was used as solvent, having a high boiling point, high relative humidity (rH>50%) turned out to create fibres with solvent still present in the mat. For thick mats, this would create local wet spots, dissolving fibres, or created a sort of topology on the mat, probably caused by local flow of the material upon partial dissolution. Figure 3.7 shows two examples of fibre mats spun at different humidity levels.

This observation was the main reason to include the humidity control device inside the box. The relative humidity was in general reduced to 30% - 40%, which was in the order of 20% -25% lower than the outside humidity, which produced good quality fibre mats.

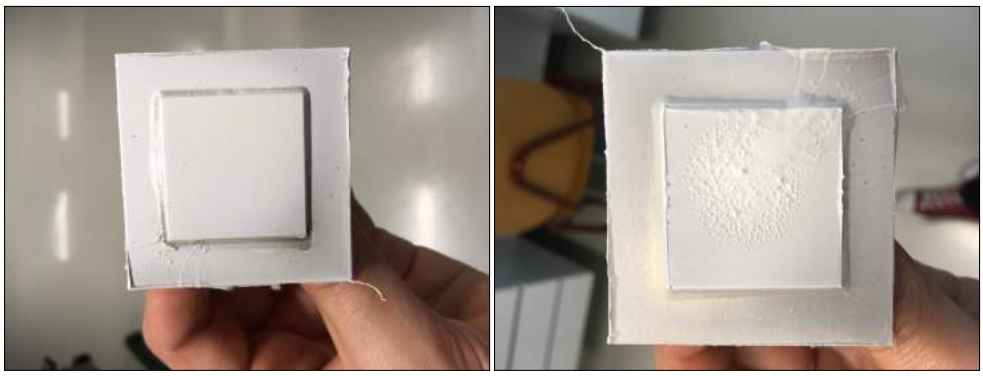

(a) ***(b)***

Figure 3.7: *Electrospun fibre mats spun with same parameters but different relative humidity levels. 3.7a: Fibre mat spun at low relative humidity (rH<45%). The result is a smooth fibre mat. 3.7b: Fibre mat spun at high relative humidity (rH>60%). There are defects forming on the surface and an unwanted topology is created.*

Temperature inside the box was the ambient temperature of the lab: room temperature. As the climate control in the lab is constant, the temperature was quite stable around 20°C. Small changes in the temperature did not have a significant effect on the process, other than slightly changing the relative humidity levels.

3.4.7 Other processing influences

Initially electrospinning was done in horizontal direction as depicted in 2.1a, as it has the benefit that droplets that form on the needle tip will fall down without hitting the collector. It was noted at potential higher than 10 kV, that part of the fibre material would fly back to the pump and deposit there instead of on the collector plate. This is due to the fact that the metal pump housing is grounded as well. This meant loss of material, slower production of thick fibre mats and less reproducible results.

A second observation was that, as the spinning fibres flies from the needle towards the collector plate it creates a cone shaped flight path. If the pump is, however, too close to the bottom of the box, the fibre will hit the bottom, sticks and starts to collect there, ruining the on-going process.

In order to solve these problems the needle was connected by a tube (diameter 1.5 mm) to the syringe. This allowed the needle to be placed further away from the pump, eliminating the influence of the pump housing. Next to this, it allowed the fibre spinning direction to be change to vertical instead of horizontal. This can be observed in figure 3.2b.

Top-to-bottom spinning has the benefit that it is easier to steer where the fibres will collect as gravity will help the fibres fall down and collect straight under the needle, where in horizontal spinning, the fibre flies in an arc-like downwards trajectory. The downside of top-to-bottom spinning is, however, that any droplets forming on the needle fall down onto the fibre mat, dissolving part of the fibres and destroying part of the sample. By spinning from bottom-to-top this problem is eliminated as well. This method was therefore chosen to give the best reproducible results.

3.5 Conclusions

It was possible to create electrospun PVA nanofibres loaded with inorganic ($CeCl_3$, Li_2CO_3) and organic/inorganic ($Ce(dbp)_3$) corrosion inbibitors by a self-developed electrospinning set-up. Many parameters, of both processing and polymer solutions, have been investigated on how they influence the electrospinning process. Solubility of the inhibitor has a big influence in how the inhibitor will be present in the final fibre mat. Inhibitors that do not fully dissolve in the solution will end up as particles between the fibres, while fully dissolved inhibitors will be mixed in the polymer network and give a uniform distribution within the fibre mat.

The presence of inhibitor salts inside the solution will have a large influence on the conductivity of the solvent. The increased conductivity shortens the flight time of the fibres, leaving them thicker than unloaded fibres. The stability of the process is reduced, limiting the applied potential and feed rate, slowing the process down compared to unloaded solutions. A practical maximum loading of around 10 wt% inhibitor with respect to the polymer matrix was found to give consistent results. The effect of inhibitor concentration seems to have a larger effect on the process than changing other solution parameters like surface tension or solvent volatility. Addition of ethanol or surfactant to the solution, therefore, did not yield in a faster, more stable process.

Ambient conditions, especially relative humidity, have a large influence on the quality of the fibre mat and control over these conditions is necessary to obtain reproducible results. This is most likely more apparent in this case due to the solvent being water, which has a high boiling point. With lower boiling point solvents the effect of relative humidity will be less pronounced as the volatility of the solvent is a lot higher and collection of solvent on the fibre mat is less likely.

Final settings for successful electrospinning can be found in table 3.2. These settings were used throughout the rest of the project.

Table 3.2: *Final electrospinning parameters.*

Fibre type	**Matrix conc. (wt%)**	**Distance (cm)**	**Voltage (kV)**	$\frac{\text{Voltage}}{\text{Distance}}$ **(kV cm^{-1})**	**Feed rate (mL h^{-1})**	**Inh. loading (wt%)**
PVA	8	13	12	1.08	0.4	0
PVA + $CeCl_3$	8	13	12	1.08	0.25	5, 10
PVA + Li_2CO_3	8	20	15	1.33	0.15	10

Chapter 4

Characterisation and release kinetics of $CeCl_3$ loaded fibres

From the previous chapter it is known that PVA nanofibres can be electrospun with corrosion inhibitor in the solution. The fibres can, however, only be of use in applications if the corrosion inhibitor is stored in the fibres and can be released again. This chapter covers the different characterisation techniques that were carried out to find out more about the chemistry of the fibres, the presence of corrosion inhibitor inside the fibres and the release kinetics of the inhibitor.

The release characteristics of the fibres will determine how much inhibitor is released, and how fast the concentration of inhibitor in aqueous environment will change. Both the speed of release and final concentration are important in order to achieve quick and long-term protection. The influence of inhibitor loading on the release kinetics, as well as the influence of modifying the fibre chemistry by (partial) crosslinking was investigated. (Partial) crosslinking changes the chemistry of the fibres and may aid in achieving a slower but longer sustained release, as well as reinforce the coating. The focus of this chapter lies on fibres loaded with $CeCl_3$ as Li_2CO_3 is not compatible for several of the characterisation methods in this chapter.

4.1 Materials

The fibre and inhibitor material were the same PVA and $CeCl_3$ from the previous chapter. Poly(acrylic acid) (PAA 63 wt% in water, Mw = 2,000 g mol^{-1}, Sigma Aldrich) and glutaraldehyde (GA) (50 wt% in H_2O, TCI Chemicals) were chosen as crosslinkers for the PVA, as both the carboxylic acid (-COOH) groups of the PAA [83–85] as the aldehyde (-CHO) groups of the GA [86,87] are known to react with the alcohol groups of the PVA to crosslink the material. Acetone was chosen as solvent for the crosslinking solution as it does not dissolve PVA nor $CeCl_3$ during the crosslinking process. 37% hydrochloric acid (HCl) was used to initiate crosslinking reactions.

4.2 Methods

4.2.1 Production of fibre mats

8 wt% PVA solutions were loaded with either mixed with 5 wt% or 10 wt% $CeCl_3$ and spun into fibre mats onto wax paper by using the settings as described in chapter 3. The solutions were spun for 1 hour or 0.25 mL in order to obtain fibre mats that were thick enough to be handled.

4.2.2 Crosslinking fibre mats

Two approaches were used in order to crosslink the PVA fibres. The first was crosslinking PVA with poly(acrylic acid) (PAA, $(CH_2CH(COOH))_n$), the second by glutaraldehyde (GA, $CH_2(CH_2CHO)_2$). As the PAA crosslinking was not a successful route, it is not further described here. Details can be found in appendix B.

For crosslinking with glutaraldehyde two approaches were investigated. Crosslinking in-situ during electrospinning, based on the work of Tang et al. [86] and crosslinking after electrospinning by immersion in a solution containing GA [87]. The first approach, which is also described in appendix B, was unsuccessful and will not be further discussed here.

For the succesful crosslinking method, 2 crosslinking solutions were prepared of 10 mM and 30 mM GA in acetone together with 0.01 M 37% HCl, to obtain partially and fully crosslinked fibre mats, as based on the work of Wang et al. [87]. After electrospinning the fibre mats were removed from the wax paper and placed in the crosslinking solutions of different concentration for 24 hours to obtain different levels of crosslinking. After the crosslinking time, the fibre mats were removed from the solution, rinsed with acetone and quickly dried under nitrogen gas flow and left to dry for another hour before characterisation or release measurements.

4.2.3 Fibre chemistry characterisation

The fibres were investigated with Field Emission Scanning Electron Microscopy (FESEM) for high magnification imaging and Energy-dispersive X-ray Spectroscopy (EDS) in order to do an elemental analysis using a JEOL-JSM-840. To prevent charging of the material, fibres were stuck onto conductive carbon tape and sputtered with a 15 nm layer of gold.

Further characterisation of the fibres was carried out by Fourier Transform Infrared Spectroscopy (FTIR)(Perkin-Elmer Spectrum 100) in order to follow the crosslinking reaction of the fibres and distinguish any changes in the molecular structure of the fibres. FTIR was carried out directly on the electrospun fibre mat from 4000 to 600 cm^{-1}.

4.2.4 Release kinetics measurements via UV/VIS

Release measurements of $CeCl_3$ were performed in-situ by UV/VIS spectroscopy with a Perkin-Elmer Lambda 35 spectrophotometer. This method measures the absorption of light at specific wavelengths in the visible (700 - 380 nm) and UV-light (<380 nm) range, in order to identify materials and determine their concentration. Light is sent through a monochromator to create light with a single wavelength. This light beam is splitted and sent through a reference sample and the sample to be measured. The light is detected on a detector behind the samples and the value of transmittance or absorbance compared to the reference sample is measured. Transmittance T is defined as the ratio of the transmitted intensity I over incident intensity I_0 [88, ch. 1].

$$T = \frac{I}{I_0} \tag{4.1}$$

More light is being absorbed when the path length of the light is increased. If a certain path length x absorbs 20% of the incident light, increasing the path length by a factor 2, will cause again 20% of the light to be absorbed. As after path length x only 80% of the incident light was left, the total absorption after $2x$ equals (20% · 100%) + (20% · 80%) = 36%. In order to take this exponential decay of total light absorption into account and make the relation between light intensity and path length linear, the absorbance A is defined by equation 4.2.

$$A = \log_{10}\frac{1}{T} = \log_{10}\frac{I_0}{I} \tag{4.2}$$

Beer-Lambert law (eq. 4.3) relates this absorbance of light, to the concentration c in [mol L^{-1}] of a material with a specific molar absorptivity ϵ in [m^2 mol^{-1}] times a given path length l in [m] [88, ch. 1].

$$A = \log_{10} \frac{I_0}{I_1} = \epsilon c l \tag{4.3}$$

From this relation it can easily be seen that an increasing concentration will show a linear increase in absorbance, making it possible to follow concentration over time.

In this work a quartz glass cuvet with a 10 mm path length was filled with 3 mL Milipore ® Elix 3 UV filtered water. For each measurement fibre mat samples, with a weight in the order of 6 - 25 mg, were folded up and placed in the solution in the cuvet. Due to their low weight, they would float on top of the water. By adding a small magnetic stirring device on the bottom (1000 rpm), as developed by Denissen [89], quick diffusion of any released material through the solution in the cuvet and subsequent uniform concentration distribution is guaranteed. The absorbance spectrum was measured in the UV-wavelength region from 325 to 200 nm. Every 2 minutes the spectrum was recorded.

4.3 Results and discussion

4.3.1 Characterisation of non-crosslinked fibres

Several non-crosslinked fibre mats were examined by EDS in order to check the presence of $CeCl_3$ in the mat. Appendix C shows several full EDS spectra. The PVA only samples show mainly presence of carbon and oxygen, as expected. The loaded fibres also show several cerium peaks between 4.5 and 6.5 eV, which become more visible when the loading of the fibres is increased. Chlorine is also detected as it is present in the inhibitor. Increase of inhibitor loading from 5 wt% to 10 wt% resulted in more prominent Ce and Cl peaks.

Figure 4.1 shows some of the elemental maps of a cerium loaded sample. They show a uniform distribution of cerium within the fibre mat. It is not possible to say if the cerium is mainly on the surface or also inside the fibres. The process of how the fibres are made would actually suggest both, as the cerium chloride is mixed in the solution in between the PVA molecules, it is likely that during the spinning the inhibitor is nicely distributed through the fibre, resulting in a uniform distribution of inhibitor in the fibre mat.

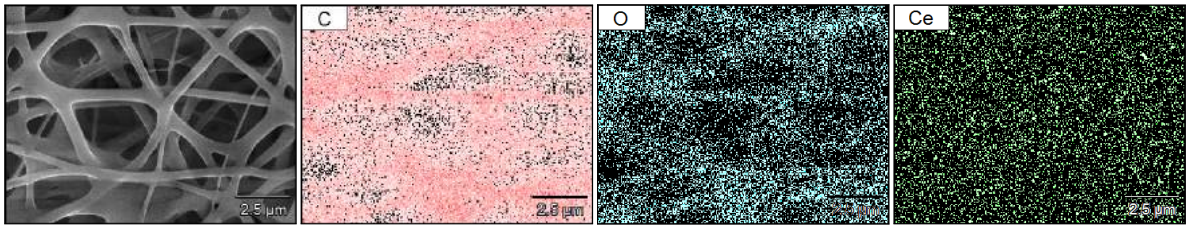

(a) *(b)* *(c)* *(d)*

Figure 4.1: *Elemental maps of $CeCl_3$ loaded PVA fibres. The main detected elements are the oxygen and carbon from the matrix material. Cerium can also be detected over the entire sample in a uniform fashion.*

4.3.2 Crosslinking of PVA fibres

In order for PVA to crosslink with GA, the aldehyde groups of the GA will, after initiation of the reaction by strong acid, react with the hydroxyl groups of the PVA chain, to form acetal bridges, as presented in figure 4.2.

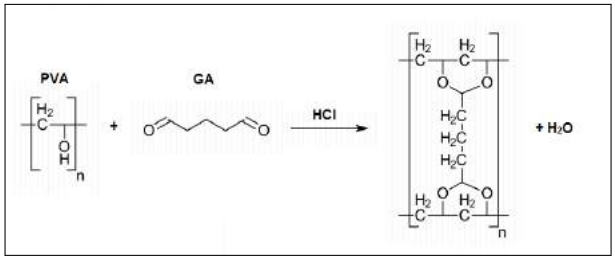

Figure 4.2: *The reaction between the PVA hydroxyl groups and the aldehyde groups of the GA is initiated by strong acid, acting as catalyst.*

The fibre mats were crosslinked in solution, which has the advantage that the fibres can be spun in the same way as before, therefore not changing the characteristics of the fibres before crosslinking is taking place. The method therefore also works with loaded fibres.

After removal of the fibres from the solution acetone starts to evaporate immediately due to its high volatility. It is observed that the fibre mats start to shrink. This effect is less prominent in fibres loaded with inhibitors than fibres spun with only PVA. This might indicate that there are interactions between either the PVA or GA with the inhibitors during crosslinking, or a reduced reaction between GA and PVA.

It was also observed that the all crosslinking solutions started to become yellow after 2 days, indicating a solution reaction is taking place. Crosslinking solutions were therefore never reused and new crosslinking reactions had to be made for every crosslinking reaction.

The fibre mats were placed in DI water to check their dissolution behaviour for several days. The partially crosslinked fibres (crosslinking in 10 mM GA) showed more swelling than the highly crosslinked samples. Especially on the thinner edges of the fibre mat it was possible to see the fibres become transparent and partly dissolve. Highly crosslinked fibres (24 hours crosslinking in 30 mM GA) did not show this behaviour. After several days of immersion both fibre mats were still intact, indicating that the crosslinking had been successful.

4.3.3 Characterisation of crosslinked fibres

4.3.3.1 SEM and EDS

Figure 4.3 shows different crosslinked fibres. When comparing the crosslinked fibres to the non-crosslinked fibres from the previous chapter, it is visible to see that the size of the fibres does not really change for unloaded fibres (fig. 4.3a). For loaded fibres, which were already more interconnected, it seems that the fibres are a bit thicker (fig. 4.3b).

Next to this, the unloaded mats are not flat anymore after crosslinking. This contraction of the fibres was visible on the macroscopic scale as shrinking of the fibre mat. This contraction will most likely cause some internal stresses in the fibres. This shrinking is more visible for unloaded fibres, which might be related to he fact that the loaded fibres are more entangled and interconnected, which might prevent the shrinking.

Finally, it was observed that the loaded fibres crosslinked with 10 mM GA do not have a smooth surface, like the other fibres (fig. 4.3c). It seems that the surface has cracked, which could be due to internal stresses in the fibre network during crosslinking [90]. This surface roughness will increase the surface area of the fibre mat a lot.

The fibres were also observed after exposure to water. A droplet of water was placed on the fibre mats and left to evaporate for an hour. The pure PVA fibres dissolved and disappeared completely, the 10 mM crosslinked fibres became transparent, and the 30 mM crosslinked fibres did not show a difference by the naked eye. Figure 4.4 shows the fibres after the exposure to water.

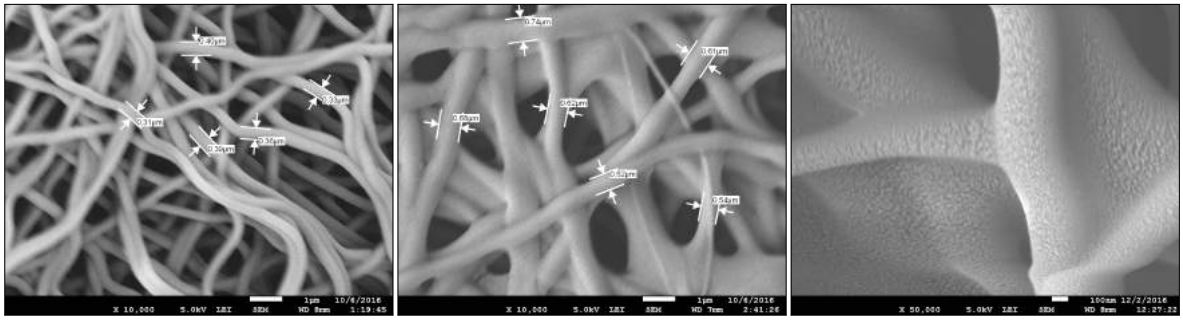

(a) *(b)* *(c)*

Figure 4.3: *Several crosslinked fibre systems. 4.3a: Unloaded PVA fibres that have been crosslinked with 30 mM GA. These fibres show the shrinking of the fibres. 4.3b: PVA fibres with corrosion inhibitor that have been crosslinked with 30 mM GA for 24 hours. 4.3c: Close up (50,000 x) of PVA fibres with corrosion inhibitor that have been crosslinked with 10 mM for 24 hours. There are surface features visible.*

Figure 4.4a shows the edge of exposure to water of 10 mM crosslinked fibres. It is clear that the fibres have swollen a lot, effectively losing the overall fibre shape and turning into cohesive film of PVA. This explains the transparency of the fibres after exposure, as the light will not scatter off the fibres anymore. Figure 4.4b shows the 30 mM crosslinked fibres after water exposure. These fibres seem not to be affected too much, as the fibre size is still in the same order of magnitude as before wetting. The interfaces are, however, not as sharp as before.

EDS results for all crosslinked fibres were very similar to the non-crosslinked samples. Cerium can still be detected and is still uniformly distributed through the fibres. The spectra can be found in appendix C.

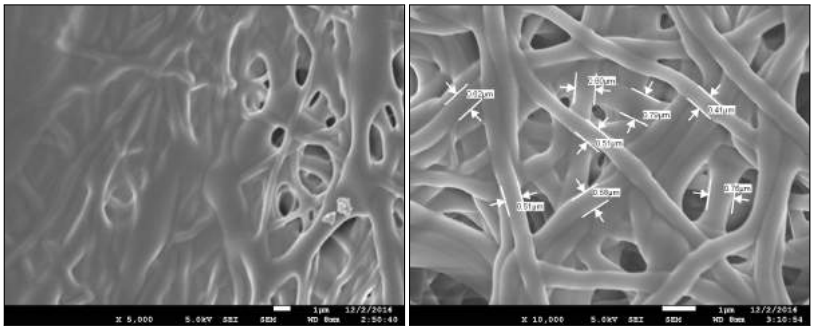

(a) *(b)*

Figure 4.4: *Loaded and crosslinked fibres after 1 hour exposure to water. 4.4b: 10 mM crosslinked fibres. 4.4b: 30 mM crosslinked fibres.*

4.3.3.2 FTIR

Figure 4.5 shows the FTIR spectra of three different types of fibre mat. By crosslinking the fibres in solution with 30 mM GA for 24 hours, the spectra show some clear differences with the original spectrum. First of all there is a reduction of the broad peak at 3300 cm^{-1} which is associated with the hydroxyl groups of PVA [91, 92], indicating that part of the functional groups have reacted with the GA.

Secondly, we see a second peak appearing between 2800 and 2900 cm^{-1}. This can be associated with the -CH in an aldehyde, and could indicate excess GA or an unfinished reaction, where only one functional group of the GA has reacted [91, 92], as well as the alkyl chain in the GA. The band at

1141 in PVA, giving this peak a shoulder is related to the C-O bond determining crystallinity of the material. Between 1150-1085 typical C-O-C bonds can be observed which are both visible in PVA and PVA/GA combinations. Changes in this range can be related to the formation of acetal bridges which are slightly different from the C-O-C bonds in PVA [92].

The $CeCl_3$ loaded crosslinked fibres show a spectrum very similar to the PVA/GA spectrum, but with minor changes. There is for instance a stronger peak at 3300 and the peak between 1100 and 1000 is less sharp. These two changes may indicate a slight change in the formation of the acetal bridges or less reacted OH-groups. This could mean that the cerium is forming complexes with either the PVA or the glutaraldehyde, reducing the reactivity and thus the amount of crosslinking.

There are, however, clear signs that the PVA has crosslinked with the GA, which is also shown by the fact that the fibres no longer fully dissolve in water. There might, however, be slight weight loss in the fibres, but this was not investigated.

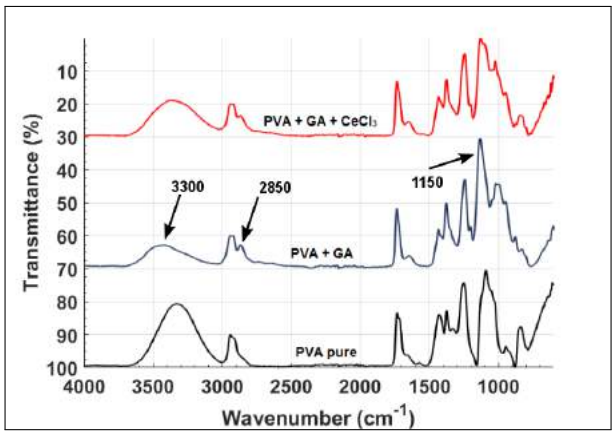

Figure 4.5: *FTIR spectra of pure PVA, crosslinked PVA and loaded crosslinked PVA. The reduction of the peak at 3300, the appearance of the peak at 2850 and the difference in peaks between 1000 and 1100 are indications of the presence of GA in the sample and successful crosslinking with the PVA.*

4.3.4 UV/VIS spectroscopy for measuring accurate $CeCl_3$ release from fibre mats

4.3.4.1 Spectra and calibration of constituent fibre materials

In order to be able to determine the concentration of $CeCl_3$ in solution, it is necessary to identify the absorbance spectrum of $CeCl_3$. Based on distinct peaks, a calibration curve can be constructed from which it is possible to determine the concentration. More details about this calibration curve can be obtained in appendix D.

Figure 4.6a shows typical absorbance spectra of $CeCl_3$. Four distinct peaks can be observed at λ = 211, 222, 239 and 253 nm respectively. Next to this, a smaller bump can be observed around λ = 300 nm. This is in agreement with observations of van Soestbergen et al. as absorption spectrum for cerium [81]. Outside of the peak regions the absorbance is practically zero. The relation between the peak intensity and the concentration is a linear one, as predicted by equation 4.3. The peak at λ = 253 nm gives the most sensitive response the a change in concentration of cerium in solution and was selected as wavelength for making the calibration curve and for following cerium release.

Pure PVA also shows absorbance in the UV-light range. As shown in figure 4.6b, PVA has a very strong absorbance where $\lambda < 240$ nm. This absorbance behaviour in the more blue wavelengths regions can be caused by a scatter phenomenon. If the particles or molecules are smaller than the wavelength, they can cause part of the light to scatter and therefore not reach the detector. This causes the scattered light to be observed as absorbance [93]. This effect becomes more apparent at higher concentrations. Next to the sharp absorbance below λ = 240 nm a small bump can be observed around

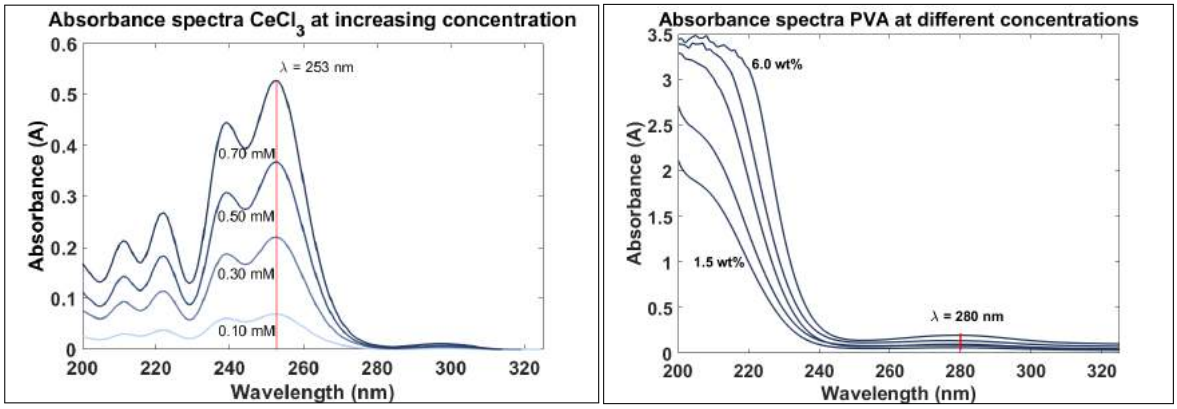

(a) *(b)*

Figure 4.6: *Typical absorbance spectra for constituent fibre materials. 4.6a: Typical absorbance spectra for $CeCl_3$. The cerium ions give a clear response in the UV-light range where four distinct peaks can be observed at 211, 222, 239 and 253 nm. There is a clear linear relation between the peak height and the concentration of the solution, which in this plot ranges from 0.05 mM to 0.7 mM. 4.6b: Typical absorbance spectra of pure PVA. There is a strong response at wavelengths below 240 nm. The small bump at $\lambda = 280$ nm shows a linear relation with concentration.*

$\lambda = 280$ nm, which shows a linear relationship with respect to the concentration of PVA. A calibration curve can therefore be constructed for PVA at $\lambda = 280$ nm. This curve can be found in appendix D.

4.3.4.2 Spectra of inhibitor loaded fibre mats

When dissolving multiple components in the same solvent, the molar absorptivity ϵ of the total solution will change. When the spectra of the different components partly overlap, they will influence each other and the combined spectrum of the two materials will have contributions of both materials. Figure 4.7a shows increasing spectra of both PVA and cerium. It is clear that the spectra overlap and, especially at $\lambda < 240$ nm will have a strong influence on each other.

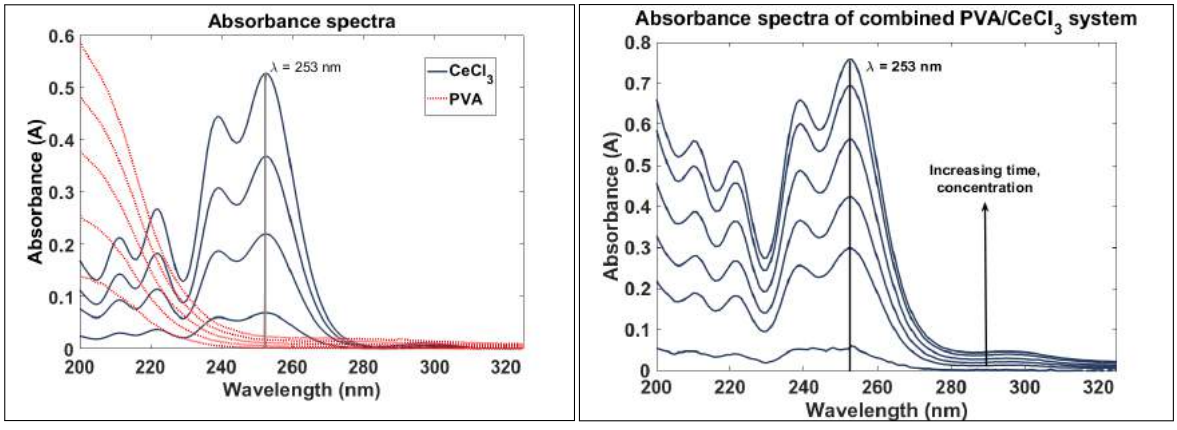

(a) *(b)*

Figure 4.7: *Absorbance spectra for increasing concentration of different compounds. 4.7a: The response of the individual components show a clear overlap in absorbance spectra, especially $\lambda < 240$ nm. At $\lambda = 253$ nm the overlap is not very large. 4.7b: The response of loaded PVA fibres over time. The features from both PVA and cerium are visible in the absorbance spectrum.*

Figure 4.7b shows a typical response of dissolving $CeCl_3$ loaded PVA fibres over time. It can be observed that the new, combined spectra have indeed characteristics of both the PVA and $CeCl_3$ ab-

sorbance spectra. The four peaks from cerium are still observed, but the strong absorbance $\lambda < 240$ nm of the PVA is also present. The 211 nm peak is consistently higher than the peak at 222 nm, which does not correspond with the spectra of pure $CeCl_3$. Also, a general background can be observed at wavelengths $280 < \lambda < 295$ nm and $\lambda > 305$ nm. This background is not present in $CeCl_3$ spectra, but only in the PVA absorbance spectra.

4.3.4.3 Correcting the spectra of fibre mats for release kinetics studies

The spectra of PVA and $CeCl_3$ affect each other and shift the entire spectrum upwards. This means that the calibration curve made for $CeCl_3$ at $\lambda = 253$ nm is no longer valid as the combined spectra will overestimate the presence of cerium. Therefore, the part of the light absorbance caused by PVA needs to be identified and corrected for. For the analysis of multicomponent systems one must make two important assumptions [88, sec. 3.2].

i) The contributions of the absorbance are additive by superposition.

ii) The Beer-Lambert Law is still obeyed after mixture of the two materials.

In this way the total absorbance of light measured would be simply the combination of the two:

$$\begin{aligned} A_{total} &= A_{PVA} + A_{CeCl_3} \\ &= \epsilon_{PVA} C_{PVA} l + \epsilon_{CeCl_3} C_{CeCl_3} l \end{aligned} \tag{4.4}$$

One can, therefore, subtract the response of the PVA from the total light absorbance to obtain the response caused by cerium. In order to achieve this, it is necessary to predict the absorbance of PVA over the entire wavelength range. As mentioned before, at $\lambda = 280$ nm PVA shows a linear relation between absorbance and concentration in the solution. As $CeCl_3$ does not absorb light at $\lambda = 280$ nm, we can assume that all the light absorption in a combined spectrum at this wavelength is caused by PVA and use this as a reference.

As long as Beer - Lambert's Law is obeyed, and the absorption increases linearly with concentration, the shape of the absorbance spectrum will remain the same. This implies that the ratio of absorbance caused by PVA at 280 nm $A_{\lambda_{280}}$ and any other wavelength A_{λ_x} will remain constant and can be used to reconstruct the entire PVA absorbance. For wavelengths where Beer - Lambert's Law is not obeyed, this method will not work, as the reconstruction of the PVA absorbance spectrum will not be correct. By checking calibration curves of PVA at different wavelengths it can be determined if absorbance at that wavelength follows Beer - Lambert's Law.

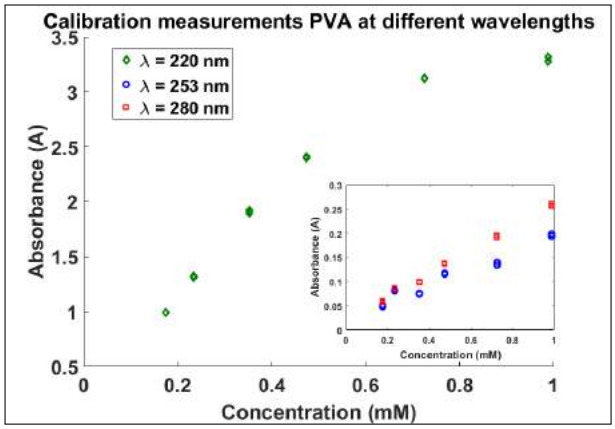

Figure 4.8: *Calibration measurements of PVA at different wavelengths. The inset shows the linear relation between concentration and absorbance at $\lambda = 253$ nm and $\lambda = 280$ nm. At a lower wavelength ($\lambda = 220$ nm), however, there is no linear relationship anymore.*

Figure 4.8 shows the calibration measurements of PVA for different wavelengths. For λ = 280 nm (calibration wavelength PVA) and λ = 253 nm (calibration wavelength $CeCl_3$) the absorbance of PVA follows a linear relation, indicating that Beer - Lambert's Law is followed and the ratio between PVA absorbance at λ = 253 nm and λ = 280 nm is constant. At lower wavelengths, however, such as λ = 220 nm the behaviour is non-linear and the construction of the PVA spectrum based on its value at λ = 280 nm will likely be prone to errors.

Figure 4.9a shows the ratio of absorbance for a PVA sample at every wavelength with respect to the absorbance at λ = 280 nm. This plot shows the average ratio with the standard deviation, based on 400 different PVA absorbance curves. For $\lambda > 240$ nm the uncertainty is in the order of several percent. Below this wavelength, where the PVA absorbance starts rising fast, we can see that the uncertainty also increases due to the non-linear absorbance behaviour in this wavelength region. When we zoom in at λ = 253 nm, shown in the inset in figure 4.9a, it is shown that the uncertainty at this wavelength is a lot smaller. In fact, the margin of error in predicting the absorbance here is ± 4%.

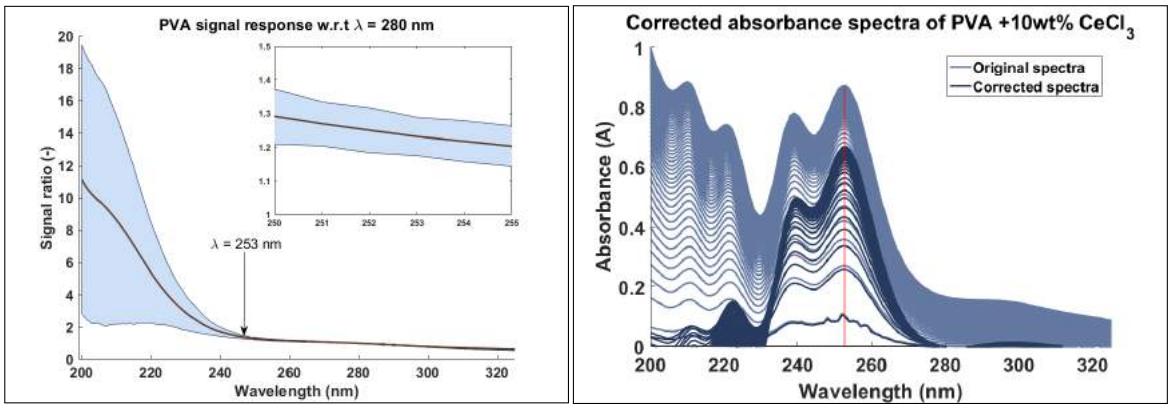

(a) ***(b)***

Figure 4.9: *Steps taken in correcting the combined UV/VIS spectra for the absorbance caused by the dissolution of PVA. 4.9a: This image show the predicted absorbance spectrum of PVA normalised to a wavelength of λ = 280 nm, including margin of error. The inset shows a detail of the area around λ = 253 nm. It is clear that when the wavelength is decreasing the uncertainty increases a lot. Around λ = 253 nm, however, the margin is ± 4%, which is acceptable. 4.9b: This image shows the effect on the measured spectra after a correction has taken place. All the spectra are shifted down, to show a response that shows only the effect of $CeCl_3$.*

With the ability to predict the PVA absorbance we can now subtract this response in every measurement of inhibitor loaded PVA fibre mat spectra to obtain the response caused by cerium alone. Figure 4.9b shows such a correction on the spectra. As expected the entire spectrum is shifted downwards again. This means that all the peaks shift downwards, any absorption at λ = 280 nm is eliminated and the small peak at λ = 300 nm becomes visible again. Below λ = 235 nm the correction becomes more aggressive and the peaks at λ = 222 and 211 nm are reduced enormously. This corresponds to the bigger uncertainty in predicting the PVA signal. At the λ = 253 nm peak the correction is more precise. By following the absorbance at λ = 253 nm over time, the release kinetics of cerium can be determined.

To validate the method of correction several measurements were checked by ICP-OES to determine the concentration of cerium. The ICP values were all within the correction margin of error of ± 4.0%, proving that this correction method can be applied with sufficient accuracy.

4.3.5 Analysing the effect of inhibitor loading on release kinetics

The first analysis of release kinetics was to study the effect of loading of $CeCl_3$, by measuring the release of 5 wt% and 10 wt% loaded fibre mats. The results, normalised to the fibre sample weight,

are shown in figure 4.10a.

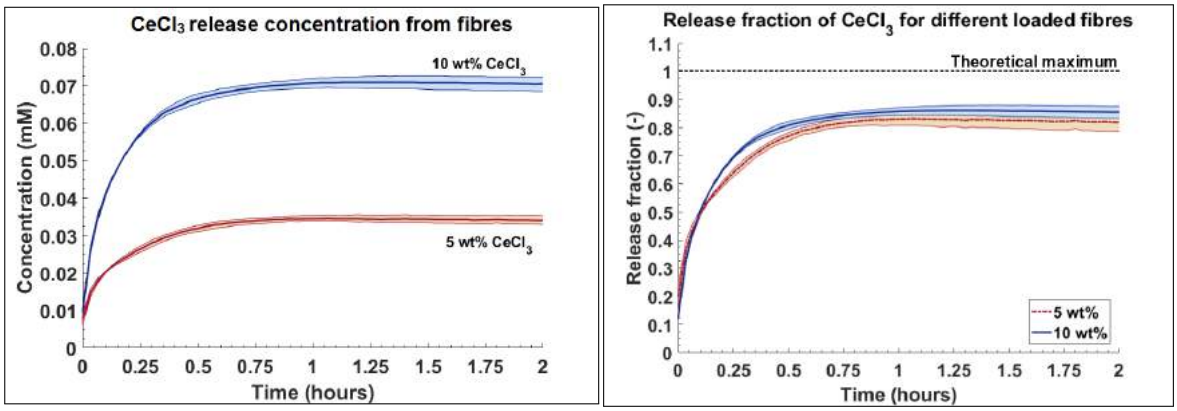

(a) ***(b)***

Figure 4.10: *The release kinetics of electrospun PVA fibres with different loadings of $CeCl_3$. 4.10a: Image showing the effect of inhibitor loading on the final concentration in solution. Concentration values are normalised to a sample weight of 1 mg of loaded PVA fibres. 4.10b: This graph shows the release as fraction of the total theoretical amount of inhibitor present inside the fibres. The release mechanism seems to be very similar for both systems.*

From this graph it is clear that there is a big effect of the concentration on the amount of corrosion inhibitor that is released. The final concentration is twice as high for the 10 wt% loading as compared to the 5 wt% loading. This is expected, as twice as much inhibitor is available inside the fibres.

Both samples show a difference in the rate at which the concentration of cerium changes. One might expect that the PVA dissolves at the same rate for both samples, thereby releasing the inhibitor at a similar rate. As $CeCl_3$ dissolves more or less instantly at these concentrations, it is unlikely that the dissolution of cerium is a limiting factor. It is clear however, that the concentration of inhibitor at the same time instants are very different. After 0.25 hours the 5 wt% samples have released about 0.027 mM, while the 10 wt% loaded sample has released about 0.055 mM at this point. It therefore seems that the speed of release is related to the amount of inhibitor available. This is in agreement with Fick's first law for steady-state diffusion.

$$J = -D\frac{d\varphi}{dx} \tag{4.5}$$

Where the diffusion flux J in [mol m^{-2} s^{-1}] is related to the diffusion coefficient D in [m^2 s^{-1}] and concentration φ [mol m^{-3}] at position x [m], as long as the flux remains constant. It is clear to see that a larger initial concentration difference between the corrosion inhibitor loaded fibres and the solution will induce a higher initial diffusion flux, thereby changing the concentration of inhibitor in solution more rapidly for higher loaded fibres.

Fick's second law also takes changing diffusion flux into account by stating that the change in concentration over time depends on the second derivative of the concentration in space:

$$\frac{\partial\varphi}{\partial t} = D\frac{\partial^2\varphi}{\partial x^2} \tag{4.6}$$

This means that a certain concentration difference will cause a certain diffusion flux, which in turn will reduce the concentration difference which reduces the diffusion flux again etc. This causes a diffusion flux that will reduce slower and slower over time. Higher initial diffusion flux will reduce relatively fast, while a low initial diffusion flux will reduce slower. In release terms this means that the release will slow down over time, where high initial release will slow down relatively fast compared to slower initial release.

We can take away this effect by normalising the release kinetics to the mass of the inhibitor and showing the release as fraction of total theoretical maximum inhibitor loading $\frac{M_t}{M_\infty}$. Figure 4.10b shows the release of $CeCl_3$ for different loaded fibres as function of this release fraction. It is clear that both samples show very similar release kinetics. Up to 55% release the lines coincide almost perfectly and above 80% the error margins of both systems overlap, indicating a very similar behaviour. This leads to the idea that a difference in inhibitor concentration will lead to a difference in the speed at which concentration changes, but not in the mechanism at which the inhibitor is released. This is an indication that the carrier of the inhibitor has the biggest influence on the way of release.

It is clear here that release never reaches the theoretical maximum of 100%. This is a puzzling result as the fibres have completely dissolved. All the encapsulated inhibitor should therefore be released. As the reduction in release fraction seems to be consistent over all measurements, the effect is most likely caused by processing or measuring errors.

A possible explanation is that the cerium forms a complex with the PVA such that it cannot be measured by UV/VIS. The fact that ICP, where atoms are completely free to move as they are turned into plasma [94], gives the same results as the UV/VIS makes the formation of complexes unlikely.

Another explanation might be the fact that the prediction of amount of $CeCl_3$ in the fibres is off and the loading is a little lower than expected. There are multiple possible reasons for this to happen. First of all $CeCl_3$ is a strong hygroscopic salt, even when weighing and handling the salt, it will attract moisture from the air. This may affect the amount that is actually weighed and reduces the amount of inhibitor added to the solution.

A second problem may be that when adding small amounts of inhibitor, in the order of mg, a small deviation has a relatively large impact on the final loading. Even though handling the inhibitor was always done carefully it is possible that something went wrong during solution preparation. As the maximum release fraction has small scatter this is not very likely.

Finally, it is possible that during spinning, the concentration of inhibitor is not constant. It is possible that when the solvent is evaporating, part of the inhibitor, being dissolved in the water is also evaporated or expelled during the rapid spinning of the fibre, meaning that a small amount of inhibitor will be lost.

4.3.6 Analysing the effect of fibre crosslinking on release kinetics

As crosslinking of the fibres is supposed to reduce the dissolution rate of the fibres, the crosslinking is expected to have an effect on the release kinetics of added corrosion inhibitors. Figure 4.11 shows the release kinetics of $CeCl_3$ when released from fibres with a different level of crosslinking.

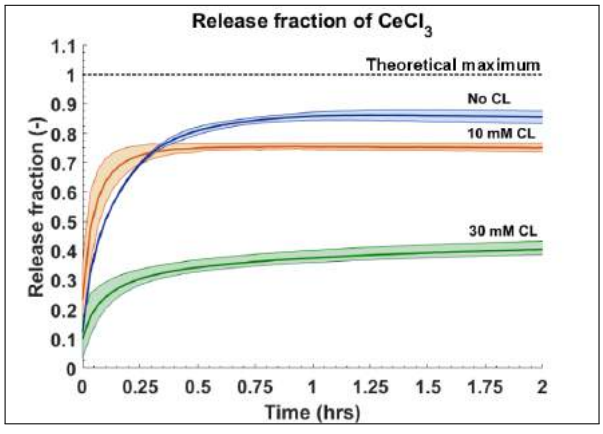

Figure 4.11: *Release kinetics of $CeCl_3$ loaded PVA fibres with various degrees of crosslinking.*

As the degree of crosslinking is increased, the final fraction of released inhibitor is decreased. Even only partial crosslinking results in a reduction of inhibitor release of about 10%. Further crosslinking reduces the release further by more than 30%. This can indicate that part of the inhibitor is trapped inside the polymer network when crosslinking has been introduced.

Surprisingly the release from the partially crosslinked fibres seems to be faster in the first 15 minutes. There is an initial burst release which is faster than for non-crosslinked fibres. The release, however, also levels out faster, which allows the non-crosslinked fibres to "catch up". This initial burst behaviour might be caused by the cracked surface of the partially crosslinked fibres, as shown in figure 4.3c, which gives the fibre a higher surface area and easier diffusion paths for encapsulated cerium to diffuse into the solution.

The release of the 30 mM crosslinked fibres is notably slower than in the other cases. This is a more expected result, as the swelling and dissolution of the fibres will be reduced notably. This will affect the release rate.

4.3.7 Describing the release kinetics with a model

In order to further understand the kinetics some fitting has been carried out. There are many models describing release kinetics, which are often linked to drug release [95]. One of the most often used models to describe the release kinetics drug release based on dissolving polymer carriers and diffusion is the Peppas-Korsmeyer model [90,96,97]. This models has also been used to describe release of corrosion inhibitors [98]. The basis of the model is a simple power law derived from one-dimensional diffusion under perfect sink conditions:

$$\frac{M_t}{M_\infty} = k t^n \tag{4.7}$$

Where M_t is the mass released at some time t, M_∞ is the total mass of inhibitor and k is some dimensionless constant taking into account macromolecular characteristic of the materials, t the time and n the diffusional exponent that relates to the kinetics mechanism. For planar geometries pure Fickian diffusion is observed for $n = 0.5$. If one, therefore, plots the release against the square root of time, pure Fickian behaviour will show as a straight line. This model is, however, only valid for the first 60% of release fraction, but can give an indication of the release mechanism [96,97,99].

The release from soluble polymer fibres, as in our case, is, however, more complicated than just diffusion. Processes like swelling, erosion and dissolution will affect the release behaviour. To account for this behaviour, the model is expanded and equation 4.7 will change to include a second term as suggested by Ritger and Peppas [99]. This leads to equation 4.8, that was used to fit the release of corrosion inhibitors from fibre mats. The exponent will still determine the release mechanism. As non-crosslinked PVA completely dissolves in water and partially crosslinked PVA shows swelling this model will provide a better fit.

$$\frac{M_t}{M_\infty} = k_1 t^n + k_2 t \tag{4.8}$$

.

The exact value of the exponent may change based on the geometry of the dissolving container. Ritger et al. identify that the exponent may change from 0.43 to 0.45 to 0.50 for spherical, cylindrical and planar geometries respectively [97]. But even these exponentials can change based on their actual geometry, size distribution aspect ratio etc.

The fitted release curves of the different samples plotted against the square root of time are shown in figure 4.12. Up to 60% release all curves show linear behaviour. The complete curves can be fitted with equation 4.8. Table 4.1 shows the coefficients of the fitted curves.

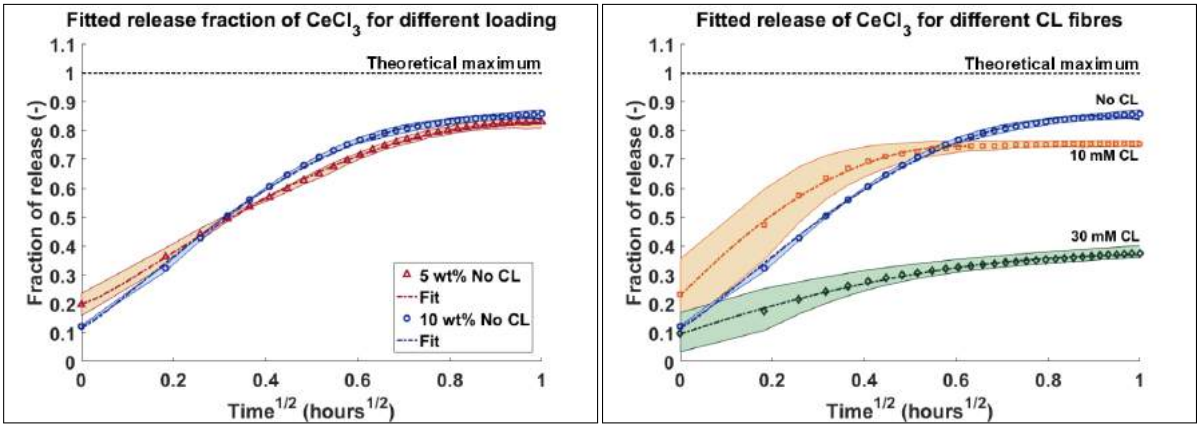

(a) *(b)*

Figure 4.12: *Release of $CeCl_3$ plotted against the square root of time and fitted with equation 4.8.*

Table 4.1: *Coefficients related to the release kinetics of cerium loaded PVA fibres.*

Inh. loading	Crosslink	k_1	n	k_2
5 wt% $CeCl_3$	No	1.82	0.645	-1.19
10 wt% $CeCl_3$	No	2.10	0.600	-1.38
10 wt% $CeCl_3$	10 mM	1.80	0.519	-1.51
10 wt% $CeCl_3$	30 mM	0.554	0.506	-0.281

Although the entire process of solvent diffusion in the fibre, swelling, erosion and dissolution of the matrix and diffusion of the inhibitor through the fibre is a complicated process, equation 4.8 allows for a good fit of the data as well as being a good description of the release mechanism. A few trends can be identified from the coefficients in table 4.1. First, all samples show behaviour that is not purely Fickian diffusion. Especially the non-crosslinked samples show release coefficients indicating anomalous, non-Fickian release behaviour, which can be related to the high relaxational processes in the swelling polymer, which will speed up the release. Increasing the crosslinking reduces the influence of swelling on release and the highly crosslinked sample shows almost pure Fickian release, indicating that swelling does not play a big role in the release of inhibitor.

A second trend is that increasing the amount of crosslinking reduces the kinetic constants k, which are related to the macromolecular structure of the material and final release concentration. The trend that crosslinking lowers the kinetics is to be expected as part of the cerium can be trapped in the crosslinking network and the swelling is reduced.

The difference between the two differently loaded fibre mats could be related to the macroscopic geometry differences between the different loaded fibre mats in terms of pore size and effective surface area for instance or the fact that several processes are happening at the same time, influencing each other.

4.4 Conclusions

In order to achieve slower, sustained release and reinforced coatings, crosslinking of the PVA fibres might be useful. Different levels of crosslinking were achieved by crosslinking inhibitor loaded fibre mats in a solution of acetone with 10 mM or 30 mM GA.

Subsequently, the release of cerium loaded fibre mats was measured in-situ via UV/VIS. As cerium and PVA have overlapping absorbance spectra, it is necessary to correct for PVA in determining the final cerium concentration. By predicting the PVA signal and subtracting it from the total absorbance

spectrum, it is possible to retrieve the cerium response and have an accurate prediction of the cerium concentration as confirmed by ICP.

The effect of inhibitor loading and crosslinking on release kinetics were investigated. Difference in inhibitor loading will change the final concentration levels and speed at which the concentration changes but not the release mechanism. This is related to Fickian diffusion behaviour, which states that the speed of diffusion is related to the concentration gradient.

The effect of increasing crosslinking is a reduction in inhibitor release. Partially crosslinked fibres show an initial burst release, likely caused due to their cracked surface. Heavily crosslinked fibres show a slower and lower release, likely due to trapping of cerium in the polymer network.

The release curves were fitted with an expanded Peppas-Korsmeyer model, which includes relaxation phenomena of polymers, caused by swelling. Non-crosslinked fibres have a anomalous release exponent, indicating that swelling plays a role in speeding up initial release. Higher crosslinking density reduces the influence of swelling and shows more Fickian release. The kinetic constants are decreased with increasing crosslinking, indicating slower release.

Chapter 5

Protective coating systems from inhibitor loaded nanofibre mats

In the previous chapter release of inhibitor was studied and parameters influencing release were investigated.The final step was to incorporate the fibres in a coating system and test the protective characteristics of the fibres when embedded in a coating system. First the methods of creating coatings including the loaded fibre mats will be explained, as well as the methods to test the anti-corrosive properties and the post mortem characterisation of the samples. The influence of several parameters on the corrosion protective properties were tested. The fibre mat was placed at different positions inside the coating systems to test if coating composition plays a role. Next to this, the effect of crosslinking the fibre mats, which affects the release kinetics was analysed. Finally, the influence of different inhibitor types were investigated.

5.1 Materials and methods

5.1.1 Materials

The fibre mats incorporated in the coatings were spun as described in chapter 3. For the coatings 10 wt% loaded fibre mats loaded with $CeCl_3$ or Li_2CO_3 were used. The substrate used was unclad aluminium AA2024-T3 with a thickness of 1.5 mm. The top coating was an epoxy/amine system consisting of Epikote 828 and Ancamine 2500 provided by Akzo Nobel. Xylene with a purity of 99% was purchased from J.T. Baker and used as solvent for the epoxy/amine. NaCl with a purity of > 98% was purchased from VWR Chemicals and used in the electrolyte. All aqueous solutions were prepared using Milipore® Elix 3 UV filtered water.

5.1.2 Methods

5.1.2.1 Substrate preparation

First, the substrates were prepared in order to ensure a reproducible surface conditions and good adhesion of the coating as described by Ferrer et al. and Denissen [21, 89]. Samples of 30 x 30 mm were cut by a Darley sheet cutter. Subsequently, the sheets were grinded down with silicon carbide sandpaper with decreasing roughness (grit 180P and 320P) in order to remove the native oxide layer. Next step was bringing back some surface roughness by Scotch Brite 3M "Clean N Finish grade AVFN", followed by degreasing with acetone. As final step the sheets were immersed in 2.0 M NaOH for 10 seconds, immediately rinsed with DI water and quickly dried under nitrogen air flow. The NaOH is used to increase the number of hydroxyl groups on the surface of the aluminium, which has a positive effect on the chemical bonding of the organic coating with the surface [100].

5.1.2.2 Coating preparation

The coating was prepared by mixing the epoxy and amine precursors in a ratio of 1:0.58 by weight, ensuring stoichiometric ratio of the reactive groups. Xylene was added as 20 wt% of the total solution to reduce the viscosity of the mixture, making it easier to create thin coatings. The components were mixed in a high speed shear mixer for 5 minutes at 2500 rpm to ensure complete mixture. The coating was applied immediately after mixing.

To apply the coating on the substrate, a spin coater was used. Spin coating is a process to create thin coatings by using centrifugal forces to disperse a material over a substrate and aid in evaporation of the solvent. Figure 5.1 shows the spin coating process.

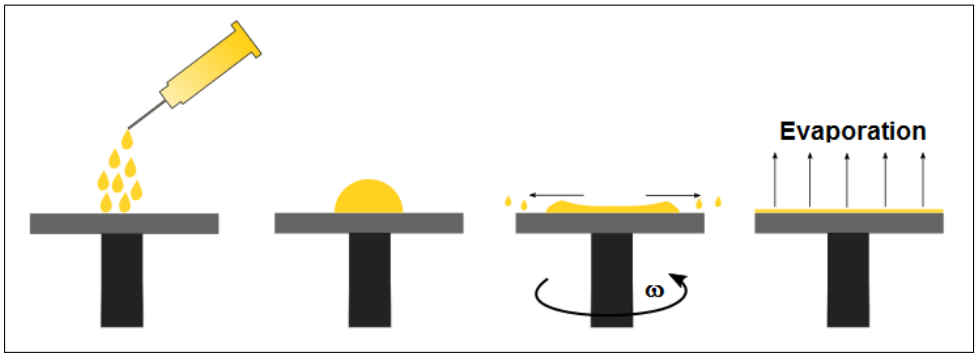

Figure 5.1: *The spin coating process. First a mixture of material and solvent is added onto the substrate. By rotation the solution is forced outwards and any excess material is spun of the substrate. This spreads and thins the coating layer. After evaporation of the solvent a thin coating layer is left.*

Substrates were secured in the spin coater with vaccuum suction and a droplet of epoxy/amine/xylene mixture was applied on top (0.3 mL). Subsequently the substrate was rotated at 1500 rpm for 30 seconds. The centrifugal forces aid in dispersing the coating material nicely over the substrate and evaporating the solvent. This leaves a thin epoxy film. The process was repeated three times in order to get a nice uniform layer over the surface. Subsequently the coatings were placed in an oven at 60° C for 24 hours to cure. Thickness was subsequently measured with an Eddy current meter.

Table 5.1 summarises the different samples that were tested. To keep the discussion concise, only the highlighted samples will be discussed in detail, showing the influence of crosslinking the fibre mat and changing the inhibitor type. The influence of coating composition on passive and active corrosion protection can be found in appendix E.1 and E.2.

Table 5.1: *Different coating samples that were tested with their most important characteristics. To clarify the naming: numbers represent the loading of the fibres in weight percent,* Ce *and* Li *are linked to the inhibitor type,* NB B *represent "no base layer" or "base layer" and* CL *denotes "crosslinked" fibres. The highlighted samples will be discussed this chapter.*

Sample name	Base layer (μm)	Fibre mat (μm)	Inhibitor	Crosslinked fibres	Total thickness (μm)	Coating type
Unprotected	-	-	-	-	50 ± 3	A
10CeNB	-	30 ± 5	$CeCl_3$	-	75 ± 5	B
PVAB[1]	7 ± 1	60 ± 5	-	-	180 ± 15	C
10CeB1	7 ± 1	50 ± 5	$CeCl_3$	-	105 ± 15	C
10CeB2	6 ± 1.5	200 ± 5	$CeCl_3$	-	220 ± 10	C
10CeBCL1	6 ± 1.5	60 ± 5	$CeCl_3$	partial	180 ± 20	C
10CeBCL2	6 ± 1.5	60 ± 5	$CeCl_3$	full	120 ± 15	C
10LiB	6 ± 1.5	60 ± 5	Li_2CO_3	-	140 ± 15	C

The coatings can be divided in three types of coatings, which can be found in figure 5.2. Coating type A does not contain any fibres, coating B has fibres directly spun unto the substrate and coating type C has a base layer between the substrate and the fibre mat. In order to make these last coatings, the base layers were applied by spin coating at 7000 rpm and cured for 24 hours. Subsequently, a thin layer of epoxy/amine was spun onto the cured base layer at 9000 rpm to act as "glue" between the baselayer and the fibre mat, which was placed on top of the wet epoxy/amine. After 2 hours of curing the top coat was applied at 1500 rpm.

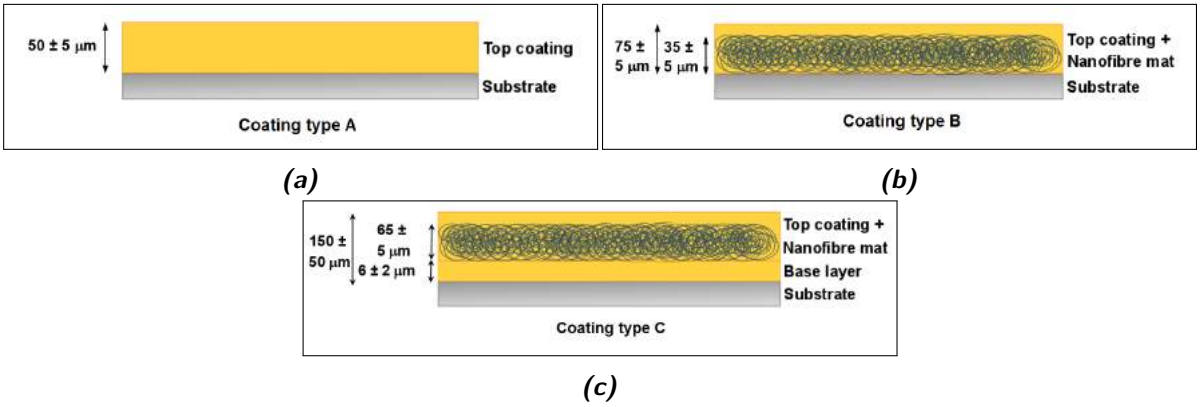

Figure 5.2: *Composition of the tested coatings. 5.2a: The control coating consisting of a simple epoxy/amine barrier without any protective elements. 5.2b: The first coating with loaded fibres. The fibres are directly spun unto a preparated substrate and covered with epoxy/amine top coating. 5.2c: Coatings that contain a base layer between the fibre mat and the substrate.*

5.1.2.3 Scratching of the coating

In order to investigate the protective capabilities of the coating, all samples were intentionally damaged by making a scratch through the coating onto the substrate. In order to achieve reproducible scratches a CSM scratch tester was used which can control the force applied to make a scratch. The scratches were made with a Rockwell indenter with a diameter of 100 μm. The scratches were made by making multiple passes with increasing force until the substrate is reached. For each increase in force 3 passes were made. The unprotected sample was sequentially scratched at 5, 10, 12 and 15 N. Coatings up to 180 micron were sequentially scratched at 5, 10, 12, 15 and 20 N. Thicker coatings needed force up to 30 N. 10LiB was scratched with a razor blade, as the scratch tester was out of commission at that time. The scratch was therefore wider than in the other samples. The scratch length was 5 mm and the scratch rate 10 mm min^{-1}.

5.1.2.4 Opto-Electrochemical Impedance Spectroscopy (EIS)

The long term corrosion behaviour of both damaged and undamaged coatings were analysed by immersion in corrosive aqueous 0.05 NaCl solutions. A hyphenated opto-EIS set-up, containing a three electrode electrochemical cell with an attached microscope camera, was used for this analysis. This set-up, developed by Mathis [101] and improved by Denissen to investigate self-healing anti-corrosive coatings [89], allows for simultaneous impedance tests and in-situ optical monitoring of the corrosion process. The electrochemical cell consists of the scratched sample as working electrode, a carbon counter electrode and a Ag/AgCl double junction reference electrode. The cell is controlled by a potentiostat (Autolab PGSTAT 302N) in order to measure both Electrochemical Impedance Spectroscopy (EIS) and Open Circuit Potential (OCP). The applied potential amplitude is 10 mV (RMS)

[1] Reference sample

over OCP in order to keep the response of the system (pseudo)-linear. The investigated frequency range is 10^{-2} to 10^{5} Hz.

For the hyphenated opto-EIS, the webcam is placed opposite of the sample. An image is recorded every 99 seconds for the length of the measurement. The cell is placed inside a Faraday cage in order to minimise interference with the environment. As systems are very unstable during initial submersion in the corrosive environment, OCP is measured continuously during the first 30 minutes, followed by EIS. Subsequently, OCP was measured for 10 minutes followed by EIS every immersion hour.

5.1.2.5 Post-mortem characterisation

After immersion all samples were examined with SEM and EDS in order to examine the scratched surfaces and carry out elemental mapping. The same SEM and EDS methods as described in chapter 3 were used.

Next to this, several samples were analysed by a Renishaw InVia Raman spectrophotometer with a green laser at 532 nm to detect cerium oxides and copper-rich phases. Several areas were mapped based on 3 sequential measurements of 1 second at a magnification of 50x and 100% laser power. The peaks used to identify cerium oxides and copper-rich phases are around 461 cm^{-1} [102] and 620 cm^{-1} [103] respectively. The inspected wavenumber range was 300 to 1000 cm^{-1}.

5.2 Results and discussion

5.2.1 Coating preparation

In order to obtain smooth coating layers, several spin coating parameters were tested in combination with various additions of xylene. It is important that the surface is nice and smooth as small defects will form when surface roughness is present and the coating will not wet the entire surface. This is also the case when there are inconsistencies in the fibre mats or when rotational speeds increases too much ($\omega > 7000$ rpm). There is an inverse relation between thickness of the coating and the rotation speed [104]. 30 seconds of spinning time seemed to be enough to get rid of the excess of material. In order to help achieving uniform coverage of the entire substrate the process was repeated 3 times.

7000 rpm was selected as speed for the thin base layers in type C coatings to obtain thin layers with consistent thickness. After placement of fibre mats and top coatings there were cases where small air bubbles would be trapped between the fibre mat and the base layer. The PVA and epoxy/amine do not seem to immediately adhere to each other, which might be a point of interest for future research. Assisting the infusion of epoxy/amine in the fibre mat with vacuum did not give desired results.

For samples with the fibre mats it was observed that after applying a droplet of epoxy/amine onto the fibres the appearance of the fibre mat changed from opaque white to transparent, indicating that the epoxy/amine is infusing into the fibre mat and reaching the substrate.

It should also be noted here that it is necessary to use square substrates for spin coating. Any deviation from this caused inconsistent rotation and therefore inconsistent flow of the coating over the substrate, making it impossible to create a uniform layer.

The cerium loaded samples showed a color change during the curing. Figure 5.3 shows several coatings with different compositions. A coating with only epoxy/amine is completely clear, while the addition of an unloaded PVA mat made the coating less transparent. Cerium loaded fibres also show a clear yellow/brownish colour which seems to be more intense when larger quantities of cerium or thicker fibre mats are present.

Crosslinking of the fibres did not seem to have a clear effect on the discoloration of the coating. It seems therefore most likely that the reaction of the cerium and the amine is taking place at the surface of the fibres where cerium has been deposited after solvent evaporation. As the crosslinked

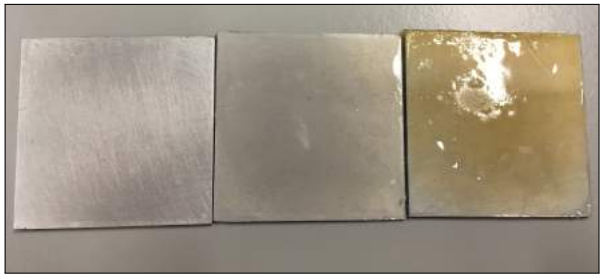

Figure 5.3: *Final manufactured coatings after curing. From left to right no fibres, PVA only fibres and cerium loaded fibres. The cerium loaded fibres give a yellow/brownish colour that seems to be more intense for higher concentrations of cerium.*

fibres should not allow the solvent to penetrate the polymer network as easily as in uncrosslinked fibres, the role of solvent seems to be limited in the reaction process. Fully encapsulating the fibres might protect the inhibitor and coating matrix from these effects.

This behaviour is observed in literature as well, although the exact mechanism is not yet clear [7, 89, 105, 106]. It is known that addition of cerium to a coating can have a negative effect on the barrier properties [107]. There are several mechanisms proposed to be causing the reaction. Kasten et al. relate a shift towards yellow colours to a change in oxidation state of Ce^{3+} to Ce^{4+} [105]. Markley et al. and Mardel et al. however, predict an interaction of the cerium with the polymer matrix. Possibly with glycols to form more carbonyl and amide groups [7, 106]. Cerium is, however, also known as catalyst in curing epoxides and opening of aromatic amines [108, 109].

In order to investigate what is causing the reaction, some pure $CeCl_3$ crystals were added to the separate coatings components, the epoxy, amine hardener, xylene and mixtures of these elements. Figure 5.4 shows these samples. The epoxy is transparent and colourless, the amine has a light yellow hue as does a mixture of epoxy/amine. Addition of cerium to epoxy does not seem to affect either compound. Addition of the cerium chloride to the amine, however, causes a chemical reaction that turns the inhibitor crystal brown in about 15 to 20 minutes. In epoxy/amine mixtures this can also be observed. The addition of xylene speeds up this change in color, likely due to reduction of the viscosity of the solution, thereby improving the mobility of amine groups to react with the cerium. Cerium chloride does not dissolve in xylene, due to the apolar nature of this solvent. It seems therefore, most likely that the cerium is oxidised by the amine, as the effect is very local and only visible on the crystal surface.

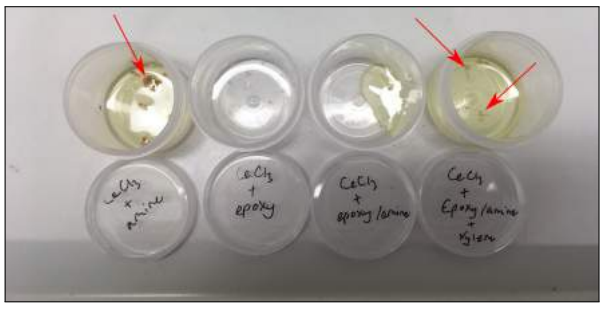

Figure 5.4: *Reactivity between cerium and different coating components. From left to right Ancamine 2500, Epikote 828, Ancamine/Epikote mixture, Ancamine/Epikote/xylene mixture with some added $CeCl_3$ crystals. In the presence of amine-groups the cerium turns brown. Pure amine reacts faster and shows a more intense colour change compared to a mixture of Epikote and Ancamine. When xylene is added, the reaction takes place at a faster rate.*

5.2.2 Passive barrier protection

The fact that the reaction between cerium and amine can be observed means that fibres are not fully encapsulating the inhibitor and that the inhibitor is not shielded from the coating. This means that the inhibitor activity might be affected or that the polymer network of the coating will not fully crosslink, which might affect barrier properties. Passive properties were therefore tested. Figure 5.5 shows the results of the EIS measurements of the coating systems. Passive barrier properties of 10CeB1 are not presented here, as the dataset got corrupted. Based on other EIS data, presented in appendix E.1, it might be suggested that the addition of a highly cerium loaded fibre mat (10CeB2) can have a negative on the barrier properties.

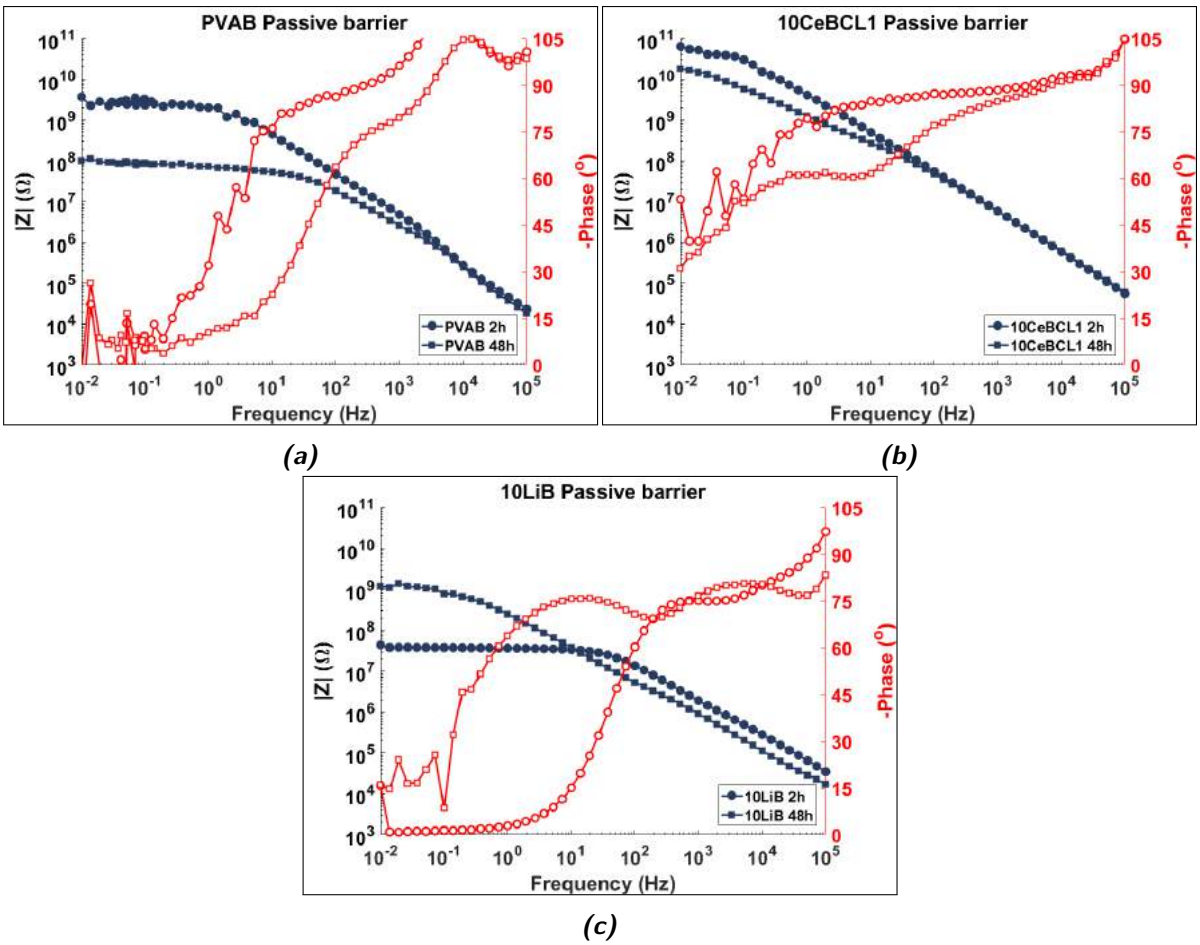

Figure 5.5: *Passive barrier behaviour of several coatings after 2 and 48 hours of immersion in 0.05 M NaCl. 5.5a: Sample with only PVA fibres, 5.5b: Sample with cerium loaded partially crosslinked fibres. 5.5c: Sample with lithium loaded fibres.*

EIS measures, amongst others, the impedance Z of an electrochemical system. Impedance is the frequency dependent resistance of such a system and a higher impedance therefore shows better resistance against corrosion processes. For a perfect resistor the impedance is frequency independent, but other equivalent circuit elements such as capacitors or inductors have a frequency dependent part [110][ch. 4]. Different frequency domains can be related to processes that happen at different time constants. EIS can therefore give insight in several processes in the same plot. For coated metal substrates often three frequency domains are identified. A low frequency range which is related to localised charge transfer processes at the substrate such as pitting, a medium frequency range related to oxide layers or other interfaces between the substrate and films on top, and the high frequencies which hold information about the electrolyte and pore resistance and barrier properties [107].

A perfect coating has a purely capacitative response, meaning that no charge can pass the electrode. This shows as a straight line with slope -1 in the impedance plot [110][ch.16]. The corresponding phase angle of a capacitor is -90° [110][ch.4]. Unfortunately, all coatings show that the straight line is deflecting towards a horizontal line, indicating that none of the system are purely capacitative which could be due to the introduction of the fibre mat. This might indicate water absorption and some porosity in the coating, even at short immersion times. Still, all coatings show decent barrier properties.

The PVAB coating shows a significant drop in low frequency impedance over time, likely due to water absorption, but the impedance values are still high ($10^8\Omega$). This indicates that the coating forms a decent protection for the substrate against the corrosion environment.

Using a lithium based inhibitor in the 10LiB coating shows an increased impedance after 48 hours compared to 2 hours of immersion, where all other coatings show a decrease. This is an indication of release of corrosion inhibitor and active corrosion protection of the undamaged coating. Next to the increase in barrier properties, this does mean that initial porosities in the coating formed pathways for electrolyte diffusion into the coating and inhibitor release.

The 10CeCL1 with partially crosslinked fibres performs the best. This coating is quite stable over time and shows the highest impedance in general. The behaviour is also the closest to pure capacitative behaviour, which shows in the high phase angle close to -90° over a broad frequency range.

5.2.3 Active corrosion protection

Next, the active corrosion protection of the coatings was analysed by immersing the artificially damaged coatings in corrosive aqueous environment for up to 4 weeks. More EIS results can be found in appendix E.2.

5.2.3.1 Open circuit potential

Following the open circuit potential (OCP) gives a first indication of the stability of the system and how well it is protected against corrosion. The OCP of AA2024-T3 in NaCl environment against Ag/AgCl is in the order of -0.5 to -0.55 V [76, 77]. As the OCP of aluminium alloys with low copper and magnesium content and pure aluminium are in the order of -0.7 to -0.75 V [111, 112] and -0.9 V [113] respectively, decreasing OCP is an indication of the decomposition of the alloy [77, 114, 115]..

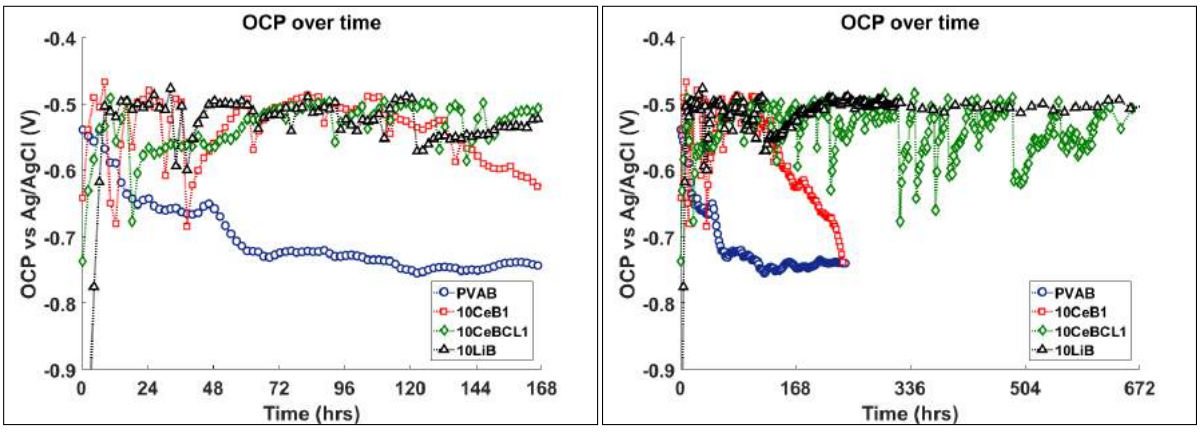

(a) *(b)*

Figure 5.6: *Evolution of OCP over time for different samples over the course of 5.6a: 1 week and 5.6b: 4 weeks.*

Figure 5.6 displays the OCP evolution over time. It is clear that the PVAB sample shows a continuous declining OCP over time towards values that indicate dealloying of the surface. Inhibitor loaded

samples show OCP values that indicate protection of the surface, as they remain in the -0.5 to -0.55 V range.

It is observed, however, that the stability of the measurements is different for different inhibitors. The cerium loaded samples show significant instabilities in the first 20 hours (10CeBCL1) and 65 hours (10CeB1). After this initial period, the OCP becomes more stable up to about 110 hours when the 10CeB1 starts to show a decline in OCP, indicating coating failure. After 130 hours the 10CeBCL1 sample starts to show more instabilities again which last up to 4 weeks of immersion. These instabilities are, however, recovered every time, indicating that several pitting or other corrosion damages occur, followed by self-healing protection of the cerium inhibitor, which will deposit on cathodic sites.

The OCP of the 10LiB on the other hand has initially a very low at -0.9 V. The OCP rises in about 10 hours to -0.5 V. After 120 hours of somewhat unstable behaviour the OCP is increasing and remains stable up to at least four weeks. This is an indication that during the first 120 hours of immersion a very stable film is forming on the substrate, which surpresses any corrosion processes and pitting.

5.2.3.2 EIS

Further information was obtained by the impedance measurements presented in figure 5.7. PVAB (fig. 5.7a) and 10CeB1 (fig. 5.7b) are shown up to 10 days of immersion. The best performing samples, 10CeBCL1 (fig. 5.7c) and 10LiB (fig. 5.7d) are shown up to 4 weeks of immersion.

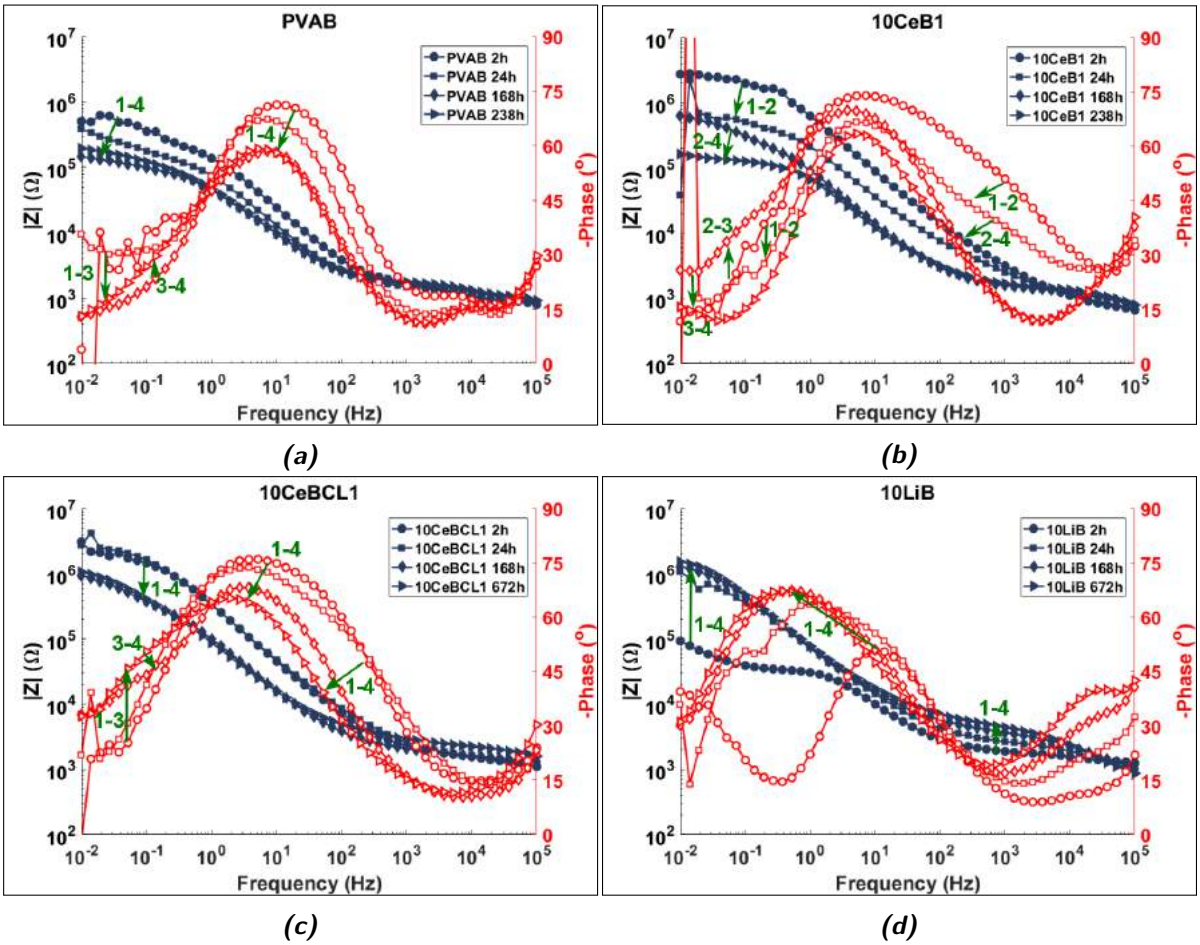

Figure 5.7: *EIS results of different coating up to 4 weeks of immersion.*

The PVAB sample (fig. 5.7a) shows a lower impedance value than the other samples over the course of the entire experiment. Over the full immersion time, impedance and phase are decreasing

over the entire frequency range, indicating water absorption, while no active corrosion protection is taking place. The substrate is therefore not very well protected.

All inhibitor loaded samples show signs of active corrosion protection. The cerium loaded samples both show a decrease in phase in the medium/high frequency range, which can be related to water absorption in the coating and the increase of diffusion paths for electrolyte through the coating. Both coatings also show an increase in the phase angle in low frequency range where a second time constant is visible. This is an indication of the growth of a protective barrier layer on the substrate caused by the cerium depositing on cathodic sites, which suppresses activity at the substrate. The 10CeB1 fails between 168 hours and 238 hours of immersion, as the phase angle drops in the entire frequency range during this time. This is also visible in a decrease of impedance. The 10CeBCL1 sample on the other hand remains highly stable in both impedance and phase from 1 week onto at least 4 weeks of immersion, indicating good protection. The partial crosslinking of the fibres, might therefore be beneficial for obtaining corrosion protective properties.

The lithium loaded sample 10LiB (fig. 5.7d) shows continuous increasing impedance and phase angle over the entire frequency range for immersion times up to at least 4 weeks. The initial impedance value is very low, caused by the relatively wide scratch, but the coating is quickly recovering this low impedance and the high stability indicates the formation of a very stable protective film on the substrate. The three time constants in the phase after 2 hours of immersion can be related to dissolution of inhibitor in the solution, the native aluminium oxide layer and activity at the substrate, for high, medium and low frequencies respectively.

As modeling and fitting the EIS data is difficult, due to the complex composition of the coating it was decided to follow the development of low frequency over time in order to say more about the protective potential of the different coatings. Impedance at low frequency, 0.01 Hz in this case, is an indication of the activity of the substrate and the extent to which it is protected [107]. The low frequency impedance is shown in figure 5.8.

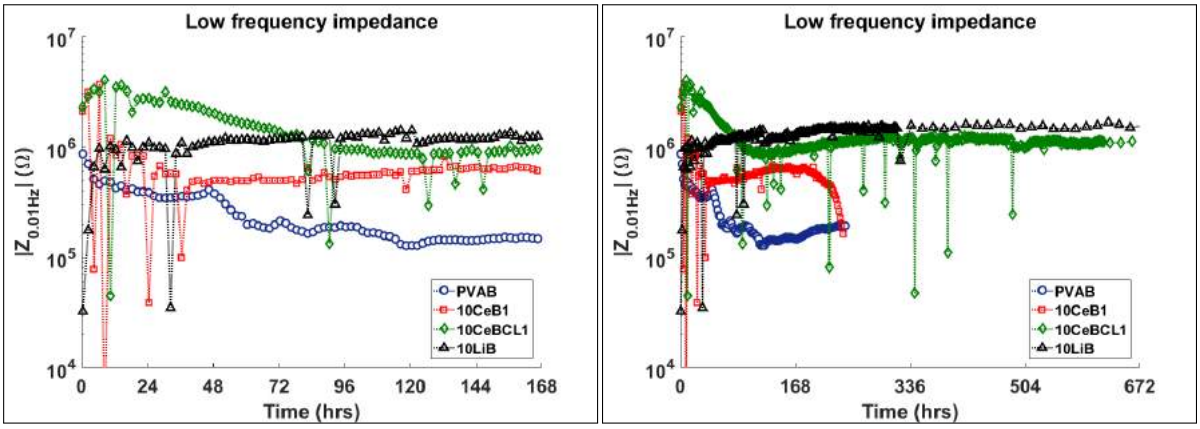

Figure 5.8: *Impedance at low frequency over time. The value of low frequency impedance is an indication of the protection of the surface. 5.8a: Impedance over 1 week. 5.8b: Impedance over 4 weeks.*

The PVAB sample shows an immediate decrease in impedance which stabilises between 24 and 48 hours, which might be caused by corrosion products blocking the scratch. Subsequently the impedance drops even further, until after 120 hours it remains relatively stable. The impedance value is well below the other samples, indicating less protection compared to the other samples. The difference between the best protected system and the PVAB sample is almost a full decade over the entire time span of the experiment.

All inhibitor loaded samples show an initial increase in impedance in the first 10 to 15 hours, due

to the release of corrosion inhibitor, followed by a high impedance plateau during the first week of immersion. After 180 hours, the 10CeB1 coating starts to fail, which was also observed in the EIS plots. 10CeBCL1 and 10LiB samples keep a relative stable and high impedance for up to 4 weeks of immersion, where the lithium loaded sample even shows slowly increasing impedance, again indicating that crosslinking is beneficial for long term stability and Li_2CO_3 has very good corrosion protective properties.

Also in this plot a difference can be observed in the protective mechanism of cerium versus lithium. The same type of difference in instabilities between the 10LiB sample and 10CeB1 and 10CeBCL1 can be observed as in the OCP evolution in figure 5.6. This indicates that the lithium is able to form a stable protective film on top of the substrate, while cerium loaded samples repair multiple damages by repassivation of the surface after initiation. This is in agreement with the fact that cerium acts as cathodic inhibitor in need of initiation of dealloying to form insoluble cerium oxides and hydroxides [77].

5.2.3.3 Optical results

The images recorded in the opto-EIS provide extra information in the mechanisms playing a role during the immersion tests. Figure 5.9 shows what the scratched samples looked like after 0, 2, 24, 1 week and, if available, 4 weeks of immersion. More examples can be found in appendix E.4.

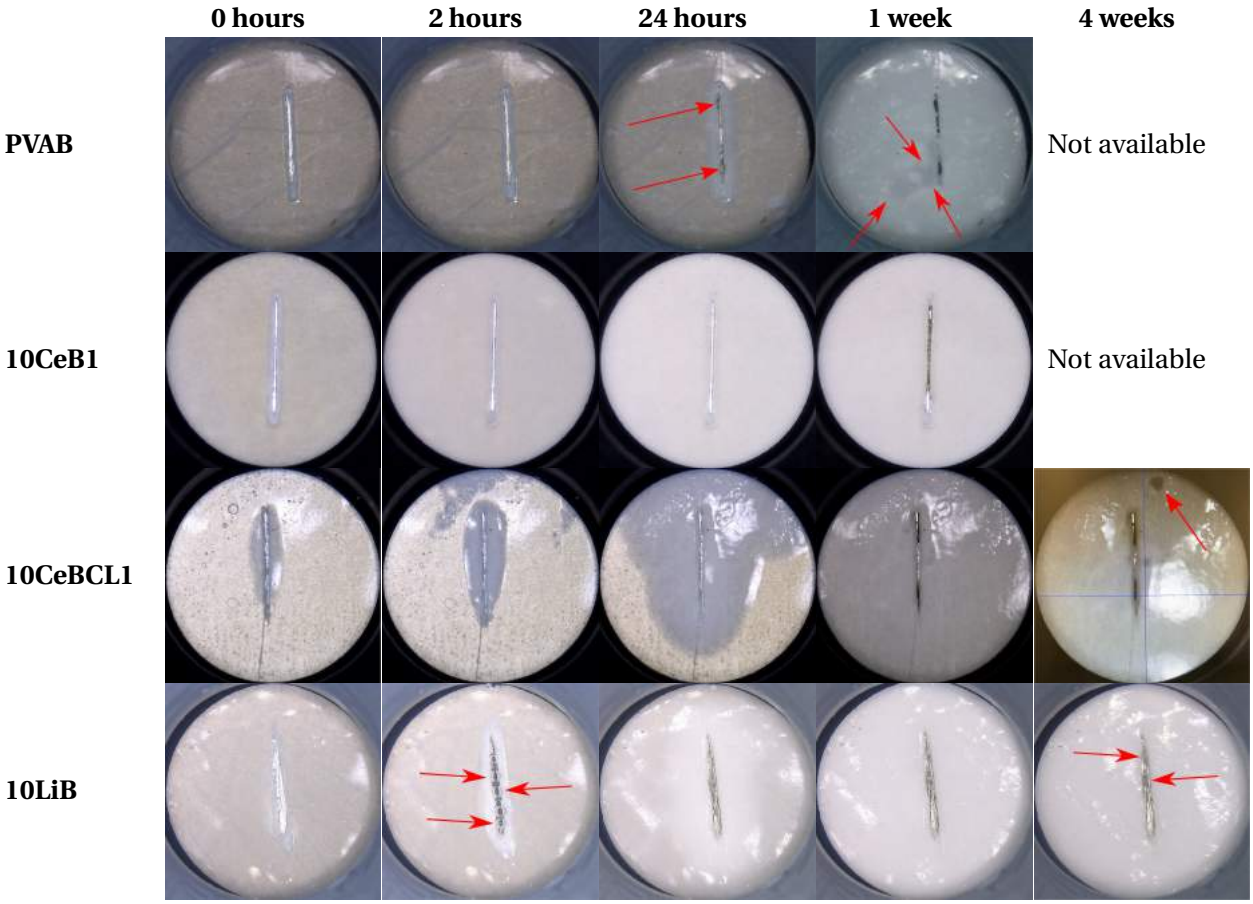

Figure 5.9: *Different samples during the electrochemical tests. From 0 hours to 4 weeks of immersion.*

The PVAB sample has a very active scratch that shows clear signs of corrosion products forming

during the first 24 hours, indicated by the arrows. This process is ongoing and oxides are filling the scratch blocking some of the diffusional pathways of aggressive species to enter. After 1 week hours we observe that the scratch is almost completely filled with black and brown corrosion products. Next to that, a large delamination is visible, growing from the bottom of the scratch. This is a clear sign of a failed coating and corresponds to the low impedance values and reducing OCP of the PVAB sample.

Cerium loaded samples all show signs of protection as large scale growth of corrosion products is slowed down and partly prevented, leaving bright spots in the scratch. In all samples water ingress can be observed, dissolving or swelling the fibres thereby releasing inhibitor. Despite of having a partially crosslinked fibre mat, 10CeBCL1 still shows a fast ingress of water, also caused by defects in the top layer. The corrosion products that have formed after 1 week of immersion seem to be relatively stable over time. Some new corrosion products that have formed seem contained, confirming that the cerium is able to repassivate active sites. No large delaminations can be observed after 4 weeks indicating that partially crosslinking might help improve the coating integrity.

The 10LiB sample shows ingress of water in the first 24 hours of immersion. Next to that, bubbles are observed on the scratched surface after 2 hours of immersion, indicating high activity in the scratch. Over the course of four weeks the scratch stays shiny in most places showing clear protection of the surface. After four weeks, two dark grey spots of corrosion product can be observed in the top of the scratch. They are very stable and seem to form a good protective barrier.

It should be noted that after removal of the coating from the electrolyte, all coatings showed delamination of the top coat. This includes type B coatings (see app. E), where this means full delamination. Partially crosslinked fibres reduced this effect, but could not fully eliminate it. Next to this, all cerium loaded samples lost the brown/yellow color in the exposed area. This is an indication that the color change is caused by oxidation of the cerium. The activity of the cerium seems to be good enough to protect the substrate. It is, however, still possible that the reaction prevents part of the amine-groups to crosslink in the epoxy/amine network, leading to worse barrier properties.

5.2.4 Post mortem characterisation

Finally, the samples were investigated by SEM and EDS in order to try and understand the structure of the formed oxides. Only PVAB and 10CeBCL1 are shown here. More SEM/EDS data can be found in appendix F. Figures 5.10a and 5.10b show the PVAB sample scratch after the immersion test. It is clear that the scratch is filled up with oxides and almost no aluminium surface can be seen underneath, showing the lack of protection. The structure of the oxides is well known to be aluminium oxides and hydroxides [16]. EDS results (app. E), confirmed that the main elements of these structure are aluminium, oxygen and chlorine, indicating that chloride ions have ingressed in these oxide layers as well. This will speed up the corrosion processes.

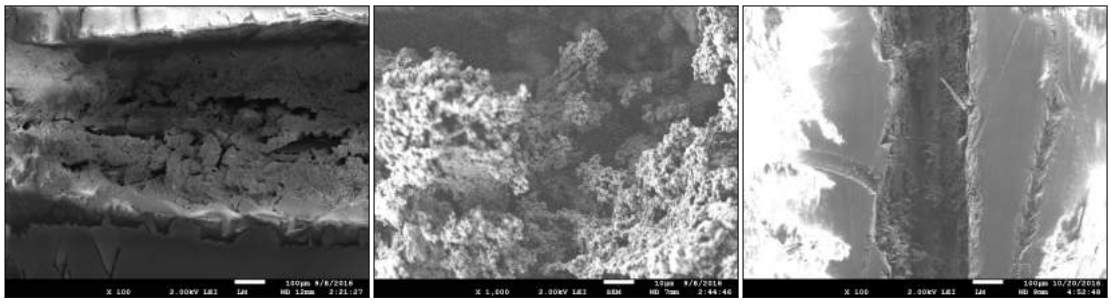

(a) *(b)* *(c)*

Figure 5.10: *SEM images of scratched coatings after exposure to aqueous corrosive environment. 5.10a and 5.10b: Sample with only PVA fibres. The scratch is almost completeley filled with aluminium corrosion products 5.10c: 10CeCLB1 sample with $CeCl_3$ and partly crosslinked fibres shows a relatively clean scratch, where the aluminium substrate can still be observed.*

The 10CeCLB1 coating, shown in figure 5.10c, shows, next to the aluminium corrosion products, parts of the scratch that seem relatively 'clean'. This corresponds to the pictures after 1 and 4 weeks of immersion, showing only local black areas of corrosion products. These corrosion products still have a typical aluminium oxide structure and indeed aluminium, oxygen and chlorides are present in these structures. At the 'clean' locations cerium can be detected amongst several alloying elements of aluminium 2024-T3, such as copper, zinc and manganese. This confirms that cerium was released from the fibres such that a protective layer has formed based on cerium oxides or hydroxides [116, 117]. This is a clear indication of the protective capabilities of the cerium loaded system. The fact that other corrosion products are still present might be due to the fact that cerium is a cathodic inhibitor, mainly depositing on cathodic zones, leaving the possibility for anodic areas to still show corrosion [16].

For several samples Raman spectroscopy was used in order to locate both cerium rich [102] and copper-rich phases [103] by the peaks shown in the Raman spectra in figure 5.11 . By mapping a part of the scratch that was protected, the presence of the elements could be located with high accuracy. This gives more insight in the protecting mechanism of the cerium. From 5.12 it can be seen that cerium and copper are abundantly present in the scratched area. Next to this, the cerium seems to be deposited in areas that are rich in copper. This implies that cerium deposits on copper-rich intermetallic phases, therefore preventing large scale pitting and degradation of the substrate. This confirms the previous observations.

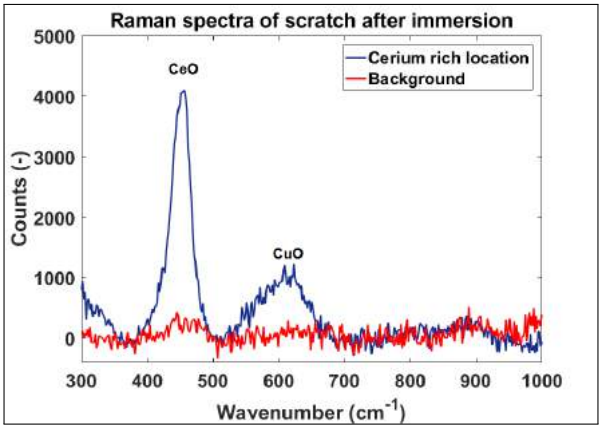

Figure 5.11: *Raman spectra with investigated peaks.*

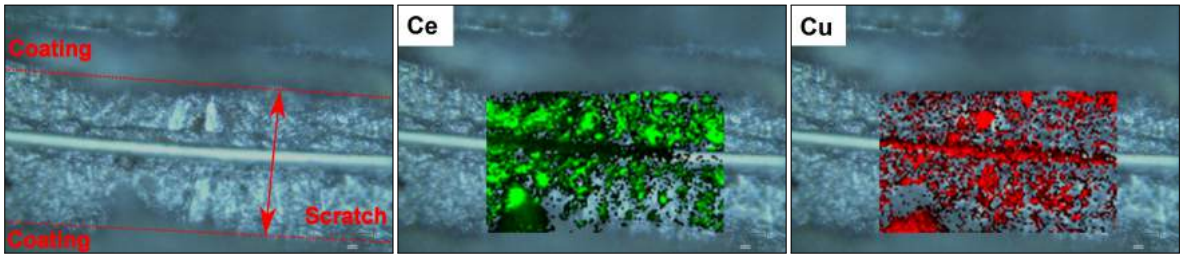

(a) ***(b)*** ***(c)***

Figure 5.12: *Part of 10CeB2 sample after immersion. 5.12a:Original image before mapping. 5.12b: Bright green areas highlight presence of cerium oxides. 5.12c: Bright red areas highlight presence of copper-rich phases.*

5.3 Conclusions

In this chapter it is shown that electrospun fibre mats loaded with $CeCl_3$ or Li_2CO_3 can successfully be applied in an epoxy/amine coating system with corrosion protective properties. Long term corrosion protection up to four weeks was obtained without any large scale delaminations taking place as confirmed by an opto-EIS characterisation or corrosion protective properties.

The creation of a good protective coating is not straight forward, as cerium based corrosion inhibitors will react with the amine in the epoxy/amine matrix. This has a negative effect on the barrier properties of the coating. The addition of the fibre layer in general can introduce a decrease in barrier properties, possibly due to limited adhesion between fibre mats and the epoxy/amine. The manufacturing of such a complicated coating system, should, therefore, be carried out in a precise manner and allows for improvement.

Dissolution of the fibres releases inhibitor but introduces delaminations. For type B coatings this means full delamination of the top coat. Adding a base layer to the coating does help with preventing full exposure of the substrate, but still allows for delamination of the top coat. By crosslinking the fibres, this effect is reduced and the integrity of the coating is increased aiding long term protection of the substrate up to 4 weeks.

$CeCl_3$ is succesful in suppressing large scale corrosion on the aluminium. The self-healing mechanism of cerium is based on the repassivation of active copper-rich cathodic sites. The formation of protective films was observed by opto-EIS and Raman. OCP and low frequency impedance show fluctuations, suggesting multiple healing events where the inhibitor is able to restore its protective ability.

Li_2CO_3 showed a very high potential to protect wide scratches for a long time. The protective mechanism is different from the cerium, as it seems that a stable protective film is formed quickly after immersion. The lithium therefore does not show multiple healing events, but very stable behaviour over time.

Overall, the proof of concept is successful and active corrosion protection can be achieved by creating coating systems with inhibitor loaded nanofibre mats. Corrosion protection is increased by a factor 5 to 6 compared to non-protected systems. There is, however, still room for improvements.

Chapter 6

Conclusions, recommendations and future prospects

In this chapter, the conclusions of research project will be drawn and the main research question will be answered. Next to that, some recommendations for improving several aspects in this work and future research will be done.

6.1 Conclusions

Chapter 3 elaborated on the electrospinning of inhibitor loaded electrospun nanofibres. A self-developed electrospinning set-up was built and succesfully used. It was possible to create electrospun PVA nanofibres loaded with inorganic ($CeCl_3$, Li_2CO_3) and organic/inorganic ($Ce(dbp)_3$) corrosion inbibitors. Many parameters, of both processing and polymer solutions, have been investigated on how they influence the electrospinning process. The presence of inhibitor salts inside the solution has a large influence on the conductivity of the solvent, reducing the stability of the process, limiting the applied potential and feed rate, slowing the process down. A practical maximum loading of around 10 wt% inhibitor with respect to the polymer matrix was found to give consistent results. The effect of inhibitor concentration seems to have a larger effect on the process than changing other solution parameters like surface tension or solvent volatility. Solubility of the inhibitor will largely determine if the inhibitor will be present in the final fibre mat as particles between the fibres, or fully mixed in the polymer network. Finally, ambient conditions, especially relative humidity, have a large influence on the quality of the fibre mat and control over these conditions is necessary to obtain reproducible results.

Effort was put in to characterise the release of the $CeCl_3$ from the loaded fibre mats. In chapter 4 it was shown by EDS that cerium is uniformly dispersed through the fibre mat. The release of cerium from a dissolving polymeric matrix can be followed in-situ by UV/VIS, by deconstructing the absorbance spectra of a combined cerium/PVA system. This method was validated by ICP. The influence of inhibitor loading on release kinetics was investigated. Difference in inhibitor loading will change the final concentration levels and speed at which the concentration changes, but not the release mechanism. In order to achieve slower, sustained release and reinforced coatings, crosslinking of the PVA fibres might be useful. Different levels of crosslinking were achieved by crosslinking inhibitor loaded fibre mats in a crosslinking solution of acetone with 10 mM or 30 mM GA. The influence of crosslinking on the release kinetics was also analysed. The effect of increasing crosslinking is a reduction in inhibitor release. Partially crosslinked fibres show an initial burst release, likely caused due to their cracked surface. Heavily crosslinked fibres show a slower and lower release, likely due to trapping of cerium in the polymer network. The release curves were fitted with an expanded Peppas-Korsmeyer

model, which includes relaxation phenomena of polymers, caused by swelling. Non-crosslinked fibres have a anomalous release exponent, indicating that swelling plays a role in speeding up initial release stage. Higher crosslinking density reduces the influence of swelling and shows more Fickian release. The kinetic constants are decreased with increasing crosslinking, indicating slower release.

Chapter 5 showed successful manufacturing of coating systems with $CeCl_3$ and Li_2CO_3 loaded PVA fibre mats and epoxy/amine matrix. The creation of a good protective coating is not straight forward, as cerium based corrosion inhibitors will react with the amine in the epoxy/amine matrix. This has a negative effect on the barrier properties of the coating. The addition of the fibre layer in general can introduce a decrease in barrier properties, possibly due to limited adhesion between fibre mats and the epoxy/amine. Dissolution of the fibres releases inhibitor, but introduces delaminations of the top coat. Adding a base layer to the coating does help with preventing full exposure of the substrate, but still allows for delamination of the top coat. By crosslinking the fibres, this effect is reduced and the integrity of the coating is increased aiding long term protection of the substrate up to 4 weeks. $CeCl_3$ is succesful in suppressing large scale corrosion on the aluminium. The self-healing mechanism of cerium is based on the repassivation of active copper-rich cathodic sites. The formation of protective films was observed by opto-EIS and Raman. OCP and low frequency impedance show fluctuations, suggesting multiple healing events where the inhibitor is able to restore its protective ability. Li_2CO_3 showed a very high potential to protect wide scratches for a long time. The protective mechanism is different from the cerium, as it seems that a stable protective film is formed quickly after immersion. The lithium therefore does not show multiple healing events, but very stable behaviour over time. The best performing coatings increased corrosion protection by a factor 5 to 6 compared to non-protected systems.

The research question *"Can the use of inhibitor loaded nanofibres lead to highly efficient anti-corrosion coating systems?"*, can therefore be answered in a positive way. Be it with challenges, it possible to create inhibitor loaded fibres and apply them in a coating system that will show long-term corrosion protection of up to 4 weeks, which is 5 to 6 times more than unprotected systems. Moreover, it is possible to change certain parameters in the fibre chemistry or coating composition to obtain desired behaviour. This work, therefore, opens many doors to exploit this knowledge in obtaining more sophisticated coatings that will show even better performance.

6.2 Recommendations

Although this work was successful in achieving its goal. There are many things that could be improved in future research. This section will present some of the recommendations based on the experiences in this research.

6.2.1 Electrospinning set-up

The electrospinning set-up can be modified to improve the reproducibility and large production. First, The box could be made more airtight, or placed in a room with more climate control on the outside. This will make it easier to control the conditions in the box.

Secondly, the fibre mats were collected on a stationary plate. This means that there is a circular deposition area with a distribution of fibre mat thickness. The centre will be the thickest, the sides will be thinner. This reduces the usable part of the fibre mat, as one would like to have a uniform distribution in thickness over the entire area. This could be solved by adding a target that moves laterally with respect to the needle. This will make the fibres deposit more uniformly over the sample and makes it possible to create bigger, uniform fibre mats. Downside of this system is that it will take a longer time to reach the desired thickness over the entire deposition area. One can also think about

a rotational drum collector. This will both increase the area of deposition and increase the amount of useful material, as well as give control over fibre alignment. Fast rotation will induce fibre alignment which can be interesting to investigate.

6.2.2 Release kinetics measurements

There are a few recommendations related to the release kinetics measurements. There could be an improvement of the set-up by being able to pump the solution through the UV/VIS spectrometer during measurement. This would allow the fibre mats to be placed in solution outside of the cuvet which prevents them to be folded. A flat fibre mat will likely show a different behaviour in release. The downside would be, however, that more solution needs to be used causing lower concentrations which are harder to measure.

When changing the matrix of the fibres, the correction method should be checked again. If the new matrix has a different absorbance spectrum than PVA, the prediction method of the absorbance spectrum should be evaluated and changed in order to match the new material. A new ICP validation is also necessary, to ensure the modified method will work.

Lastly, as release kinetics are sometimes hard to understand, some time could be invested in trying to model the processes that are going on. There will be swelling, erosion and dissolution of matrix, next to diffusion of the inhibitor. Modeling might give more insight in how these processes are linked together and if experimental measurements can be matched with the simulation results.

6.2.3 Coating systems

Finally, some recommendations can be given in relation to the coating systems.

First of all, the interactions of cerium with the epoxy/amine matrix seem to be negative for the barrier properties of the coating. It would therefore be better to shield the fibres further from the matrix. This could be done by adding a shell around the loaded PVA fibres as described in chapter 2 via biaxial electrospinning. This also requires a modification of the electrospinning set-up by adding a biaxial needle.

An extra benefit of this could be that the shell material can be picked in order to have good interactions with the epoxy/amine matrix. This would ensure better cohesion between the different layers of the coating, which might reduce the water ingress and thereby improve barrier properties further.

From this work it seems that lithium based inhibitors are very interesting to investigate further. Downside is that lithium is not detectable in UV/VIS making it more difficult to follow in-situ release of the fibres. ICP can detect lithium, but will not allow for in-situ measurements.

It was shown that crosslinking reduces the release, but swelling allowed more and faster release. A material that swells under the right conditions such as a change in pH might promote release only at desired conditions and stop the release when the corrosion process has been under control.

One can also think of combinations of fibres with different functionalities. Some fibres that contain corrosion inhibitors, some fibres that have surface modifying agents to form hydrophobic layers or fibres that can act as traps for aggressive species. This would create a truly multifunctional coating which would likely have a better performance.

Finally, in terms of coating production it would be better if the fibres were directly spun onto the substrate instead of manually added, as this will yield better adhesion between different layers and prevent defects such as air entrapment. When adding the base layer the surface of the sample becomes non conductive, which will repel the fibres during spinning. When adding the sample to a larger collector plate and moving this plate back and forth through the cone of fibres it is possible to collect fibres on this surface. Extra benefit of this method is that it is easier to create a fibre mat with uniform thickness over the entire surface of the substrate.

Appendices

Appendix A

Challenges and considerations in electrospinning inhibitor loaded fibres

This appendix elaborates on several challenges and things to take into account when electrospinning inhibitor loaded fibres and can be used together with the general comments in chapter 3.

A.1 Challenges during electrospinning

Even though the electrospinning process seems quite easy, starting a new project with electrospinning can be quite challenging. The process of finding the right spinning conditions can be quite lengthy and tedious, especially since it needs to be redone every time a parameter in the solution itself changes. There are a lot of variables that can influence the process, many of which are coupled with competing mechanisms, and thus it takes some time to find an optimum for the parameters.

Figure A.1 shows some typical fibre structures one can encounter during initial electrospinning and optimising of the spinning parameters. During the start of the project the equipment was limited to 10 kV potentials. Due to the limited power available, the effective electrospinning window is decreased limiting the options. A smaller amount of concentrations can successfully be spun into fibres.

The range of spinning distances is quite limited as well. Below 8 cm more bead formation is present, because of a lack of flight time of the fibre. This limits the amount of stretching and subsequent bead removal. An additional effect is that the solvent starts to collect in the fibre mat. When the droplets start to flow they dissolve part of the fibres, destroying the sample (fig. A.1a). Due to the relatively low potentials, 10 cm seems to be about the maximum distance that can be used.

The right combination of parameters, a concentration of 6 wt% to 8 wt%, a distance of 10 cm and a voltage of 9 or 10 kV did however create nicely uniform fibres (see fig. A.1b).

Figure A.2 shows some images of unloaded and loaded 6 wt% PVA fibres produced at sub-10kV potentials. It is clear that loaded fibres are a lot thinner than pure PVA fibres (A.2a) spun at the same PVA concentration. The diameter of the fibres is reduced from 200 nm to around 100 nm. This effect is due to the increased conductivity of the solution. This increases the electrostatic forces on the fibre and induces more stretching of the fibre resulting in smaller diameter fibres. To counter this reduction in fibre diameter the polymer concentration was increased to 8 wt%. Additional effect is the increased stability of the process, caused by an increase in viscosity. This increase of polymer concentration by 2 wt% after introduction of the corrosion inhibitors turned out to be a useful rule of thumb when spinning of other materials was attempted.

It should be noted that there is not simply one set of parameters that is 'the right one'. Various combinations of settings are possible to achieve acceptable results. The parameters reported in this thesis, are therefore simply the ones that were selected for this work, but slight variations might also

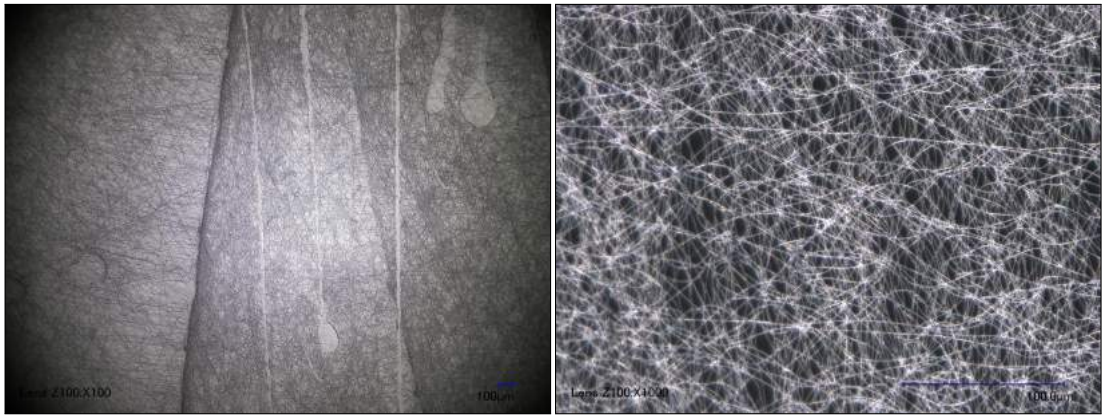

(a) ***(b)***

Figure A.1: *Fibres spun with different parameters, showing some of the typical good and bad fibre structures that can be found when optimising the electrospinning parameters. 3.4b: PVA fibres spun at 15 wt%, 6.5 kV and 3 cm. These fibres are an overall mess. Very uneven fibres, droplets of solvent and polymer are all clearly visible. A.1a: PVA fibres spun at 5 wt%, 6 kV and 5 cm. One can clearly see the 'tears', formed by aggregations of solvent, that dissolve the fibres again. Increasing the spinning distance resulted in beaded fibres. A.1b: Fibres spun at 6 wt%, 7 kV and 5 cm. These fibres have good quality and are uniformly distributed.*

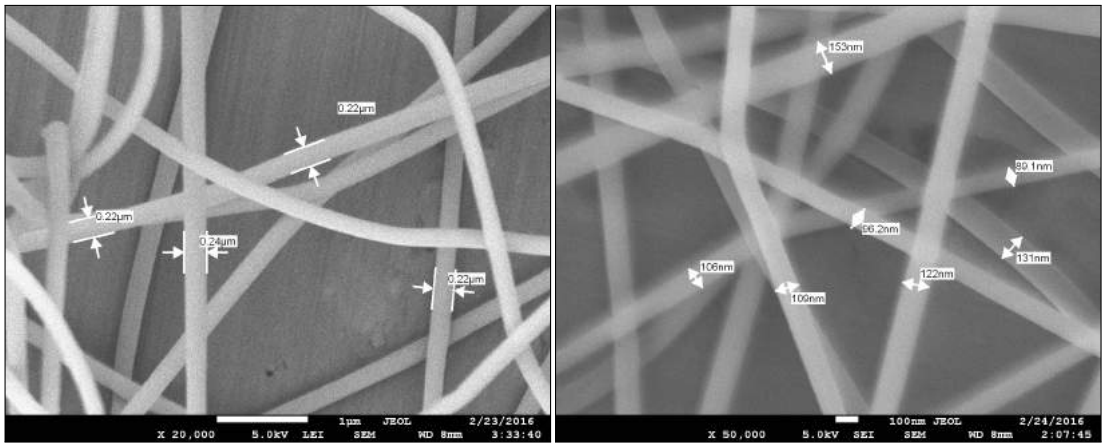

(a) ***(b)***

Figure A.2: *6 wt% PVA fibres loaded with different levels of corrosion inhibitor $CeCl_3$. A.2a: Fibres spun with a 6 wt% solution at 9 kV and with a distance of 10 cm. The fibres are of good quality and have a thickness in the order of 200 nm. A.2b: PVA fibres loaded with 10 wt% $CeCl_3$.*

be useful.

A.2 Tips and ideas

When loading electrospun fibres with corrosion inhibitor salts the instabilities increase. This might produce thinner fibres, as the fibres encouter stronger electrostatic stretching forces. To counter this effect the polymer concentration can be increased. Initially the spinning conditions for spinning PVA were selected to be for 6 wt% solutions which gave nice results. After introducing the inhibitor, the concentration was increased to 8 wt% in order to cancel the instabilities and thinning of the fibres. This approach worked well for several other solution mixtures and can be used as rule of thumb. If a certain polymer concentration works well without inhibitors, increasing the concentration by 2 wt% will work well after inhibitors are added.

In order to quickly decrease the relative humidity in the box, a heating gun was placed in the electrospinning box. Prior to electrospinning the temperature in the box was increased to about $30^{/circ}$C. This would allow the air to take up more moisture and reduce the relative humidity. By letting the warm air flow out of the box during setting up prior to electrospinning. The moist air flows out of the box. This allows for quick reduction of relative humidity.

Appendix B

Crosslinking PVA

Several approaches to crosslink PVA were attempted as mentioned in chapter 4. This appendix shows some information about the abandonded routes of crosslinking with PAA and GA.

B.1 Crosslinking PVA and PAA

B.1.1 Methods

Both PVA and PAA can be mixed in solution and a subsequent thermal treatment will initiate crosslinking [83]. The mixed solution can be spun into fibres and afterwards a thermal treatment can be applied [84, 85]. Polymer solutions were mixed in molar ratios of reactive groups, (-OH) for PVA and (-COOH) for PAA, of (1:0.25) and (1:0.5) in DI water. The total polymer weight fraction was 12 wt%. Corrosion inhibitor was added as 10 wt% of the polymer fraction. After electrospinning the fibre mats different heat treatments were used to obtain several amounts of crosslinking.

Table B.1: *Tested heat treatments for crosslinking PVA and PAA.*

Molar ratio (PVA:PAA)	Temperature (°C)	Time (mins)
1:0.25	100	5, 15, 30
	140	5, 15, 30, 60, 120
	180	5, 15, 30, 60 ,120
1:0.50	140	5, 15, 30
	180	5, 15, 30

To check if crosslinking was successful, the fibres were suspended in DI water after the thermal treatment. Subsequently, the release of cerium chloride was tested as described in chapter 4.

B.1.2 Results

Almost all samples that were crosslinked in molar ratio (PVA:PAA) of (1:0.25) immediately dissolved, indicating crosslinking was not successful. Only at very long heat treatment of 120 minutes at 140°C, or >30 minutes at 180°C. The fibres remained intact. At these treatments the fibre mats were starting to turn yellow.

Molar ratios of (PVA:PAA) of (1:0.50) were more successful. Heat treatments of 15 and 30 minutes at 140°C showed no full dissolution with increasing water resistance for longer times. High temperature caused the fibre mats to turn brown or yellow. A heat treatment of 140°C for 30 minutes was selected as desired crosslinking method.

Figure B.1 shows the release of $CeCl_3$ from PAA crosslinked fibres with . As can be seen, the release

fraction is extremely low at 2.5 %. Next to that, the measurement is quite noisy. These types of results were observed for all types of fibres with PAA. Even the ones that were not heat treated and therefore not crosslinked. As it turns out, from literature, the carboxylic acid groups of PAA are able to form complexes with cerium ions, preventing their release in solution. PAA is in fact so effective in binding cerium that it is used to filter cerium ions from solution [118]. This is obviously not what the project is aiming for and was the main reason to abandon this route.

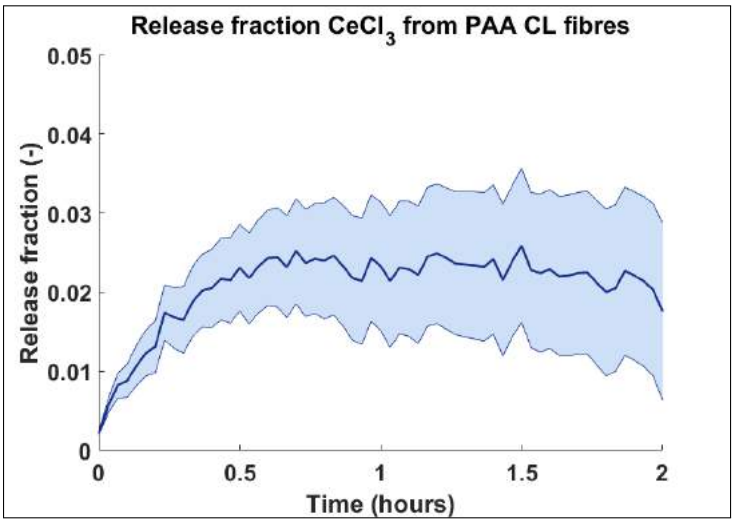

Figure B.1: *Release fraction of $CeCl_3$ over time from PVA fibres crosslinked with 0.5 mol PAA and heat treated at 140° for 15 minutes.*

B.2 In-situ crosslinking of PVA and GA

B.2.1 Methods

For in-situ crosslinking GA was mixed with 37% HCl in volume ratio GA:HCl of 10:1. This solution was added to a 7 wt% PVA solution with 10 wt% inhibitor under rapid stirring in order to obtain a 90:1 mole ratio of PVA:GA. After mixture the solution was electrospun directly under the same conditions as described in chapter 4.

B.2.2 Results

Electrospinning of the in-situ crosslinking solution was possible, but as described by Tang et al., due to the fact that the solution is crosslinking during the electrospinning process, the viscosity changes over time. The solution prepared in this study, was spinnable for about 15 to 20 minutes. After that, the solution became too viscous to be spun, even at different electrospinning settings. The fibre spinning could therefore not be maintained for the desired, longer times.

Next to that, the fibre morphology will change during the electrospinning window, making it hard to predict what the fibres look like in different layers of the fibre mat. It is therefore also hard to predict how this will affect the release behaviour of the fibre mat.

A final problem is that after the solution starts crosslinking, the entire solution in the bulk and in the syringe is crosslinking too. This makes every batch useless after a few hours and creates a lot of extra waste material. The in-situ crosslinking was therefore abandoned.

Appendix C

EDS spectra of $CeCl_3$ loaded fibres

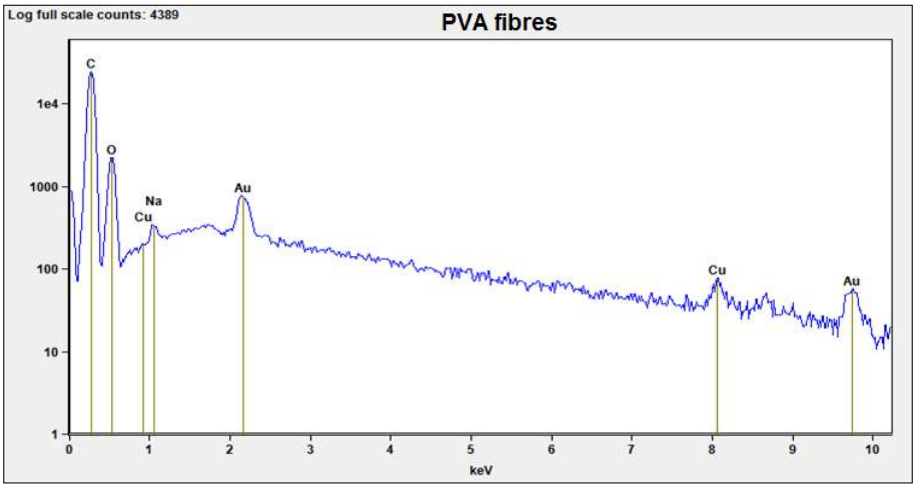

Figure C.1: *EDS spectrum of pure PVA fibres.*

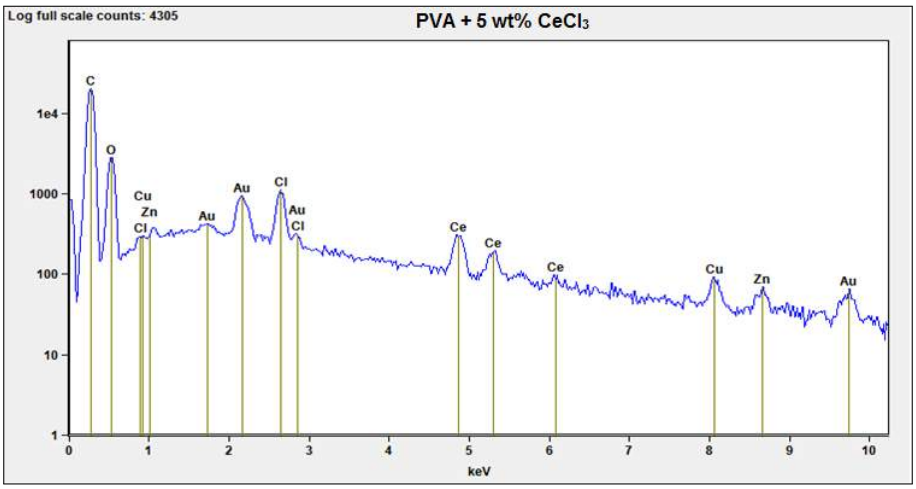

Figure C.2: *EDS spectrum of PVA fibres loaded with 5 wt% $CeCl_3$.*

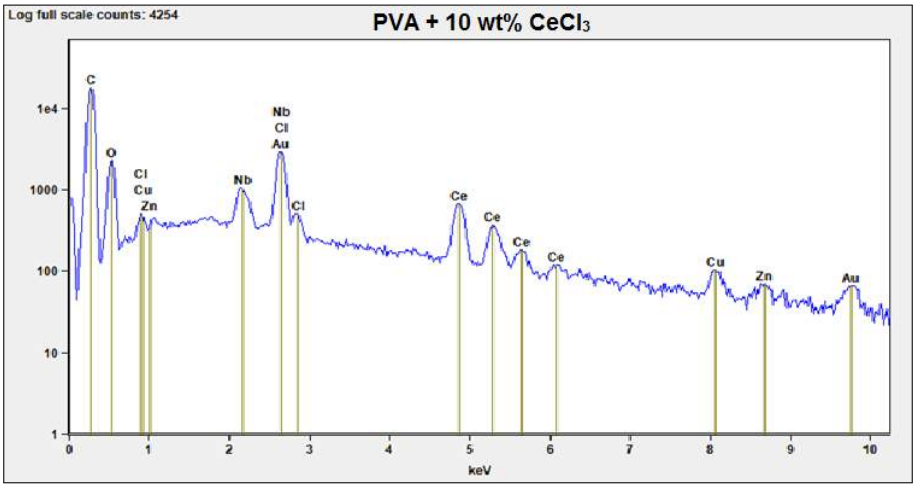

Figure C.3: *EDS spectrum of PVA fibres loaded with 10 wt% $CeCl_3$.*

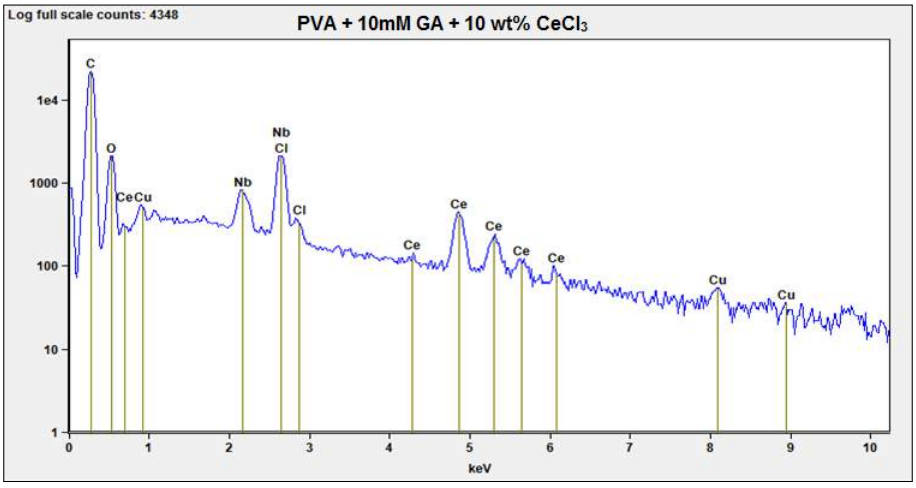

Figure C.4: *EDS spectrum of PVA fibres loaded with 10 wt% $CeCl_3$ crosslinked with 10 mM GA.*

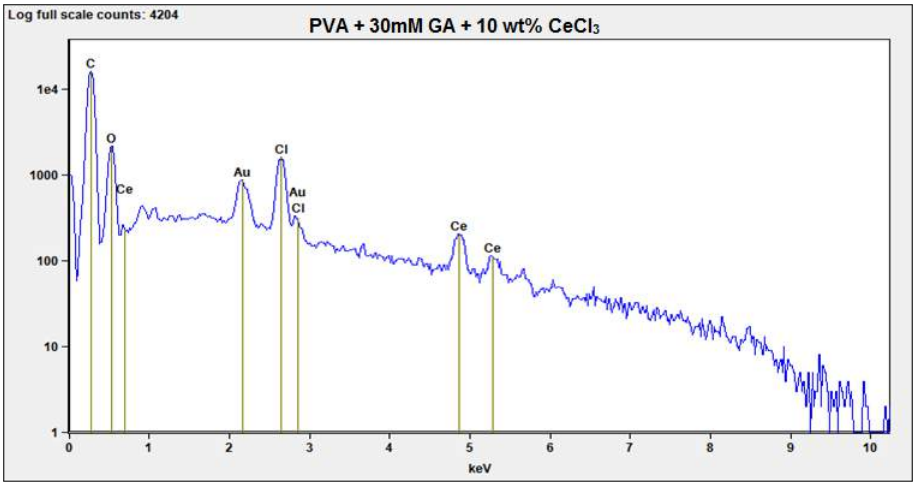

Figure C.5: *EDS spectrum of PVA fibres loaded with 10 wt% $CeCl_3$ crosslinked with 30 mM GA.*

Appendix D

Calibration UV/VIS

As mentioned in chapter 4, the absorbance, measured in absorbance units, is related to a material specific parameter, the molar absorptivity ε. This parameter depends on what you are measuring in which solvent. The value can be determined by making a calibration curve.

D.1 Calibration curve of cerium

Several solutions with different concentrations ranging from 0.05 to 0.7 mM of $CeCl_3$ and $Ce(dbp)_3$ in deionised water were prepared. The calibration curves were made by analysing the absorbance at λ = 253 nm and comparing it to the result of van Soestbergen et al. [81]. The calibration for the cerium peaks can be found in figure

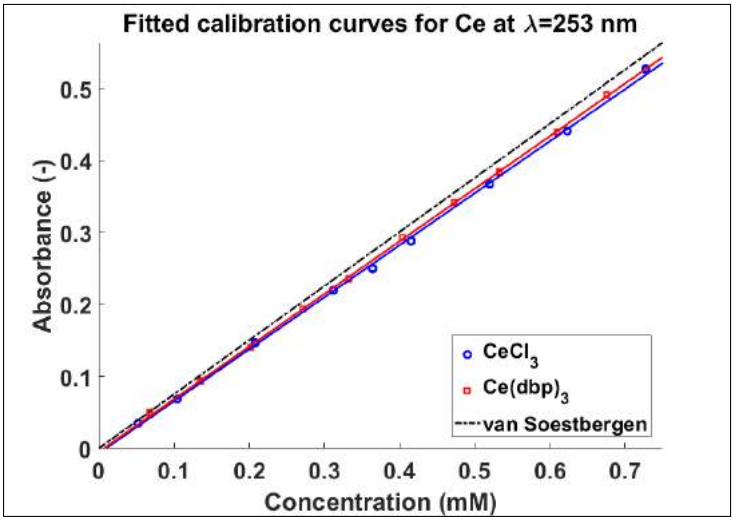

Figure D.1: *Calibration measurements of $CeCl_3$ as well as $Ce(dbp)_3$ at λ = 253 nm with fitted calibration curves, predicting a value for molar absorptivity of ϵ = 72.3 and ϵ = 73.1 m^2 mol^{-1}. The dashed line shows the predicted Beer-Lambert Law response based with of ϵ = 75.7 m^2 mol^{-1}, as measured by van Soestbergen et al. [81].*

The linear calibration relation is found to be:

$$\begin{aligned} C_{CeCl_3} &= 0.723A - 0.007 \\ C_{Ce(dbp)_3} &= 0.731A - 0.005 \end{aligned} \tag{D.1}$$

Where C_{Ce} is the concentration of cerium in solution in [mM] and A is the measured absorbance in dimensionless absorbance units. Equation D.1 allows us to follow release of cerium in solution by

following the absorbance measured at $\lambda = 253$ nm.

With equation D.1 it is also possible to determine the molar absorptivity, as we know that $l = 10 \cdot 10^{-3}$ m. Figure D.1 shows the calibration measurements and the corresponding fitted calibration curves. ϵ turns out to have a value of $\epsilon = 72.3$ m^2 mol^{-1} for $CeCl_3$ and 73.1 m^2 mol^{-1}, which is around 4% lower than the 75.7 m^2 mol^{-1} measured by van Soestbergen et al. for $Ce(dbp)_3$ [81] and the 75.2 m^2 mol^{-1} as referenced by Banks et al [119]. This difference is a little on the high side as Thomas predicts deviations between own measurements and literature values in the order of 3% [88]. The difference can be explained by several manual steps that needed to be taken in order to obtain this result and the uncertainties that this introduces, such as during weighing, dissolving and diluting the solutions. At lower concentrations the influence of small deviations can relate to relatively larger errors. It can be seen that the values for the absorptivity ϵ are directly related to the slope of the calibration curve in equations D.1.

D.2 Calibration curve of PVA

The same procedure can be used for determining a calibration peak for PVA, which absorbs light in the UV-light range as well. The selected wavelength for making a calibration curve of PVA is $\lambda = 280$ nm.

In this case the linear relationship is:

$$C_{PVA} = 0.2410A + 0.0207 \tag{D.2}$$

Figure D.2 shows the fit of the calibration measurements, following Beer-Lambert Law for $\epsilon = 24.0990$ m^2 mol^{-1}.

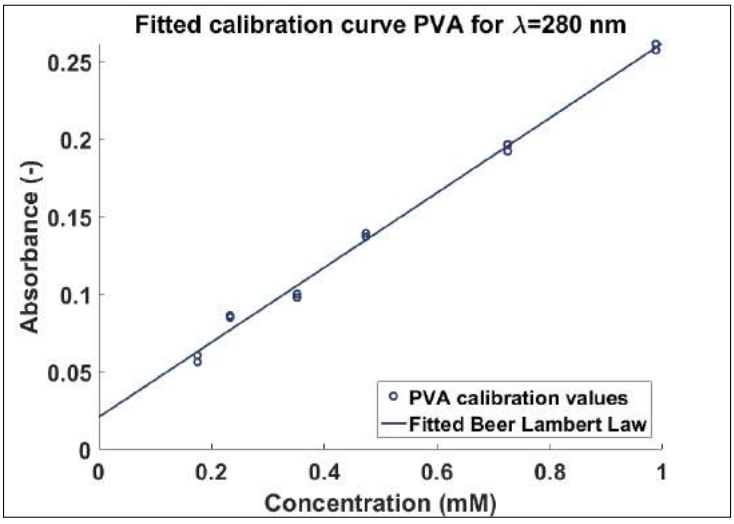

Figure D.2: *The calibration measurement points for PVA at $\lambda = 280$ nm and the fit of these points, corresponding to the Beer-Lambert Law for $\epsilon = 24.1$ m^2 mol^{-1}.*

Unfortunately Li_2CO_3 does not have a response in UV/VIS. No light is absorbed in the range of 700 - 200 nm that the machine can measure. This is probably due to the fact that lithium only has 3 electrons (2 in the inner shell, 1 in the second shell) reducing the chances that the light can excite an electron by absorbing a photon from the light with the right energy. This makes following release kinetics of lithium via UV/VIS impossible and therefore this has not been taken into account in this study. Inductively coupled plasma optical emission spectrometry (ICP-OES) could be used to detect lithium in solution [120], although this cannot be carried out in-situ.

Appendix E

Extended corrosion protection results

E.1 Passive barrier protection

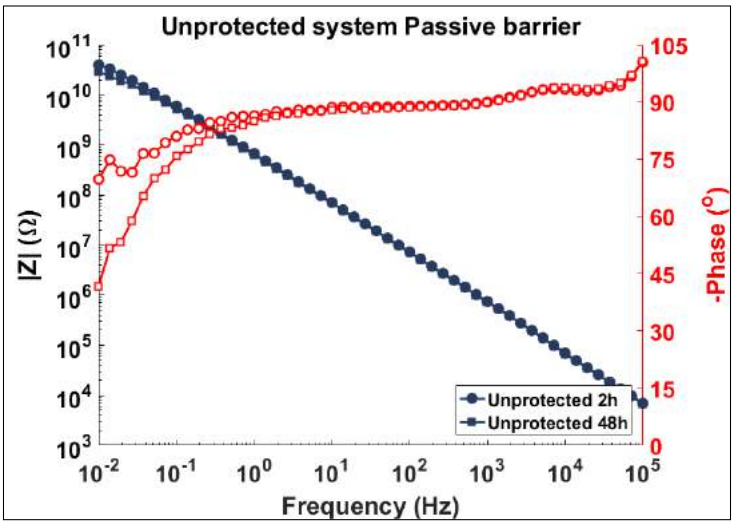

Figure E.1: *Passive barrier properties of unprotected epoxy/amine coating.*

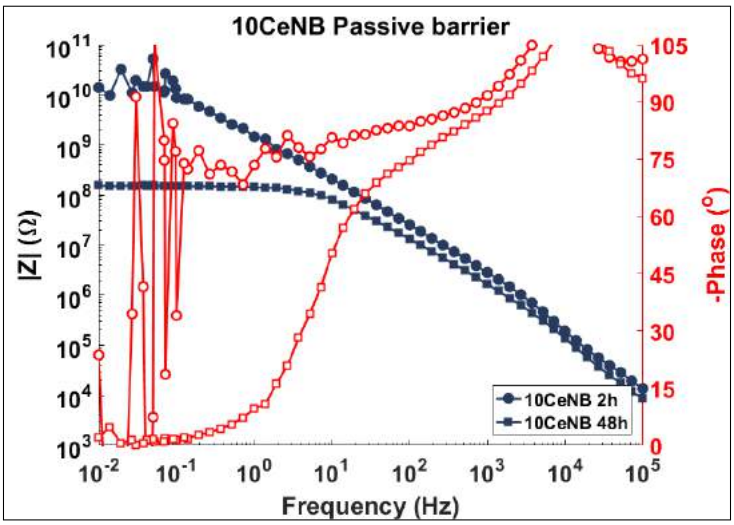

Figure E.2: *Passive barrier properties of 10CeNB coating.*

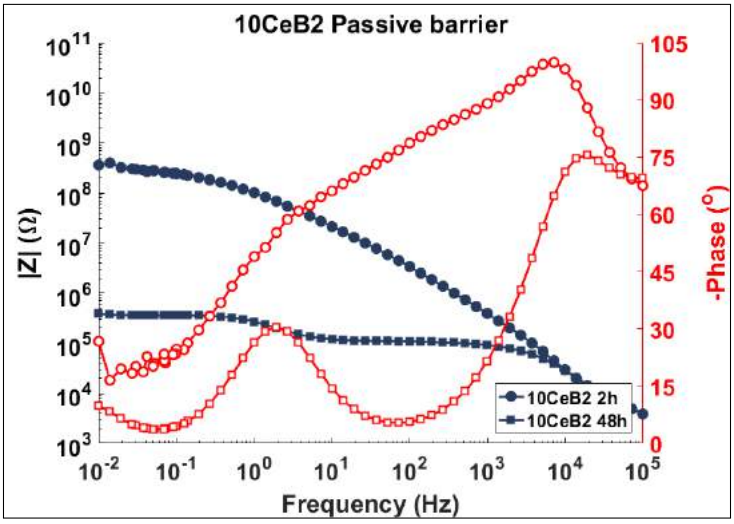

Figure E.3: *Passive barrier properties of 10CeB2 coating.*

E.2 Active corrosion protection

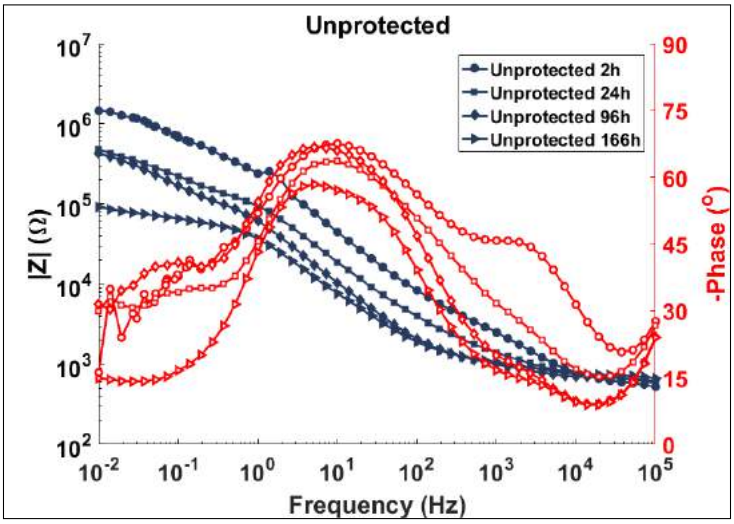

Figure E.4: *EIS data of exposed unprotected sample.*

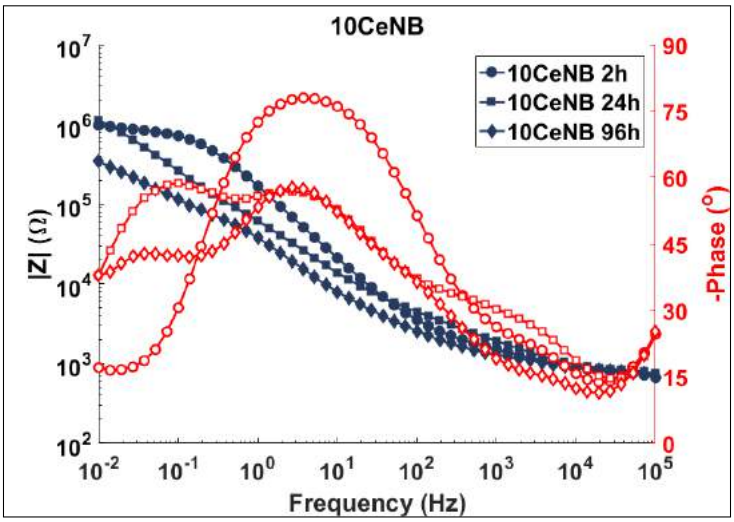

Figure E.5: *EIS data of exposed 10CeNB sample.*

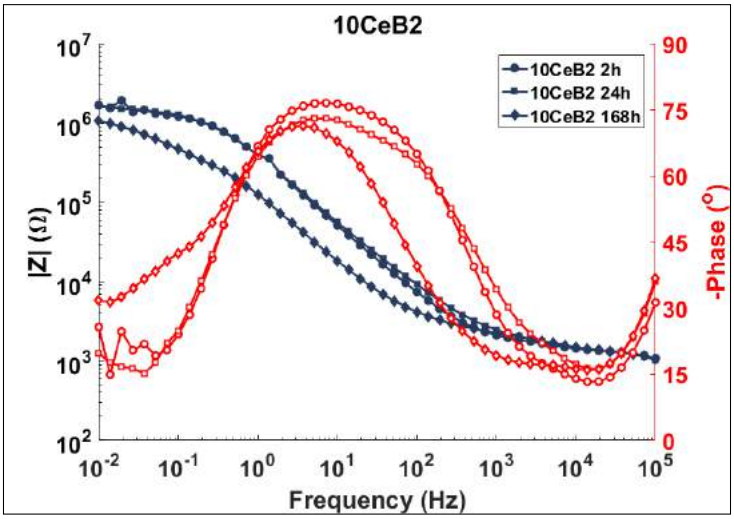

Figure E.6: *EIS data of exposed 10CeB2 sample.*

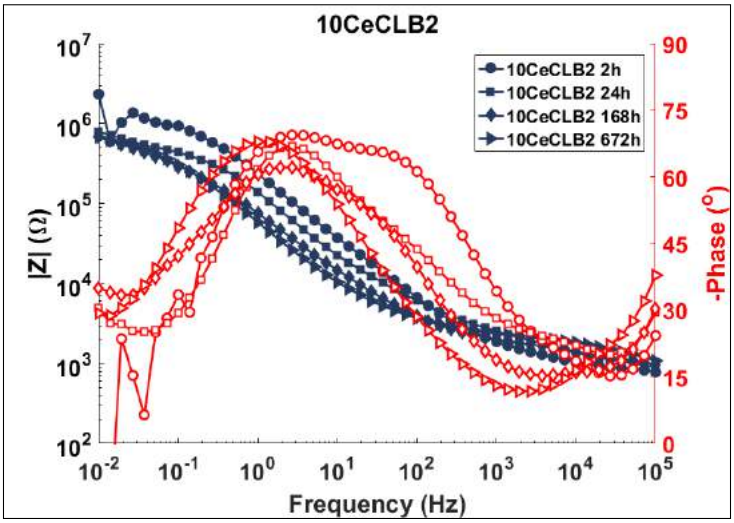

Figure E.7: *EIS data of exposed 10CeBCL2 sample.*

E.3 OCP and low frequency impedance

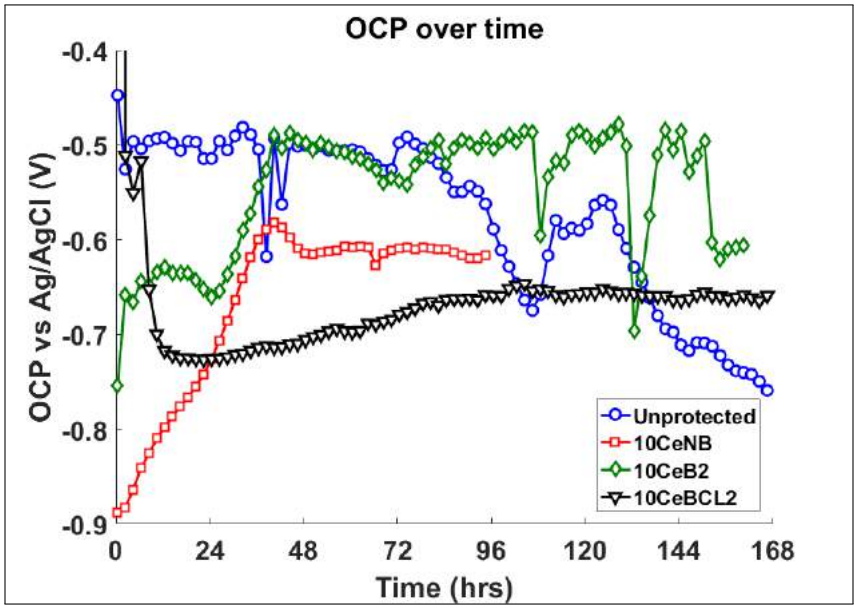

Figure E.8: *OCP over a week for several coating systems.*

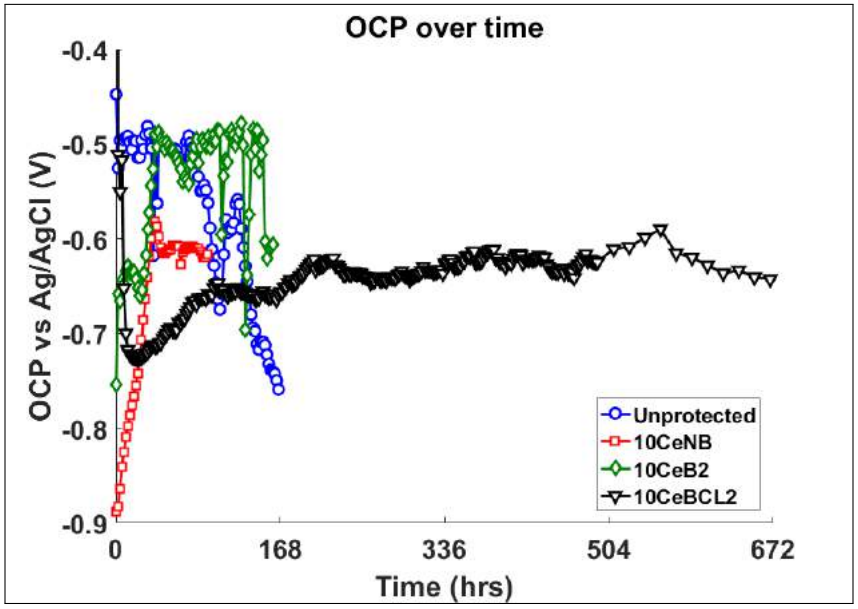

Figure E.9: *OCP over 4 weeks for several coating systems.*

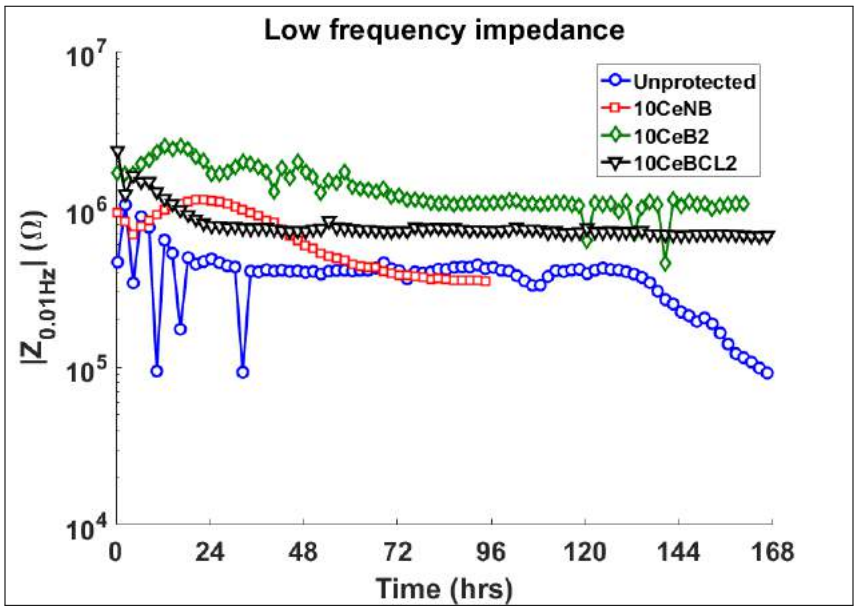

Figure E.10: *Low frequency impedance over a week for several coating systems.*

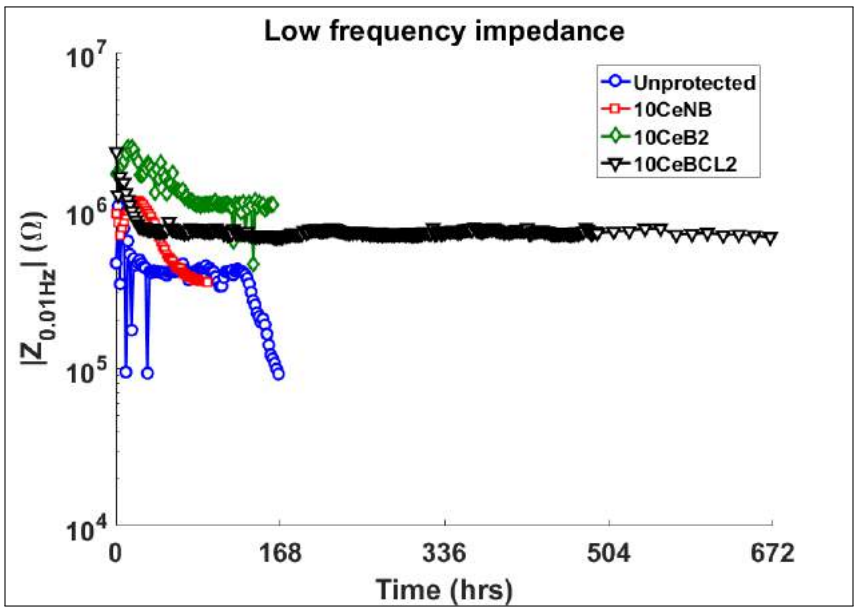

Figure E.11: *Low frequency impedance over 4 weeks for several coating systems.*

E.4 Optical corrosion results

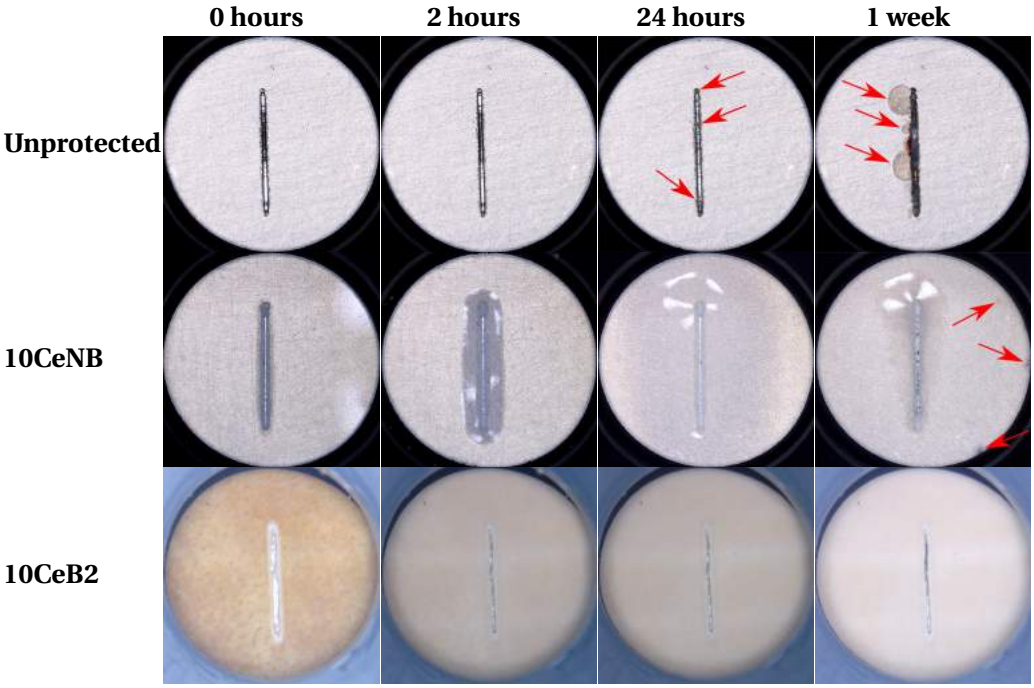

Figure E.12: *Optical results for several coating systems in corrosive environment.*

Appendix F

SEM/EDS of corroded samples

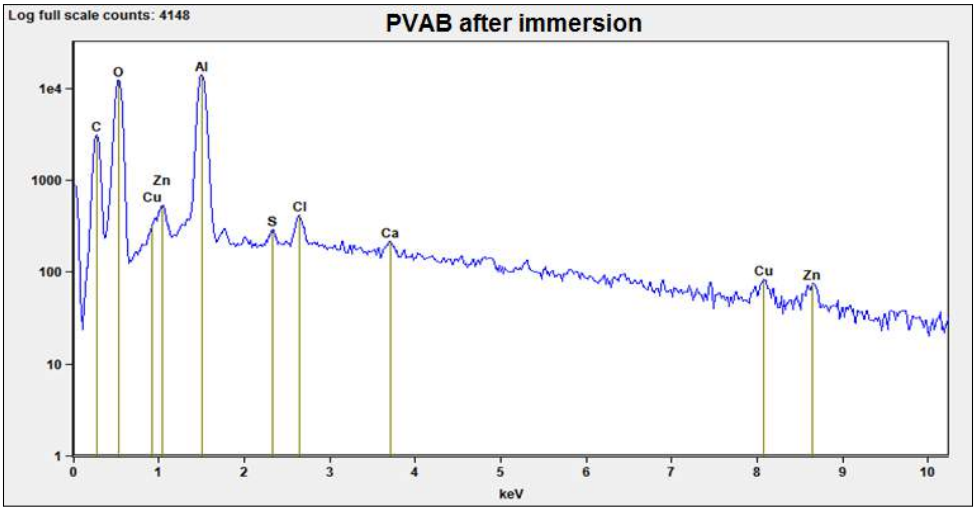

Figure F.1: *EDS spectrum of scratched PVAB sample after immersion test.*

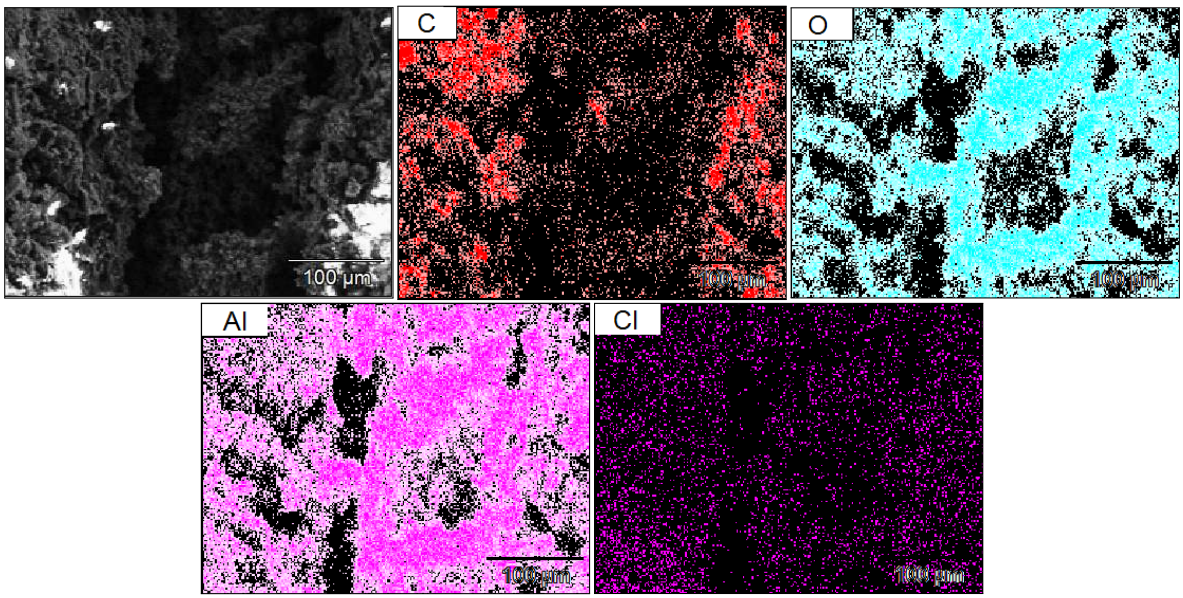

Figure F.2: *Elemental maps PVAB sample after immersion test.*

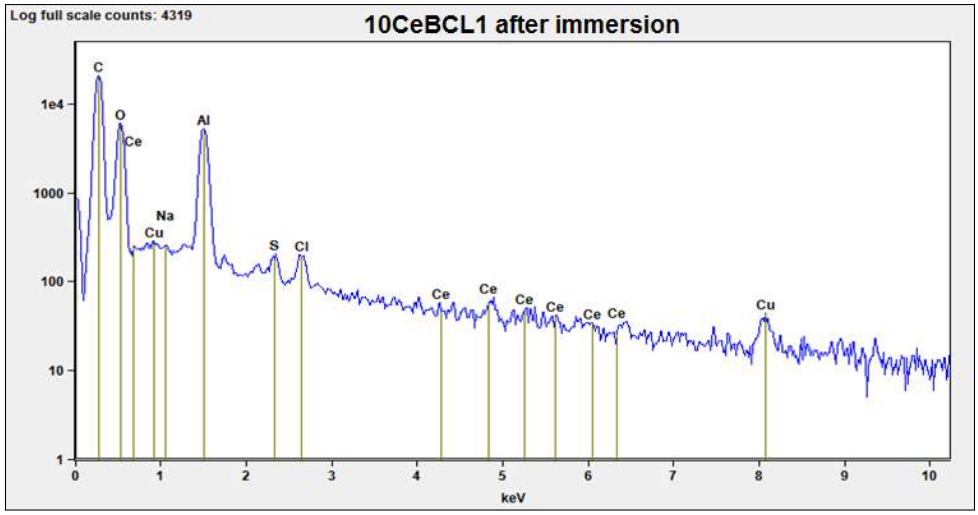

Figure F.3: *EDS spectrum of scratched 10CeBCL1 sample after immersion test.*

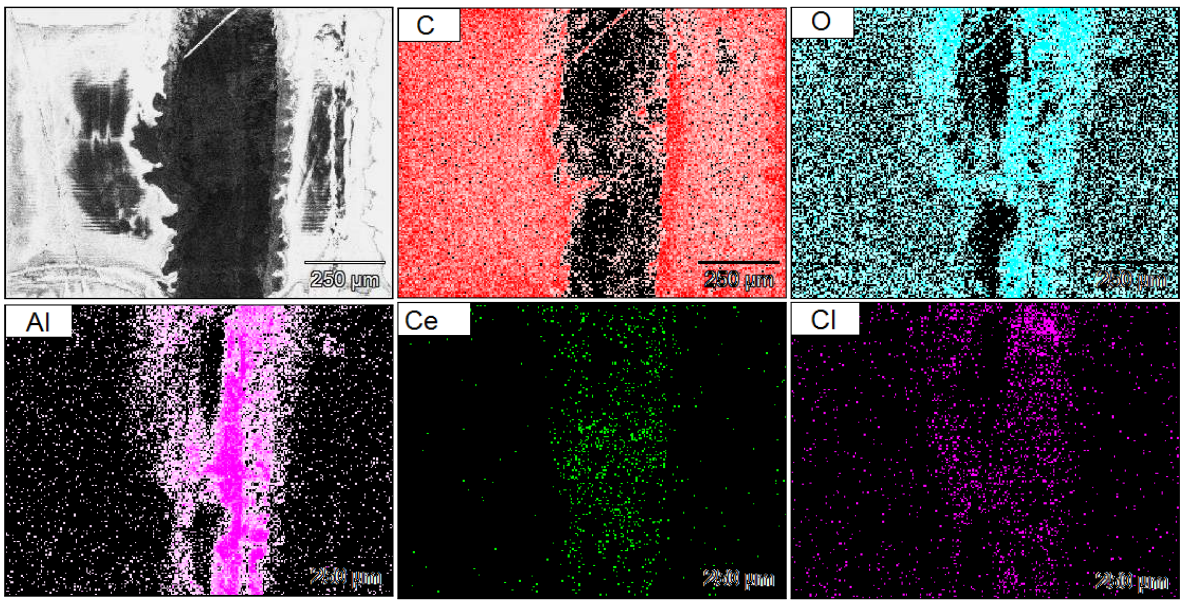

Figure F.4: *Elemental maps 10CeBCL1 sample after immersion test.*

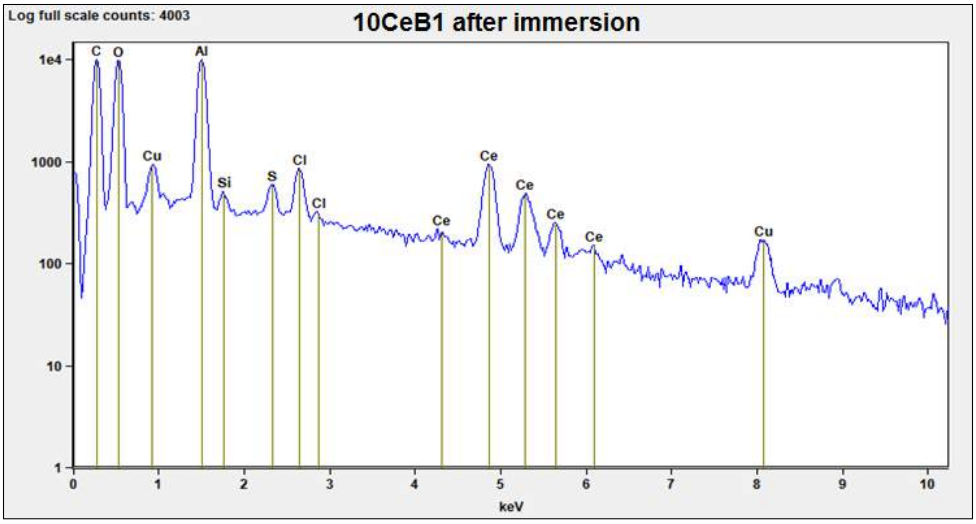

Figure F.5: *EDS spectrum of scratched 10CeB1 sample after immersion test.*

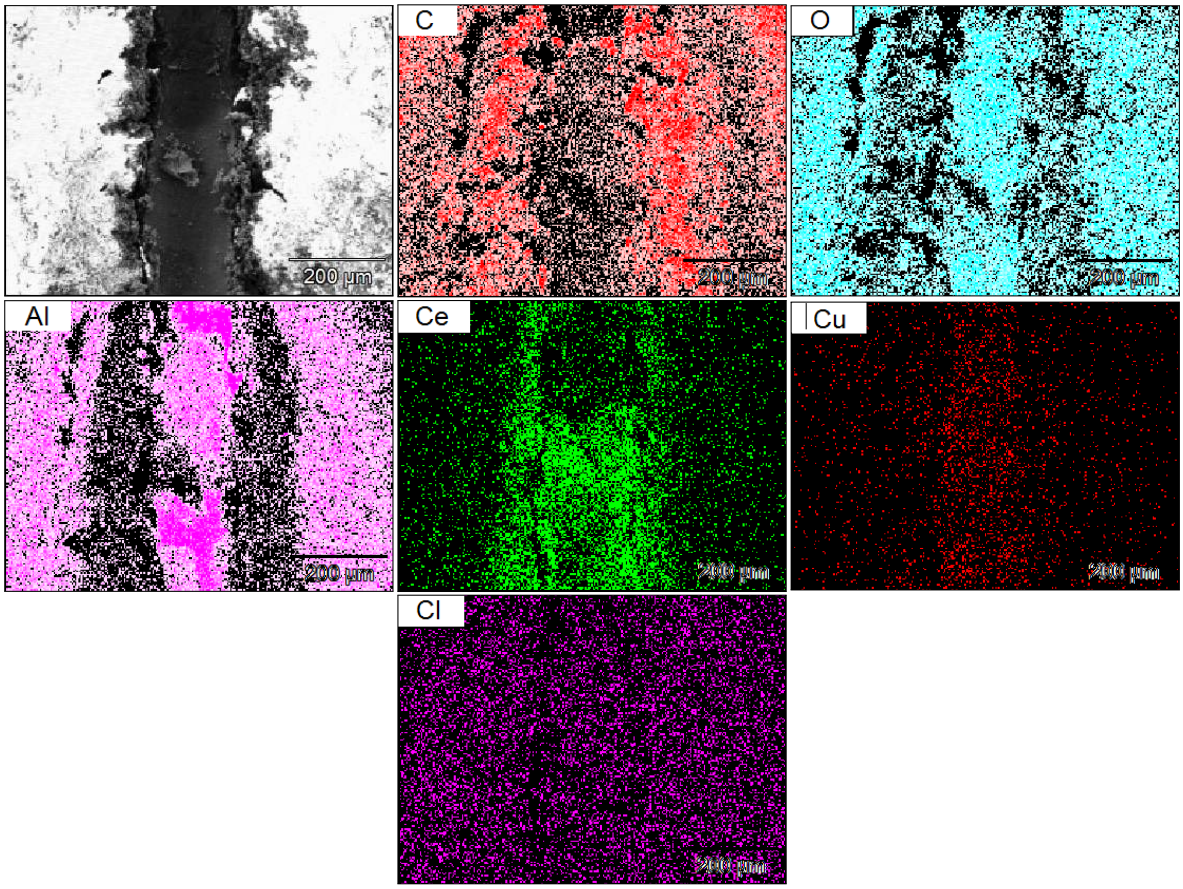

Figure F.6: *Elemental maps 10CeB1 sample after immersion test.*

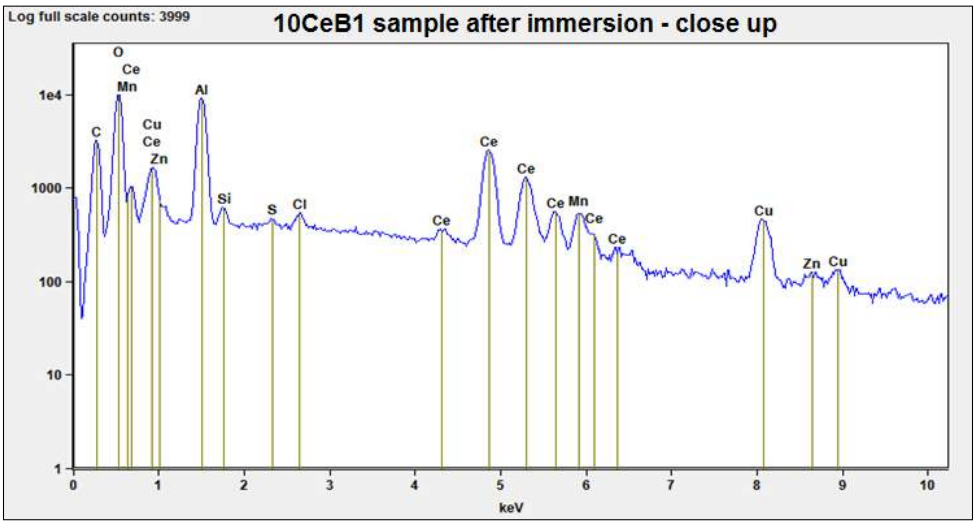

Figure F.7: *EDS spectrum of a close up of the scratched 10CeB1 sample after immersion test.*

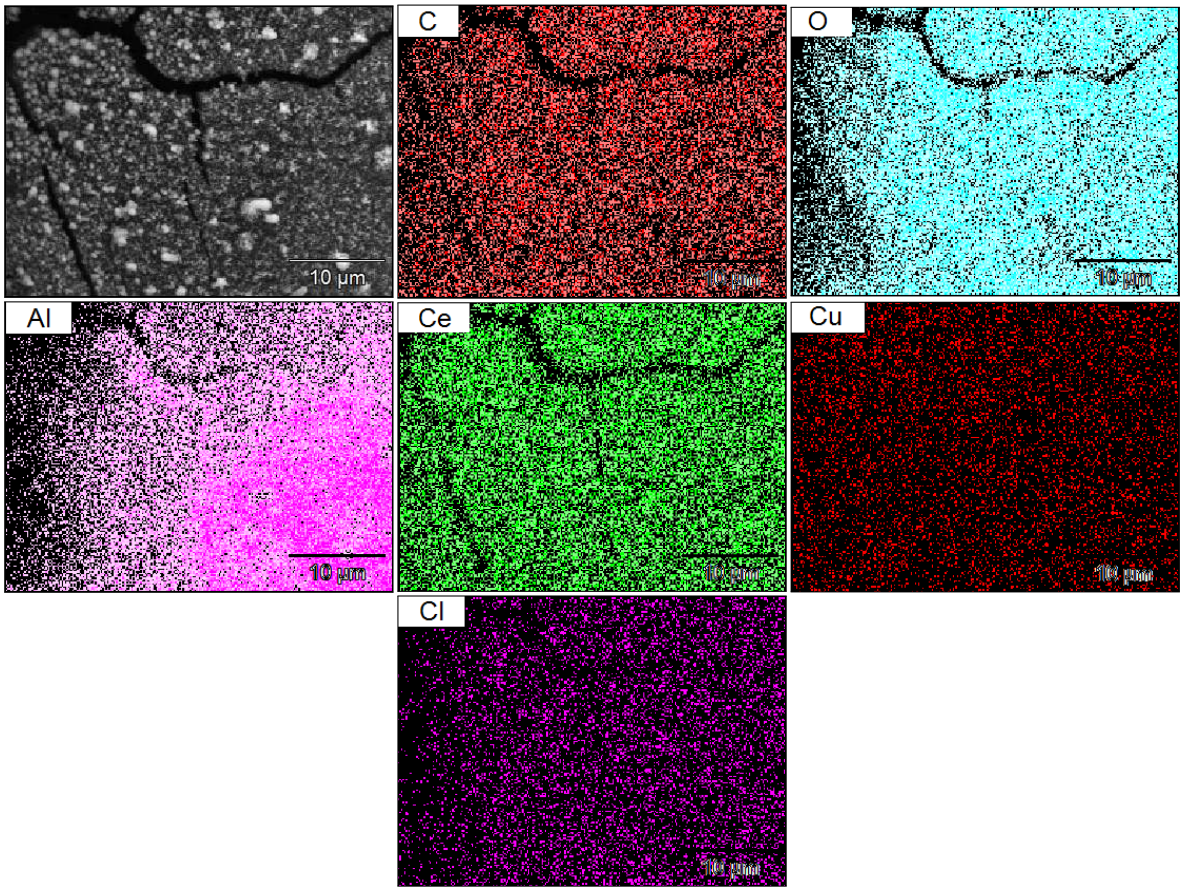

Figure F.8: *Elemental maps of a close up of the scratched 10CeB1 sample after immersion test.*

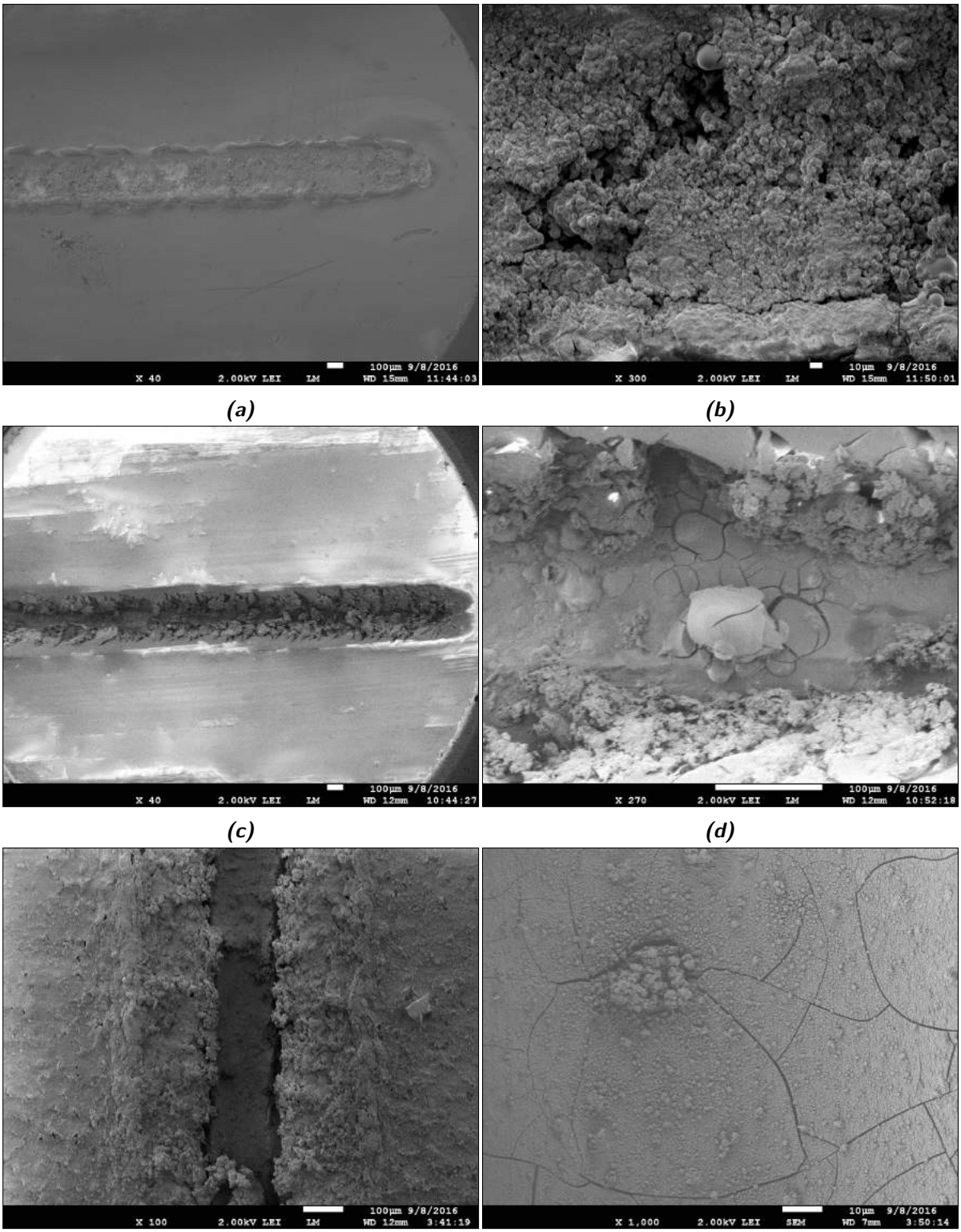

(a) ***(b)*** ***(c)*** ***(d)*** ***(e)*** ***(f)***

Figure F.9: *SEM images of scratched coatings after exposure up to 2 weeks to aqueous corrosive environment. F.9a and F.9b: Control sample without any protective system shows a scratch completely filled with aluminium corrosion products. F.9c and F.9d: 10CeNB sample with corrosion inhibitor shows a relatively clean scratch, where cracked cerium based oxide layers can be detected. F.9e and F.9f: 10CeB1 sample with corrosion inhibitor after two weeks of exposure to 0.05 M NaCl. Also this sample is relatively clean and shows cracked cerium oxide layers [16]. All cerium loaded samples showed this type of protection of the scratches.*

Bibliography

[1] H. Fong, I. Chun, and D. Reneker, "Beaded nanofibers formed during electrospinning," *Polymer*, vol. 40, no. 16, pp. 4585–4592, 1999.

[2] Z. Sun, E. Zussman, A. L. Yarin, J. H. Wendorff, and A. Greiner, "Compound core-shell polymer nanofibers by co-electrospinning," *Advanced Materials*, vol. 15, no. 22, pp. 1929–1932, 2003.

[3] G. F. Hays, "Now is the time," *World Corrosion Organization*, 2013.

[4] World Bank Databank, "Gross domestic product," *World Bank Databank*, 2013.

[5] B. N. Popov, *Corrosion Engineering*. Elsevier Science, 2015.

[6] A. Stankiewicz, I. Szczygieł, and B. Szczygieł, "Self-healing coatings in anti-corrosion applications," *Journal of Materials Science*, vol. 48, no. 23, pp. 8041–8051, 2013.

[7] J. Mardel, S. J. Garcia, P. A. Corrigan, T. Markley, A. E. Hughes, T. H. Muster, D. Lau, T. G. Harvey, A. M. Glenn, P. A. White, S. G. Hardin, C. Luo, X. Zhou, G. E. Thompson, and J. M. C. Mol, "The characterisation and performance of $Ce(dbp)_3$-inhibited epoxy coatings," *Progress in Organic Coatings*, vol. 70, pp. 91–101, 2011.

[8] S. J. Garcia, H. R. Fischer, P. A. White, J. Mardel, Y. Gonzalez-Garcia, J. M. C. Mol, and A. E. Hughes, "Self-healing anticorrosive organic coating based on an encapsulated water reactive silyl ester: Synthesis and proof of concept," *Progress in Organic Coatings*, vol. 70, pp. 142–149, 2011.

[9] M. van Soestbergen, V. Baukh, S. J. F. Erich, H. P. Huinink, and O. C. G. Adan, "Release of cerium dibutylphosphate corrosion inhibitors from highly filled epoxy coating systems," *Progress in Organic Coatings*, vol. 77, pp. 1562–1568, 2014.

[10] European Chemicals Agency, "Authorisation list." online, February 2015.

[11] M. Forsyth, M. Seter, M. Y. Tan, and B. Hinton, "Recent developments in corrosion inhibitors based on rare earth metal compounds," *Corrosion Engineering Science and Technology*, vol. 49, no. 2, pp. 130–135, 2014.

[12] M. Bethencourt, F. J. Botana, J. J. Calvino, M. Marcos, and M. A. Rodriguez-Chacon, "Lanthanide compounds as environmentally-friendly corrosion inhibitors of aluminium alloys: A review," *Corrosion Science*, vol. 40, no. 11, pp. 1803–1819, 1998.

[13] D. Ho, N. Brack, J. Scully, T. Markley, M. Forsyth, and B. Hinton, "Cerium dibutylphosphate as a corrosion inhibitor for AA2024-T3 aluminum alloys," *Journal of the Electrochemical Society*, vol. 153, no. 9, pp. B392–B401, 2006.

[14] T. Muster, D. Lau, H. Wrubel, N. Sherman, A. Hughes, T. Harvey, T. Markley, D. Alexander, P. Corrigan, and P. White, "An investigation of rare earth chloride mixtures: combinatorial optimisation for aa2024-t3 corrosion inhibition," *Surface and Interface Analysis*, vol. 42, no. 4, pp. 170–174, 2010.

[15] J. Carneiro, J. Tedim, S. C. M. Fernandes, C. S. R. Freire, A. J. D. Silvestre, A. Gandini, M. G. S. Ferreira, and M. L. Zheludkevich, "Chitosan-based self-healing protective coatings doped with cerium nitrate for corrosion protection of aluminum alloy 2024," *Progress in Organic Coatings*, vol. 75, no. 1-2, pp. 8–13, 2012.

[16] A. E. Hughes, T. A. Markley, S. J. Garcia, and J. M. C. Mol, "Comparative study of protection of AA 2024-T3 exposed to rare earth salts solutions," *Corrosion Engineering Science and Technology*, vol. 49, no. 8, pp. 674–687, 2014.

[17] I. A. Kartsonakis, E. Athanasopoulou, D. Snihirova, B. Martins, M. A. Koklioti, M. F. Montemor, G. Kordas, and C. A. Charitidis, "Multifunctional epoxy coatings combining a mixture of traps and inhibitor loaded nanocontainers for corrosion protection of AA2024-T3," *Corrosion Science*, vol. 85, pp. 147–159, 2014.

[18] S. J. Garcia, H. R. Fischer, and S. van der Zwaag, "A critical appraisal of the potential of self healing polymeric coatings," *Progress in Organic Coatings*, vol. 72, pp. 211–221, 2011.

[19] B. Aïssa, D. Therriault, E. Haddad, and W. Jamroz, "Self-healing materials systems: overview of major approaches and recent developed technologies," *Advances in Materials Science and Engineering*, vol. 2012, 2012.

[20] S. R. White, N. R. Sottos, P. H. Geubelle, J. S. Moore, M. R. Kessler, S. R. Sriram, E. N. Brown, and S. Viswanathan, "Autonomic healing of polymer composites," *Nature*, vol. 409, no. 6822, pp. 794–797, 2001.

[21] E. L. Ferrer, A. P. Rollon, H. D. Mendoza, U. Lafont, and S. J. Garcia, "Double-doped zeolites for corrosion protection of aluminium alloys," *Microporous and Mesoporous Materials*, vol. 188, pp. 8–15, 2014.

[22] E. Javierre, S. J. GarcÃŋa, J. M. C. Mol, F. J. Vermolen, C. Vuik, and S. Van Der Zwaag, "Tailoring the release of encapsulated corrosion inhibitors from damaged coatings: Controlled release kinetics by overlapping diffusion fronts," *Progress in Organic Coatings*, vol. 75, no. 1-2, pp. 20–27, 2012.

[23] T. J. Sill and H. A. von Recum, "Electrospinning: Applications in drug delivery and tissue engineering," *Biomaterials*, vol. 29, no. 13, pp. 1989–2006, 2008.

[24] S. Ramakrishna, K. Fujihara, W.-E. Teo, T.-C. Lim, and Z. Ma, "An introduction to electrospinning and nanofibers," World Scientific, 2005.

[25] A. Balogh, R. Cselkó, B. Démuth, G. Verreck, J. Mensch, G. Marosi, and Z. K. Nagy, "Alternating current electrospinning for preparation of fibrous drug delivery systems," *International Journal of Pharmaceutics*, vol. 495, no. 1, pp. 75–80, 2015.

[26] J. S. Monfared Zanjani, B. S. Okan, I. Letofsky-Papst, Y. Menceloglu, and M. Yildiz, "Repeated self-healing of nano and micro scale cracks in epoxy based composites by tri-axial electrospun fibers including different healing agents," *RSC Advances*, vol. 5, no. 89, pp. 73133–73145, 2015.

[27] P. K. Baumgarten, "Electrostatic spinning of acrylic microfibers," *Journal of colloid and interface science*, vol. 36, no. 1, pp. 71–79, 1971.

[28] C.-L. Zhang and S.-H. Yu, "Nanoparticles meet electrospinning: recent advances and future prospects," *Chemical Society Reviews*, vol. 43, pp. 4423–4448, 2014.

[29] A. L. Yarin, "Coaxial electrospinning and emulsion electrospinning of core-shell fibers," *Polymers for Advanced Technologies*, vol. 22, pp. 310–317, 2011.

[30] T. Amna, M. S. Hassan, F. A. Sheikh, H. K. Lee, K. S. Seo, D. Yoon, and I. H. Hwang, "Zinc oxide-doped poly(urethane) spider web nanofibrous scaffold via one-step electrospinning: A novel matrix for tissue engineering," *Applied Microbiology and Biotechnology*, vol. 97, pp. 1725–1734, 2013.

[31] S. K. Park, L. E. Aguilar, D. K. Kim, K. M. Lee, C. H. Park, and C. S. Kim, "Development of polyurethane/non-woven fabric composite as a protective device for filtering ultrafine particles in air and absorption of CO_2," *Digest Journal of Nanomaterials and Biostructures*, vol. 9, no. 4, pp. 1547–1553, 2014.

[32] J. Kucinska-Lipka, I. Gubanska, H. Janik, and M. Sienkiewicz, "Fabrication of polyurethane and polyurethane based composite fibres by the electrospinning technique for soft tissue engineering of cardiovascular system," *Materials Science & Engineering C-Materials for Biological Applications*, vol. 46, pp. 166–176, 2015.

[33] Y. E. Miao, G. N. Zhu, H. Hou, Y. Y. Xia, and T. Liu, "Electrospun polyimide nanofiber-based nonwoven separators for lithium-ion batteries," *Journal of Power Sources*, vol. 226, pp. 82–86, 2013.

[34] J. Shayapat, O. H. Chung, and J. S. Park, "Electrospun polyimide-composite separator for lithium-ion batteries," *Electrochimica Acta*, vol. 170, pp. 110–121, 2015.

[35] Shilpa, B. M. Basavaraja, S. B. Majumder, and A. Sharma, "Electrospun hollow glassy carbon-reduced graphene oxide nanofibers with encapsulated ZnO nanoparticles: A free standing anode for Li-ion batteries," *Journal of Materials Chemistry A*, vol. 3, no. 10, pp. 5344–5351, 2015.

[36] T. Matsuda, M. Ihara, H. Inoguchi, I. K. Kwon, K. Takamizawa, and S. Kidoaki, "Mechano-active scaffold design of small-diameter artificial graft made of electrospun segmented polyurethane fabrics," *Journal of Biomedical Materials Research - Part A*, vol. 73, pp. 125–131, 2005.

[37] J. I. Kim, H. R. Pant, H. J. Sim, K. M. Lee, and C. S. Kim, "Electrospun propolis/polyurethane composite nanofibers for biomedical applications," *Materials Science & Engineering C-Materials for Biological Applications*, vol. 44, pp. 52–57, 2014.

[38] L. M. Bellan and H. G. Craighead, "Applications of controlled electrospinning systems," *Polymers for Advanced Technologies*, vol. 22, no. 3, pp. 304–309, 2011.

[39] J. H. Park and P. V. Braun, "Coaxial electrospinning of self-healing coatings," *Advanced Materials*, vol. 22, no. 4, pp. 496–499, 2010.

[40] G. Taylor, "Disintegration of water drops in an electric field," in *Proceedings of the Royal Society of London A: Mathematical, Physical and Engineering Sciences*, vol. 280, pp. 383–397, The Royal Society, 1964.

[41] D. H. Reneker, A. L. Yarin, H. Fong, and S. Koombhongse, "Bending instability of electrically charged liquid jets of polymer solutions in electrospinning," *Journal of Applied Physics*, vol. 87, no. 9 I, pp. 4531–4547, 2000.

[42] S. L. Zhao, X. H. Wu, L. G. Wang, and Y. Huang, "Electrospinning of ethyl-cyanoethyl cellulose/tetrahydrofuran solutions," *Journal of Applied Polymer Science*, vol. 91, pp. 242–246, 2004.

[43] J. Deitzel, J. Kleinmeyer, J. Hirvonen, and N. B. Tan, "Controlled deposition of electrospun poly (ethylene oxide) fibers," *Polymer*, vol. 42, no. 19, pp. 8163–8170, 2001.

[44] X. H. Zong, K. Kim, D. F. Fang, S. F. Ran, B. S. Hsiao, and B. Chu, "Structure and process relationship of electrospun bioabsorbable nanofiber membranes," *Polymer*, vol. 43, pp. 4403–4412, 2002.

[45] S. Megelski, J. S. Stephens, D. B. Chase, and J. F. Rabolt, "Micro-and nanostructured surface morphology on electrospun polymer fibers," *Macromolecules*, vol. 35, no. 22, pp. 8456–8466, 2002.

[46] X. Yuan, Y. Zhang, C. Dong, and J. Sheng, "Morphology of ultrafine polysulfone fibers prepared by electrospinning," *Polymer International*, vol. 53, no. 11, pp. 1704–1710, 2004.

[47] J. Doshi and D. H. Reneker, "Electrospinning process and applications of electrospun fibers," *Journal of Electrostatics*, vol. 35, no. 2-3, pp. 151–160, 1995.

[48] K. H. Lee, H. Y. Kim, Y. M. La, D. R. Lee, and N. H. Sung, "Influence of a mixing solvent with tetrahydrofuran and n, n-dimethylformamide on electrospun poly(vinyl chloride) nonwoven mats," *Journal of Polymer Science Part B: Polymer Physics*, vol. 40, no. 19, pp. 2259–2268, 2002.

[49] M. G. McKee, C. L. Elkins, and T. E. Long, "Influence of self-complementary hydrogen bonding on solution rheology/electrospinning relationships," *Polymer*, vol. 45, no. 26, pp. 8705–8715, 2004.

[50] P. Supaphol, C. Mit-uppatham, and M. Nithitanakul, "Ultrafine electrospun polyamide-6 fibers: Effects of solvent system and emitting electrode polarity on morphology and average fiber diameter," *Macromolecular Materials and Engineering*, vol. 290, no. 9, pp. 933–942, 2005.

[51] J. M. Deitzel, J. Kleinmeyer, D. Harris, and N. C. B. Tan, "The effect of processing variables on the morphology of electrospun nanofibers and textiles," *Polymer*, vol. 42, pp. 261–272, 2001.

[52] J. S. Choi, S. W. Lee, L. Jeong, S.-H. Bae, B. C. Min, J. H. Youk, and W. H. Park, "Effect of organosoluble salts on the nanofibrous structure of electrospun poly (3-hydroxybutyrate-co-3-hydroxyvalerate)," *International Journal of Biological Macromolecules*, vol. 34, no. 4, pp. 249–256, 2004.

[53] J. S. Lee, K. H. Choi, H. Do Ghim, S. S. Kim, D. H. Chun, H. Y. Kim, and W. S. Lyoo, "Role of molecular weight of atactic poly(vinyl alcohol) (PVA) in the structure and properties of pva nanofabric prepared by electrospinning," *Journal of Applied Polymer Science*, vol. 93, pp. 1638–1646, 2004.

[54] D. Crespy, K. Friedemann, and A.-M. Popa, "Colloid-electrospinning: fabrication of multicompartment nanofibers by the electrospinning of organic or/and inorganic dispersions and emulsions," *Macromolecular Rapid Communications*, vol. 33, pp. 1978–1995, 2012.

[55] Y. Jin, D. Yang, D. Kang, and X. Xiang, "Fabrication of necklace-like structures via electrospinning," *Langmuir*, vol. 26, no. 2, pp. 1186–1190, 2010.

[56] A. B. Radwan, A. M. A. Mohamed, A. M. Abdullah, and M. A. Al-Maadeed, "Superhydrophobic and corrosion behavior of electrospun PVDF-ZnO coating," in *ECS Transactions*, vol. 64, pp. 57–67, 2015.

[57] X. Xu, L. Yang, X. Xu, X. Wang, X. Chen, Q. Liang, J. Zeng, and X. Jing, "Ultrafine medicated fibers electrospun from w/o emulsions," *Journal of Controlled Release*, vol. 108, no. 1, pp. 33–42, 2005.

[58] A. V. Bazilevsky, A. L. Yarin, and C. M. Megaridis, "Co-electrospinning of core-shell fibers using a single-nozzle technique," *Langmuir*, vol. 23, no. 5, pp. 2311–2314, 2007.

[59] A. L. Yarin, E. Zussman, J. H. Wendorff, and A. Greiner, "Material encapsulation and transport in core-shell micro/nanofibers, polymer and carbon nanotubes and micro/nanochannels," *Journal of Materials Chemistry*, vol. 17, no. 25, pp. 2585–2599, 2007.

[60] J. S. Monfared Zanjani, B. Saner Okan, I. Letofsky-Papst, M. Yildiz, and Y. Z. Menceloglu, "Rational design and direct fabrication of multi-walled hollow electrospun fibers with controllable structure and surface properties," *European Polymer Journal*, vol. 62, pp. 66–76, 2015.

[61] V. Kalra, J. H. Lee, J. H. Park, M. Marquez, and Y. L. Joo, "Confined assembly of asymmetric block-copolymer nanofibers via multiaxial jet electrospinning," *Small*, vol. 5, no. 20, pp. 2323–2332, 2009.

[62] D. Han and A. J. Steckl, "Triaxial electrospun nanofiber membranes for controlled dual release of functional molecules," *ACS Applied Materials and Interfaces*, vol. 5, no. 16, pp. 8241–8245, 2013.

[63] M. Angeles, H. L. Cheng, and S. S. Velankar, "Emulsion electrospinning: Composite fibers from drop breakup during electrospinning," *Polymers for Advanced Technologies*, vol. 19, no. 7, pp. 728–733, 2008.

[64] A. Arecchi, S. Mannino, and J. Weiss, "Electrospinning of poly(vinyl alcohol) nanofibers loaded with hexadecane nanodroplets," *Journal of Food Science*, vol. 75, no. 6, pp. N80–N88, 2010.

[65] A. Firouzi, A. Impagnatiello, C. Del Gaudio, F. R. Lamastra, A. Bianco, and G. Montesperelli, "Electrospun protective self-healing coatings for light alloys: A better understanding of the intrinsic potential of the technology," *Journal of Applied Polymer Science*, vol. 132, 2015.

[66] A. Covelo, J. Genescá, A. Barba, C. Menchaca, J. Uruchurtu, and M. Hernández, "Corrosion behavior of hybrid sol-gel films reinforced with electrospun nanofibers," in *Solid State Phenomena*, vol. 227, pp. 119–122, 2015.

[67] B. Grignard, A. Vaillant, J. De Coninck, M. Piens, A. M. Jonas, C. Detrembleur, and C. Jerome, "Electrospinning of a functional perfluorinated block copolymer as a powerful route for imparting superhydrophobicity and corrosion resistance to aluminum substrates," *Langmuir*, vol. 27, no. 1, pp. 335–342, 2011.

[68] G. Gong, J. Wu, J. Liu, N. Sun, Y. Zhao, and L. Jiang, "Bio-inspired adhesive superhydrophobic polyimide mat with high thermal stability," *Journal of Materials Chemistry*, vol. 22, no. 17, pp. 8257–8262, 2012.

[69] T. J. Mitchell and M. W. Keller, "Coaxial electrospun encapsulation of epoxy for use in self-healing materials," *Polymer International*, vol. 62, no. 6, pp. 860–866, 2013.

[70] M. W. Lee, S. An, C. Lee, M. Liou, A. L. Yarin, and S. S. Yoon, "Self-healing transparent core-shell nanofiber coatings for anti-corrosive protection," *Journal of Materials Chemistry A*, vol. 2, no. 19, pp. 7045–7053, 2014.

[71] S. An, M. Liou, K. Y. Song, H. S. Jo, M. W. Lee, S. S. Al-Deyab, A. L. Yarin, and S. S. Yoon, "Highly flexible transparent self-healing composite based on electrospun core-shell nanofibers produced by coaxial electrospinning for anti-corrosion and electrical insulation," *Nanoscale*, vol. 7, no. 42, pp. 17778–17785, 2015.

[72] L. Li and Y.-L. Hsieh, "Chitosan bicomponent nanofibers and nanoporous fibers," *Carbohydrate Research*, vol. 341, no. 3, pp. 374–381, 2006.

[73] W. J. Liu, H. F. Zhang, D. W. Li, C. Huang, and X. Y. Jin, "Study on needle and needleless electrospinning for nanofibers," in *Advanced Materials Research*, vol. 750-752, pp. 276–279, 2013.

[74] H. Y. Liu and J. H. He, "Frontiers of nanofiber fabrication: From electrospinning, vibration electrospinning to bubble electrospinning," in *Advanced Materials Research*, vol. 843, 2014.

[75] C. D. Dieleman, "Incorporation of organic/inorganic corro- sion inhibitors in electrospun polyurethane fibres - internship report," tech. rep., Delft University of Technology, 2015.

[76] T. Muster, H. Sullivan, D. Lau, D. Alexander, N. Sherman, S. Garcia, T. Harvey, T. Markley, A. Hughes, P. Corrigan, *et al.*, "A combinatorial matrix of rare earth chloride mixtures as corrosion inhibitors of aa2024-t3: optimisation using potentiodynamic polarisation and eis," *Electrochimica Acta*, vol. 67, pp. 95–103, 2012.

[77] S. J. Garcia, T. A. Markley, J. M. C. Mol, and A. E. Hughes, "Unravelling the corrosion inhibition mechanisms of bi-functional inhibitors by EIS and SEM-EDS," *Corrosion Science*, vol. 69, pp. 346–358, 2013.

[78] R. G. Buchheit, M. Bode, and G. Stoner, "Corrosion-resistant, chromate-free talc coatings for aluminum," *Corrosion*, vol. 50, no. 3, pp. 205–214, 1994.

[79] P. Visser, Y. Liu, X. Zhou, T. Hashimoto, G. E. Thompson, S. B. Lyon, L. G. van der Ven, A. J. Mol, and H. A. Terryn, "The corrosion protection of aa2024-t3 aluminium alloy by leaching of lithium-containing salts from organic coatings," *Faraday discussions*, vol. 180, pp. 511–526, 2015.

[80] C. Zhang, X. Yuan, L. Wu, Y. Han, and J. Sheng, "Study on morphology of electrospun poly(vinyl alcohol) mats," *European Polymer Journal*, vol. 41, no. 3, pp. 423 – 432, 2005.

[81] M. van Soestbergen, S. J. F. Erich, H. P. Huinink, and O. C. G. Adan, "Dissolution properties of cerium dibutylphosphate corrosion inhibitors," *Corrosion Engineering Science and Technology*, vol. 48, no. 3, pp. 234–240, 2013.

[82] A. Seidell, *Solubilities of inorganic and organic compounds c. 2*. D. Van Nostrand Company, 1919.

[83] K. Arndt, A. Richter, S. Ludwig, J. Zimmermann, J. Kressler, D. Kuckling, and H. Adler, "Poly (vinyl alcohol)/poly (acrylic acid) hydrogels: Ft-ir spectroscopic characterization of crosslinking reaction and work at transition point," *Acta Polymerica*, vol. 50, no. 11-12, pp. 383–390, 1999.

[84] X. Jin and Y.-L. Hsieh, "ph-responsive swelling behavior of poly (vinyl alcohol)/poly (acrylic acid) bi-component fibrous hydrogel membranes," *Polymer*, vol. 46, no. 14, pp. 5149–5160, 2005.

[85] J.-C. Park, T. Ito, K.-O. Kim, K.-W. Kim, B.-S. Kim, M.-S. Khil, H.-Y. Kim, I.-S. Kim, *et al.*, "Electrospun poly (vinyl alcohol) nanofibers: effects of degree of hydrolysis and enhanced water stability," *Polymer journal*, vol. 42, no. 3, pp. 273–276, 2010.

[86] C. Tang, C. D. Saquing, J. R. Harding, and S. A. Khan, "In situ cross-linking of electrospun poly (vinyl alcohol) nanofibers," *Macromolecules*, vol. 43, no. 2, pp. 630–637, 2009.

[87] X. Wang, X. Chen, K. Yoon, D. Fang, B. S. Hsiao, and B. Chu, "High flux filtration medium based on nanofibrous substrate with hydrophilic nanocomposite coating," *Environmental science & technology*, vol. 39, no. 19, pp. 7684–7691, 2005.

[88] M. J. Thomas and D. J. Ando, *Ultraviolet and visible spectroscopy*. Published on behalf of ACOL (University of Greenwich) by J. Wiley, 1996.

[89] P. Denissen, "Development and testing of nano-porous micro-carriers for corrosion inhibitor release from protective organic coatings," Master's thesis, Delft University of Technology, 2015.

[90] R. W. Korsmeyer and N. A. Peppas, "Effect of the morphology of hydrophilic polymeric matrices on the diffusion and release of water soluble drugs," *Journal of membrane Science*, vol. 9, no. 3, pp. 211–227, 1981.

[91] H. S. Mansur, C. M. Sadahira, A. N. Souza, and A. A. Mansur, "Ftir spectroscopy characterization of poly (vinyl alcohol) hydrogel with different hydrolysis degree and chemically crosslinked with glutaraldehyde," *Materials Science and Engineering: C*, vol. 28, no. 4, pp. 539–548, 2008.

[92] C.-K. Yeom and K.-H. Lee, "Pervaporation separation of water-acetic acid mixtures through poly (vinyl alcohol) membranes crosslinked with glutaraldehyde," *Journal of Membrane Science*, vol. 109, no. 2, pp. 257–265, 1996.

[93] J. L. Taylor, C. Lynch, and J. F. Dlugos, "Particle characterization of uv blocking sunscreens and cosmetics using uv/visible spectroscopy," tech. rep., Perkin-Elmer, 2013.

[94] X. Hou, R. S. Amais, B. T. Jones, and G. L. Donati, "Inductively coupled plasma optical emission spectrometry," *Encyclopedia of analytical chemistry*, 2000.

[95] G. Singhvi and M. Singh, "Review: in-vitro drug release characterization models," *Int J Pharm Stud Res*, vol. 2, no. 1, pp. 77–84, 2011.

[96] R. W. Korsmeyer, R. Gurny, E. Doelker, P. Buri, and N. A. Peppas, "Mechanisms of solute release from porous hydrophilic polymers," *International journal of pharmaceutics*, vol. 15, no. 1, pp. 25–35, 1983.

[97] P. L. Ritger and N. A. Peppas, "A simple equation for description of solute release i. fickian and non-fickian release from non-swellable devices in the form of slabs, spheres, cylinders or discs," *Journal of Controlled Release*, vol. 5, no. 1, pp. 23 – 36, 1987.

[98] F. Maia, K. A. Yasakau, J. Carneiro, S. Kallip, J. Tedim, T. Henriques, A. Cabral, J. Venâncio, M. L. Zheludkevich, and M. G. S. Ferreira, "Corrosion protection of AA2024 by sol-gel coatings modified with MBT-loaded polyurea microcapsules," *Chemical Engineering Journal*, vol. 283, pp. 1108–1117, 2016.

[99] P. L. Ritger and N. A. Peppas, "A simple equation for description of solute release ii. fickian and anomalous release from swellable devices," *Journal of controlled release*, vol. 5, no. 1, pp. 37–42, 1987.

[100] F. M. De Wit, *Polymer bonding and adhesion on aluminium and magnesium alloys*. TU Delft, Delft University of Technology, 2012.

[101] C. Mathis, "Development of an optical-electrochemical technique for in-situ evaluation of silane based healing agents," Master's thesis, Delft University of Technology, 2013.

[102] M. Fabián, B. Antić, V. Girman, M. Vučinić-Vasić, A. Kremenović, S. Suzuki, H. Hahn, and V. Šepelák, "Mechanosynthesis and structural characterization of nanocrystalline ce 1–x yxo 2–δ (x= 0.1–0.35) solid solutions," *Journal of Solid State Chemistry*, vol. 230, pp. 42–48, 2015.

[103] B. L. Hurley, S. Qiu, and R. Buchheit, "Raman spectroscopy characterization of aqueous vanadate species interaction with aluminum alloy 2024-t3 surfaces," *Journal of The Electrochemical Society*, vol. 158, no. 5, pp. C125–C131, 2011.

[104] C. Brinker, A. Hurd, P. Schunk, G. Frye, and C. Ashley, "Review of sol-gel thin film formation," *Journal of Non-Crystalline Solids*, vol. 147-148, no. C, pp. 424–436, 1992.

[105] L. Kasten, J. Grant, N. Grebasch, N. Voevodin, F. Arnold, and M. Donley, "An xps study of cerium dopants in sol–gel coatings for aluminum 2024-t3," *Surface and Coatings Technology*, vol. 140, no. 1, pp. 11–15, 2001.

[106] T. A. Markley, *Corrosion mitigation of aerospace alloys using rare earth diphenyl phosphates*. PhD thesis, Monash University. Faculty of Engineering. Department of Materials Engineering, 2008.

[107] D. Snihirova, S. V. Lamaka, and M. Montemor, "Smart protective ability of water based epoxy coatings loaded with $CaCO_3$ microbeads impregnated with corrosion inhibitors applied on AA2024 substrates," *Electrochimica Acta*, vol. 83, pp. 439–447, 2012.

[108] G. Sabitha, R. S. Babu, M. Rajkumar, C. S. Reddy, and J. Yadav, "Highly regioselective ring opening of epoxides and aziridines using cerium (III) chloride," *Tetrahedron letters*, vol. 42, no. 23, pp. 3955–3958, 2001.

[109] L. R. Reddy, M. A. Reddy, N. Bhanumathi, and K. R. Rao, "Cerium chloride-catalysed cleavage of epoxides with aromatic amines," *Synthesis*, vol. 2001, no. 06, pp. 0831–0832, 2001.

[110] M. E. Orazem and B. Tribollet, *Electrochemical impedance spectroscopy*, vol. 48. John Wiley & Sons, 2011.

[111] E. Darmiani, I. Danaee, M. Golozar, and M. Toroghinejad, "Corrosion investigation of al–sic nano-composite fabricated by accumulative roll bonding (arb) process," *Journal of Alloys and Compounds*, vol. 552, pp. 31–39, 2013.

[112] M. Abdulstaar, M. Mhaede, L. Wagner, and M. Wollmann, "Corrosion behaviour of al 1050 severely deformed by rotary swaging," *Materials & Design*, vol. 57, pp. 325–329, 2014.

[113] P. R. Roberge, *Handbook of corrosion engineering*. McGraw-Hill,, 2000.

[114] T. A. Markley, M. Forsyth, and A. E. Hughes, "Corrosion protection of aa2024-t3 using rare earth diphenyl phosphates," *Electrochimica acta*, vol. 52, no. 12, pp. 4024–4031, 2007.

[115] P. Campestrini, E. Van Westing, H. Van Rooijen, and J. De Wit, "Relation between microstructural aspects of aa2024 and its corrosion behaviour investigated using afm scanning potential technique," *Corrosion Science*, vol. 42, no. 11, pp. 1853–1861, 2000.

[116] P. Campestrini, H. Terryn, A. Hovestad, and J. De Wit, "Formation of a cerium-based conversion coating on aa2024: relationship with the microstructure," *Surface and Coatings Technology*, vol. 176, no. 3, pp. 365–381, 2004.

[117] R. Catubig, A. Hughes, I. Cole, B. Hinton, and M. Forsyth, "The use of cerium and praseodymium mercaptoacetate as thiol-containing inhibitors for aa2024-t3," *Corrosion science*, vol. 81, pp. 45–53, 2014.

[118] X.-J. Li, C.-J. Yan, W.-J. Luo, Q. Gao, Q. Zhou, C. Liu, and S. Zhou, "Exceptional cerium (iii) adsorption performance of poly (acrylic acid) brushes-decorated attapulgite with abundant and highly accessible binding sites," *Chemical Engineering Journal*, vol. 284, pp. 333–342, 2016.

[119] C. V. Banks and D. W. Klingman, "Spectrophotometric determination of rare earth mixtures," *Analytica Chimica Acta*, vol. 15, pp. 356–363, 1956.

[120] I. Segal, E. Dorfman, O. Yoffe, I. Bezrukavnikov, and A. Agranat, "Direct ICP-OES determination of low concentrations of Cu, Fe, Li, Ti, and V in Potassium Lithium Tantalate Niobate crystals," *ATOMIC SPECTROSCOPY-NORWALK CONNECTICUT-*, vol. 21, no. 2, pp. 46–49, 2000.